

Precise Measurement of the Neutron Skin Thickness of ^{208}Pb and ^{48}Ca

A Dissertation Presented

by

Weibin Zhang

to

The Graduate School

in Partial Fulfillment of the Requirements

for the Degree of

Doctor of Philosophy

in

Physics

Stony Brook University

June 2022

Stony Brook University

The Graduate School

Weibin Zhang

We, the dissertation committee for the above candidate for the Doctor of Philosophy degree, hereby recommend acceptance of this dissertation.

Abhay Deshpande – Dissertation Advisor
Professor, Department of Physics and Astronomy

Joanna Kiryluk – Chairperson of Defense
Professor, Department of Physics and Astronomy

James M. Lattimer
Professor, Department of Physics and Astronomy

Name of Outside Member
Position
Institution

This dissertation is accepted by the Graduate School.

Eric Wertheimer
Dean of the Graduate School

Abstract of the Dissertation

**Precise Measurement of the Neutron Skin Thickness
of ^{208}Pb and ^{48}Ca**

by

Weibin Zhang

Doctor of Philosophy

in

Physics

Stony Brook University

2022

text of abstract

Contents

List of Figures	v
Acknowledgements	vi
1 Introduction	2
1.0.1 Neutron Radius and Neutron Skin	2
1.0.2 Theoretical Models	6
1.1 Symmetry Energy	9
1.2 Physics Beyond the Standard Model (SM)	13
1.3 Asymmetry	13
1.4 Dynamics	20
1.5 Why Pb and Ca	21
2 Experimental Setup	23
2.1 Kinematics	25
2.1.1 Figure Of Merits (FOM)	26
2.2 Continuous Electron Beam Accelerator Facility (CEBAF)	29
2.3 Polarized Electron	32
2.3.1 Polarized Electron Source	32
2.3.2 Polarization Control	34
2.3.3 Polarimeters	39
2.4 Monitors	44
2.4.1 BPMs	44
2.4.2 BCMs	45
2.4.3 SAMs	47
2.4.4 Beam Modulation	47
2.5 Target	48
2.5.1 Target Cooling	50
2.5.2 Raster	50
2.5.3 Beamline Collimator and Sieve Slit Collimators	52
2.5.4 Septum	53
2.5.5 High Resolution Spectrometer (HRS)	54
2.5.6 Detector Package	54
2.5.7 Data AcQuisition (DAQ)	58

3 Data Analysis	61
3.1 Raw Data	64
3.1.1 Measured Asymmetry	64
3.1.2 Beam False Asymmetry	64
3.2 Regression	65
3.2.1 The Model	65
3.3 Beam Modulation	67
3.4 Lagragian	67
3.5 Correction	67
3.6 Result	67
4 Transverse Asymmetry	68
4.1 Motivation for Transverse Asymmetry	68
4.2 How to Measure the Transverse Asymmetry: the Method	68
4.3 The Result	68
5 Systematic Uncertainties	69
5.1 Q^2 and θ	69
5.2 Carbon Contamination in PREX-II	69
5.3 Acceptance Function	70
6 Results	71
6.1 Polarization	71
6.1.1 Moller	71
6.1.2 Compton	71
6.2 Final Number	71
6.3 Physical Implication	71
6.3.1 Theoretical Models	71
6.3.2 Saturation Density	72
6.4 Neutron Stars	73
Bibliography	74
A Symmetry Energy	79
A.1 Resource	79

List of Figures

1.1	Characristic of FF w.r.t. different density distribution functions	5
1.2	As we can see, the virtual photon wave absorbed by a nucleon at position \mathbf{r} will travel a further distance $\mathbf{q} \cdot \mathbf{r}$ than the one absorbed at the central point, therefore a phase difference $e^{i\mathbf{q}\mathbf{r}/\hbar}$	7
1.3	Left: Mott cross section of electron elastically scattered off a Ca48 target. Parameters: $p = E = 757.5 \text{ MeV}$. Middle: cross section of electron elastically scattered off Ca48 with the hard ball model (1.0.2). Parameters: $E = 757.5 \text{ MeV}$, $R = A^{1/3} \text{ fm}$. Right: experimental values (dots) and theoretical prediction (solid line), their calculation assumed the charge distribution as a Fermi 3-parameter function. $\rho(r) = \frac{\rho_0(1+\omega r^2/c^2)}{1+\exp((r-c)/a)}$. The ^{48}Ca (^{40}Ca) cross sections are multiplied by 10^{-1} (10) to seperate them. [1]	8
1.4	In nuclear Shell Model, it is assumed that nucleons occupy different eigenstates of the same spherically symmetric average potential. This potential, unlike that in atomic shell model, needed to be guessed. It turns out that the Saxon-Woods model is a good candidate: $V(r) = -\frac{V(0)}{1+\exp((r-c)/a)}$ (c is the half-height raidus and a represents diffuseness of the distribution). Because the potential is formed by all nucleons, so it is approximatively proportional to the nucleon density, therefore the same distribution for nucleon density.	8
1.5	PV asymmetry for ^{208}Pb and ^{48}Ca versus scattering angle at 850 MeV (Coulomb distortion correction included). The dotted curve assumes the same weak and charge distribution, while the solid curve is based on relativistic Mean Field Densities. The dashed curve in ^{208}Pb plot uses 3 parameter Fermi distribution [2]	9
1.7	Fermi's interpretation of beta decay, current $j_{n \rightarrow p}$ convert n into p and current $j_{\nu_e \rightarrow e}$ creates $(e, \bar{\nu}_e)$ pair.	14
1.8	W-boson exchange picture of β decay	16
1.9	Nuclear Landscape	21

2.1	Evolution of PVES experiments, solid lines represent the relative precision. Generation I experiments (E122 (1978) [3], MIT-12C (1989) [4] and Mainz-Be (1990) [5]) did pioneering work to pave the way for PVES. Generation II experiments (the SAMPLE collaboration [6] at the MIT-Bates accelerator, the G0 [7] and HAPPEX [8] collaboration at Jefferson Lab and the A4 collaboration [9] at the Maizer Mikrotron (MAMI) accelerator) were devoted to the exploration of strange FFs in nucleons. Generation III experiments (E158 at SLAC [10], Qweak [11] and PVDIS [12]) tested the SM at low energy and measured the neutron skin thickness of nuclei (PREX-I/II and CREX). The planned Generation IV experiments (SoLID program [13] and M OLLEr experiment [14] at JLab, P2 experiment on the future Mainz Energy-recovery Superconducting Accelerator (MESA) [15]) will continue to test the SM and explore the structure of nucleons with higher precisions. (MESA-12C is the same experiment as MESA-P2 with a different ^{12}C target)	24
2.2	Scattering rate versus beam energy and scattering angle for ^{208}Pb and ^{48}Ca , the energy and scattering angle are design values. We see that rate falls quickly along both beam energy and scattering angle for both nuclei, so one would like small beam energy and small scattering angle (equivalently small \mathbf{q}) for large scattering rate.	28
2.3	Asymmetry and sensitivity plot for ^{208}Pb , which increases along beam energy and oscillating up along scattering angle. The sensitivity plot is calculated with 1% change in neutron radius and it shows the absolute value. So in small scattering angle region, there is a local maximum around 6°	29
2.4	Asymmetry and sensitivity plot for ^{48}Ca , the asymmetry maximize around 2500 MeV and there is a local maximum about 4.5° . As for sensitivity, there is regional maximum around 5°	29
2.5	For both nuclei, FOM supports a small scattering angle. As for beam energy, FOM maximize around 950 (2200) GeV for ^{208}Pb (^{48}Ca).	29
2.6	Aerial view of JLab accelerator site, yellow line tells the position of the CEBAF accelerator and the 3 experimental halls are marked out as A/B/C (Hall D locates on the top left corner, after the exit of north LINAC). The accelerator tunnel is 30 feet ($\sim 9\text{ m}$) underground and 10 feet ($\sim 3\text{ m}$) high, with a circumference of about 7/8 miles (1.4 km). There are 2 superconducting LINAC (red lines), each of 1/4 miles (400 m). The pink part on the mid left is the location of injector. The right 2 plots show the tunnel and experimental halls under construction.	30
2.7	Schematic plot of CEBAF. Low energy beams will be kicked into higher arc, and high energy beams will go through lower arc. The magnetic field increases from higher arc to lower arc to keep electron trajectory have the same radius.	31

2.8	3D and bird view of Hall A [?]. Originally, they were called High Resolution Hadron Spectrometer (HRHS) and High Resolution Electron Spectrometer (HRES), but they are essentially identical to each other and can be used interchangeably. so now they are called left arm (HRS-L) and right arm HRS (HRS-R)	32
2.9	Excitation of polarized electrons	33
2.10	The energy band diagram of GaAs near its surfacer. Left: bare p-type GaAs, the large positive electron affinity (PEA) prevents electrons from escaping the surface; Middle: p-type GaAs with a cesiated surface, the electron affinity (EA) is 0, but electrons still can't escape the surface easily; Right: GaAs with layer of cesium oxide; the electron vaccum energy E_∞ is lowered to make a negative EA so that electrons can break free the surface easily. [16]	33
2.11	Strained GaAs	34
2.12	The laser system at the CEBAF injector	35
2.13	How the laser table actually looks like	36
2.14	Phase shift by going through the PC	36
2.15	Schematic plot of double wien filter, electron beam travels from left to right. [17]	38
2.16	Schematic plot of the Mott polarimeter, it has 4 symmetric detector ports (up and down, left and right – which is not shown in the plot). The back scattering angle is 172.6° , where we have the highest analyzing power from theoretical calculation of the Sherman function. [33]	39
2.17	The Sherman Function for different high-Z targets at 5 MeV, dots represent experimental measurement.	40
2.18	Left: Compton Chicane [?]; Right: Schematic plot of electron/photon scattering	41
2.19	The Compton analyzing power increases with electron energy. Note that the analyzing power will change sign at $\rho \sim 0.5$ for both PREX-II and CREX beam energies.	42
2.20	Moller Polarimeter	43
2.21	Schematic plot of Hall A beam monitor system and beam modulation system	44
2.22	Schematic plot of stripline BPM	45
2.23	Hall A BCM system [?]	46
2.24	Up: Schemtaic plot of current convertor; Down: TM_{010} and TM_{110} modes, the red arrows are electric field	46
2.25	Layout of SAMs[?]	47
2.26	Scattering chamber of PREX-II/CREX	49
2.27	Production target ladder and calibration ladder	49
2.28	Raster pattern with different frequency difference between X and Y. Left: $ f_y - f_x = 120\ Hz$; Right: $ f_y - f_x = 8 * 120\ Hz$. The raster shape is a $4 \times 4\ mm$ square.	51
2.29	Picture of Pb targets after running, one can see clearly the shape of raster.	51
2.30	How the target temperature change with size of raster area.	51

2.31	Side and top view of beamline collimator. Beam from left to right.	52
2.32	Left: a simple model of target degradation – assumming the inner foil (t_1) is becoming thinner and the outer foil is becoming thicker (t_2) while the total mass keeps intact. The plot showes how the power deposition on the beamline collimator change in this model. Middle and Right: actual neutron and photon radiation level monitored along charge accumulation. They show similar trends.	53
2.33	Front picture of beamline collimator and sieve slit collimators, looking downstream. One can clearly see a cylinder removed from the central collimator. The sieve planes lie after the beamline collimator and are movable like a door, it can be opened or closed remotely.	53
2.34	Left: septum (the red coils) in the pivot region; Right: picture of septum.	54
2.35	Schematic plot of HRS and particle rays inside it. [?] The 'focal plane' in the middle plot, by design, should be at an angle of 45° w.r.t the central ray, but is actually rotated to 70° due to lackness of sextupole winding in Q3. When we talk about the HRS focal plane, we usually refer to the VDC lower plane.	55
2.36	Picture of Q1 collimator pairs	55
2.37	The detector package	56
2.38	Schematic plot of VDCs showing UV wires [?]	56
2.39	Left: CAD drawing of the quartz detector; Middle: schematic plot of Cherenkov radiation, the angle between electron and the Cherenkov radiation is $\cos \theta = \frac{v_c}{v_e} = \frac{c}{nv_e} = \frac{1}{n\beta} \approx \frac{1}{n}$; Right: electron flux goes through a quartz detector.	57
2.40	Simulation result of photo-electron (PE) spectrum for single electron passing through the main detectors. The wider tail in the downstream detector is due to particle showering in the upstream quartz. Plot from Devi Adhikari.	58
2.41	Data of x,y distribution on quartz. Plots from Devi Adhikari.	59
2.42	Scatter plot of electrons on the AT monitor plane. Red and blue represent events with opposite transverse polarization.	60
3.1	Charge accumulation versus time (left) and run number (right). The long plateau on the left plot is due to Covid shutdown, which is shown around run 7500 on the right plot. We see that data taking is most efficient after AT (before Covid), the last month (after Covid) is not bad while the first 2 months is not so efficient due to various problems.	62
3.2	Statistics of CREX runs	62
3.3	For CREX, $t_{\text{settle}} = 90 \mu\text{s}$, to allow the PC stablizes after flipping, avoiding any cross effect from last helicity state. The deputy factor is 98.92%.	63

Acknowledgements

text of acknowledgement

Remember to remove it after completing your thesis.

- pdfpageheight (pdfforwidth) – 598.14806pt(845.90042pt) – page height and width
- baselineskip – 15.0pt – vertical distance between two nearby lines; set it to change line gap
- left (right) margin –

Chapter 1

Introduction

The Pb Radius EXperiment-II (PREX-II) and Ca48 Radius EXperiment (CREX) are high-precision experiments that measure the tiny parity-violating (PV) asymmetry (at part per million (ppm) level) of longitudinally polarized electrons scattered off neutron-rich targets (^{208}Pb and ^{48}Ca), from which the weak form factors, weak charge and neutron distribution, and finally neutron skin thickness of those nuclei will be extracted.

The PV asymmetry (\mathcal{A}_{pv}) comes from the interference between the electromagnetic (EM) and (neutral) weak one-boson exchange amplitude, because weak interaction doesn't conserve the parity symmetry. While the EM interaction has been studied thoroughly, the asymmetry measurement allows us to derive the weak charge and therefore the neutron distribution in a nucleus.

Parity-violating electron scattering (PVES) experiments require high energy polarized electron beam, which was provided by the Continuous Electron Beam Accelerator Facility (CEBAF) at Thomas Jefferson National Accelerator Facility (TJNAF, also known as JLab). The excellent beam qualities and dedicated instrumentations at JLab allowed the measurements to be statistics limited.

1.0.1 Neutron Radius and Neutron Skin

What's the size of a nucleus? Given the development of modern physics, many people may think there is a clear answer to this basic question. Unfortunately, we don't. Of course, one may estimate a nuclear radius as $R = cA^{1/3}$, where A is the mass number and c is an approximative constant coefficient that can be experimentally identified ($\sim 1.20 \text{ fm}$ [?]). But this picture is over simplified and can't help in cases where precise nucleon distribution is needed. Physicists do have calculated and precisely measured the proton radius of many nuclei, but neutron, due to its neutrality, remains as a stubborn obstacle in our understanding toward the structure of nuclei. Especially for heavy nuclei, where more neutrons than protons are needed to bound the nuclei, it is neutron radius rather than proton radius that defines the size of a heavy nucleus.

When we talk about the proton or neutron radius, it is actually a concept under the framework of Quantum Mechanics (QM), rather than the radius of any objects that we

are familiar with in our daily life. In QM, particles are represented by a probability wave function, so the neutron (proton) Root-Mean-Square (RMS) radius is defined as:

$$R_{p,n} \equiv \langle R_{p,n}^2 \rangle^{1/2} = \sqrt{\frac{\int d^3\mathbf{r} r^2 \rho_{p,n}(\mathbf{r})}{\int d^3\mathbf{r} \rho_{p,n}(\mathbf{r})}} \quad (1.1)$$

where $\rho(\mathbf{r})$ is the nucleon density at position \mathbf{r} , which satisfies the normalization condition:

$$\int d^3\mathbf{r} \rho_{p,n}(\mathbf{r}) = 1$$

Searching through the literatures, we can find many works on the high-precision (with an error $\leq 0.02 \text{ fm}$) measurement of the proton (charge) radius (R_p) of many nuclei through atomic and nuclear experiments [18, 19] but not much precise data about the neutron radius (R_n). The difficulties lie in that neutrons are electrically chargeless, so one can measure its size only through strong or weak interaction. Both methods suffer from their own limitations: the weak interaction is too weak (compared to the background EM interaction) to measure it directly, therefore people turn to PV asymmetry measurement, which is also tiny, much effort is needed during experiments; while the strong interaction has large theoretical uncertainties from the low energy non-perturbative Quantum Chromodynamics (QCD), the interpretation of hadronic measurement is usually model dependent. Though of these difficulties, there have been many effort from the community to explore the different aspects of neutron radius (and neutron skin thickness): the hadronic probe includes pion [?], proton [?], antiproton [?] and alpha particle [?]; atomic experiments like electric dipole polarizabilities [?] and pygmy dipole resonances [?] also provide input to our understanding. Experimentally, the best resolution we got about R_n is about 5%. (FIXME) Theoretically, The best estimates of R_n appear to come from nuclear theory, where models have been constrained primarily by data other than measurements of neutron radii. Therefore, a measurement of R_n will provide a powerful independent check of basic nuclear theory.

Experimentally, the nucleon radius is measured from their corresponding form factors (FFs). According to QM, under Born approximation, the matrix element (ME) for a

scattering process is (assuming a Coulomb-like potential):

$$\begin{aligned}
\mathcal{M}_{fi} &= \langle \Psi_f | V(\mathbf{r}) | \Psi_i \rangle = \int e^{-i\mathbf{p}_f \cdot \mathbf{r}} V(\mathbf{r}) e^{i\mathbf{p}_i \cdot \mathbf{r}} d^3 \mathbf{r} \\
&= \int e^{i(\mathbf{p}_i - \mathbf{p}_f) \cdot \mathbf{r}} d^3 \mathbf{r} \int \frac{Q_t \rho(\mathbf{r}')}{4\pi |\mathbf{r} - \mathbf{r}'|} d^3 \mathbf{r}' \\
&= \int \int e^{i\mathbf{q} \cdot \mathbf{r}} \frac{Q_t \rho(\mathbf{r}')}{4\pi |\mathbf{r} - \mathbf{r}'|} d^3 \mathbf{r} d^3 \mathbf{r}' \\
&= \int \int e^{i\mathbf{q} \cdot (\mathbf{r} - \mathbf{r}')} \frac{Q_t \rho(\mathbf{r}')}{4\pi |\mathbf{r} - \mathbf{r}'|} e^{i\mathbf{q} \cdot \mathbf{r}'} d^3 \mathbf{r} d^3 \mathbf{r}' \\
&= \int e^{i\mathbf{q} \cdot \mathbf{R}} \frac{Q_t}{4\pi |\mathbf{R}|} d^3 \mathbf{R} \int \rho(\mathbf{r}') e^{i\mathbf{q} \cdot \mathbf{r}'} d^3 \mathbf{r}' \\
&= (\mathcal{M}_{fi})_{\text{point}} F(\mathbf{q})
\end{aligned} \tag{1.2}$$

where Q_t is the total charge. The ME can be factorized into two parts: the scattering amplitude of a point-like nucleus with charge Q_t and a modification due to the inner structure of the target, which is called the FF:

$$F(\mathbf{q}) = \int \rho(\mathbf{r}) e^{i\mathbf{q} \cdot \mathbf{r}} d^3 \mathbf{r} \tag{1.3}$$

which is just the Fourier transformation of the spatial density distribution. Conversely, once we know (measure) the FF at different \mathbf{q} , we can derive the charge distribution:

$$\rho(\mathbf{r}) = \int F(\mathbf{q}) e^{-i\mathbf{q} \cdot \mathbf{r}} d^3 \mathbf{q} \tag{1.4}$$

This tells us how to measure the charge density distribution of a nucleus:

$$F(\mathbf{q}) = \frac{\mathcal{M}_{fi}}{(\mathcal{M}_{fi})_{\text{point}}} = \sqrt{\frac{\sigma_{\text{measured}}}{\sigma_{\text{Mott}}}} \tag{1.5}$$

Though of many precise data points at different \mathbf{q} (most at low q region), there is obviously no way to cover the whole space of \mathbf{q} experimentally, therefore, some phenomenological models are needed to extract charge density distribution.

For a spherically symmetric density distribution, $\rho(\mathbf{r}) = \rho(|\mathbf{r}|) = \rho(r)$, one can calculate the corresponding FF as:

$$\begin{aligned}
F(\mathbf{q}) &= \int \rho(r) e^{iqr \cos \theta} 2\pi r^2 \sin \theta dr d\theta \\
&= 4\pi \int r \rho(r) \frac{\sin(qr)}{q} dr
\end{aligned}$$

One can see that for a Coulomb-like potential, $F(\mathbf{q})$ doesn't depend on the direction of \mathbf{q} , but only its length: q , and for the convention of Lorentz Invariance, people usually

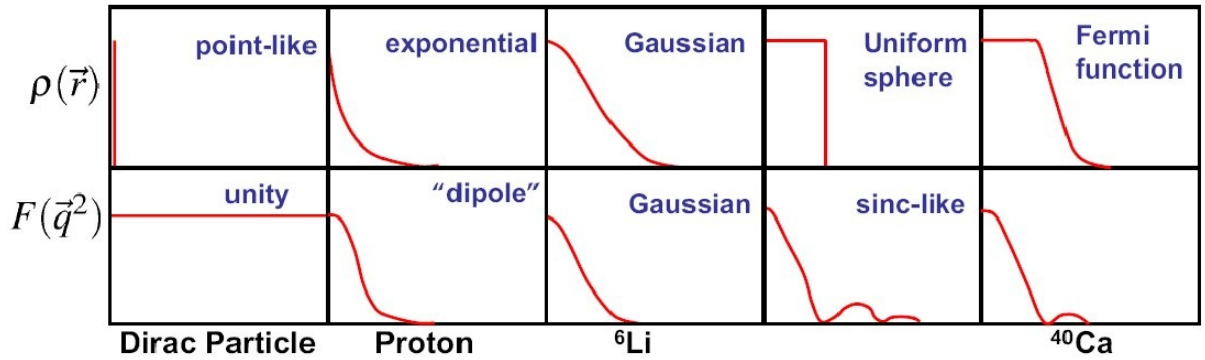


Figure 1.1: Characristic of FF w.r.t. different density distribution functions

write F in terms of $Q^2 = -q^2$, rather than q , so we will use $F(q^2)$ or $F(Q^2)$ hereafter.

Some typical spherically symmetric density distribution and their corresponding FFs are shown in Fig. ??.

At small q^2 limitation, one can do the Fourier expansion:

$$\begin{aligned}
 F(q^2) &= 4\pi \int r\rho(r) \frac{\sin(qr)}{q} dr \\
 &= 4\pi \int \rho(r) r \left(r - \frac{1}{6}q^2 r^3 + \dots \right) dr \\
 &= \int \rho(r) \left(1 - \frac{1}{6}q^2 r^2 + \dots \right) 4\pi r^2 dr \\
 &= 1 - \frac{1}{6}q^2 \langle r^2 \rangle + \dots \\
 &= F(0) + \left. \frac{dF}{dq^2} \right|_{q^2=0} \times q^2 + \dots
 \end{aligned}$$

and easily to get:

$$\langle R^2 \rangle = -6 \left. \frac{dF(q^2)}{dq^2} \right|_{q^2=0} \quad (1.6)$$

This equations prompts how to measure RMS radius: one can measure the FF at some low q^2 points, extrapolate them to $q^2 = 0$, then the slope at $q^2 = 0$ will be the RMS radius (that's why we use the RMS radius rather than the more physical definition of: $\langle R \rangle = \int d^3r r \rho(r)$).

For charged proton, the FF will be the precisely measured EM FF:

$$\langle R_p^2 \rangle = -6 \left. \frac{dF_{EM}(q^2)}{dq^2} \right|_{q^2=0} \quad (1.7)$$

While neutron is neutral, we will measure its RMS radius from its weak charge distribu-

tion:

$$\langle R_n^2 \rangle = -6 \frac{dF_{weak}(q^2)}{dq^2} \Big|_{q^2=0} \quad (1.8)$$

The difference between them will be what we called the neutron skin thickness

$$R_{skin} = R_n - R_p \quad (1.9)$$

The neutron skin, as its name implies, is founded in neutron-rich isotopes that have more neutrons than protons. An intuitive picture is following: analog to atomic electron shell model, protons and neutrons also arrange themselves on shelves from low to high energy, without disturbing each other (nuclear shell model). The higher the energy level, the larger the orbit (radius). For most nuclei, they have similar number of proton and neutron, therefore an approximative proton and neutron radius. But for neutron-rich isotopes, the extra neutrons need to stay on higher energy shell after filling all low energy ones, forming a larger radius than proton and therefore the neutron skin.

Of course, this picture is too simple to fully understand the neutron skin. One quick question will be how can one ensure that the extra neutrons lies in the surface rather than the core area? That's related to the symmetry energy, more specifically, the density dependence of the symmetry energy. Because the core area has a higher nucleon density than the surface, and symmetry energy represents the penalty for breaking the proton-neutron symmetry: the higher the density, the larger the symmetry energy, therefore the lower the binding energy (the energy needed to break down a nuclear system: $BE(N, Z) = M(N, Z)c^2 - Zm_p c^2 - Nm_n c^2$), the less stable the nuclei. So it is symmetry energy that pushes extra neutrons to the surface, which is the deeper reason for the formation of neutron skin.

Experimental hints of the existence of the neutron skin comes from optical isotope shifts (FIXME)

1.0.2 Theoretical Models

Though we don't know the actual neutron distribution, one would not expect too much difference between the proton and neutron distributions, and we know the proton distribution very well, through elastic ep scattering. The scattering cross section is:

$$\frac{d\sigma}{d\Omega} = \left(\frac{d\sigma}{d\Omega} \right)_{Mott} |F(q^2)|^2 \quad (1.10)$$

FF encodes information about the charge structure of a nucleon, it is an interference effect, finite size of the scattering center introduces a phase difference between different plane waves scattered from different points in space.

Consider the simplest hard ball model:

$$\rho(r) = \begin{cases} \frac{3}{4\pi R^3} & r \leq R \\ 0 & r > R \end{cases}$$

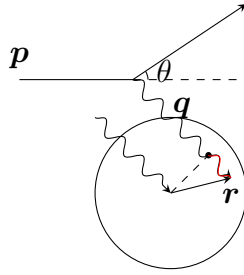


Figure 1.2: As we can see, the virtual photon wave absorbed by a nucleon at position \mathbf{r} will travel a further distance $\mathbf{q} \cdot \mathbf{r}$ than the one absorbed at the central point, therefore a phase difference $e^{i\mathbf{q}\mathbf{r}/\hbar}$

Then the FF will be:

$$F(q^2) = \frac{3}{(qR)^3} (\sin(qR) - qR \cos(qR))$$

where $q = 2p \sin(\theta/2)$

Given the Mott cross section:

$$\left(\frac{d\sigma}{d\Omega} \right)_{Mott} = \begin{cases} \frac{Z^2 \alpha^2}{4E^2 \sin^4(\theta/2)} \cos^2(\theta/2) & \text{light nuclei } Z\alpha \ll 1 \\ \frac{Z^2 \alpha^2}{4E^2 \sin^4(\theta/2)} \cos^2(\theta/2) \left[1 + \pi Z \alpha \frac{\sin(\theta/2)(1 - \sin(\theta/2))}{\cos^2(\theta/2)} \right] & \text{medium nuclei} \end{cases} \quad (1.11)$$

We can draw the cross section, as a function of scattering angle in Fig. 1.3.

Well, the hard ball model doesn't reproduce the experimental distribution, it does characterize the real distribution and show us how FF modify the Mott cross section: the oscillating dips. As it turns out, a more realistic model will be the Saxon-Woods distribution (also called the Fermi 2-parameter model or the Fermi distribution):

$$\rho(r) = \frac{\rho(0)}{1 + \exp((r - R)/t)} \quad (1.12)$$

where $R = (1.2A^{1/3} - 0.48) \text{ fm}$ denotes the nuclear force radius, and $t = 0.4 - 0.5 \text{ fm}$ for $A > 40$. The right plot on Fig. 1.3 uses a fine tuned Fermi 3-parameter model, which fits quite well with the data. More detailed discussion about the Fermi distribution can be found in [20].

One theoretical model based on the Fermi distribution is the FSUGold [21], the neutron distribution of ^{208}Pb predicted by FSUGold is shown in Fig. ??.

We also need to note that for medium and heavy nuclei, the Born approximation doesn't hold, where the incoming and outgoing waves are treated as plane waves. In reality, the waves are distorted by the intense nuclear EM field, making them no longer plane waves any more. So we have to take into account the Coulomb distortion effect, which will modify the PV asymmetry significantly. Coulomb distortion can be understood as multiple EM interactions with the same nucleus, so the distortion correction is

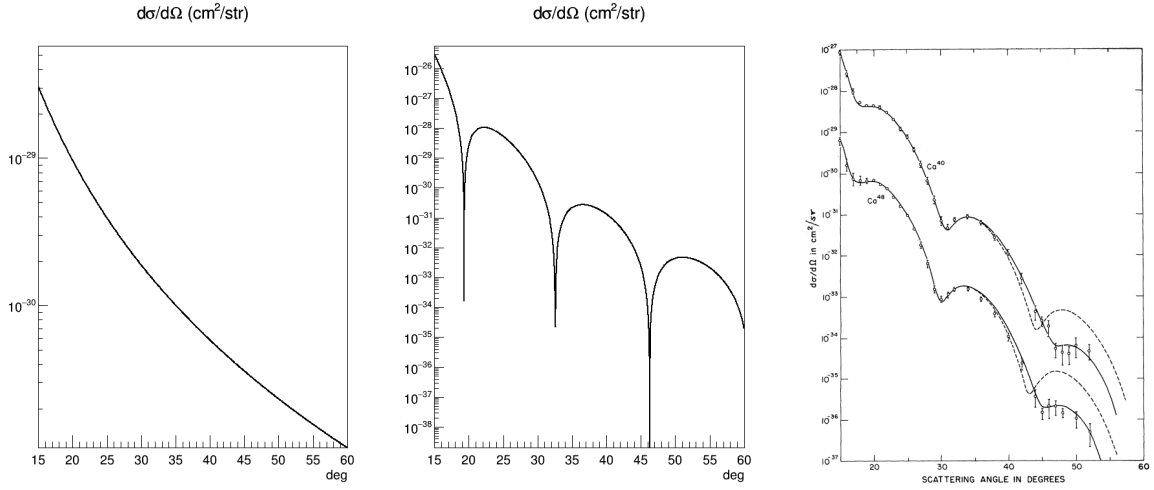


Figure 1.3: Left: Mott cross section of electron elastically scattered off a Ca48 target. Parameters: $p = E = 757.5 \text{ MeV}$. Middle: cross section of electron elastically scattered off Ca48 with the hard ball model (1.0.2). Parameters: $E = 757.5 \text{ MeV}$, $R = A^{1/3} \text{ fm}$. Right: experimental values (dots) and theoretical prediction (solid line), their calculation assumed the charge distribution as a Fermi 3-parameter function. $\rho(r) = \frac{\rho_0(1+\omega r^2/c^2)}{1+\exp((r-c)/a)}$. The ^{48}Ca (^{40}Ca) cross sections are multiplied by 10^{-1} (10) to separate them. [1]

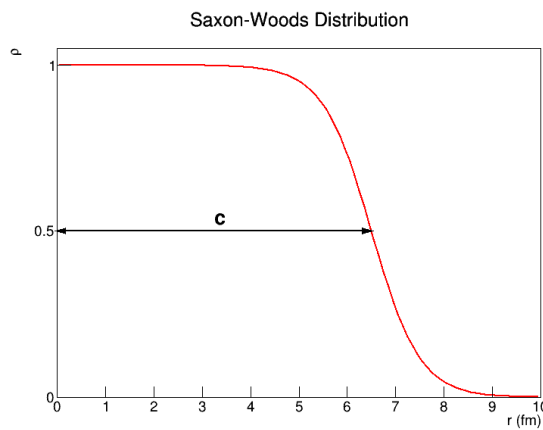
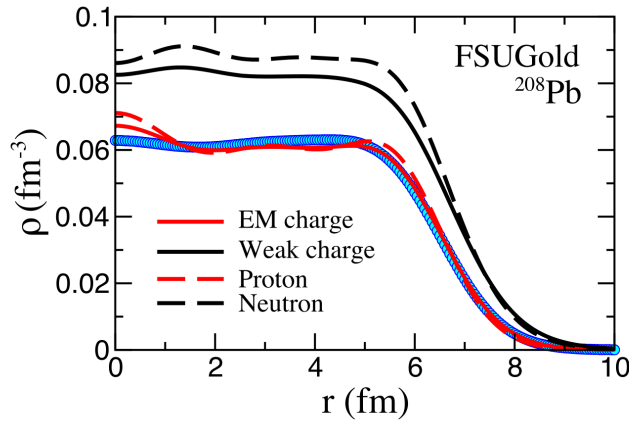


Figure 1.4: In nuclear Shell Model, it is assumed that nucleons occupy different eigenstates of the same spherically symmetric average potential. This potential, unlike that in atomic shell model, needed to be guessed. It turns out that the Saxon-Woods model is a good candidate: $V(r) = -\frac{V(0)}{1+\exp((r-c)/a)}$ (c is the half-height radius and a represents diffuseness of the distribution). Because the potential is formed by all nucleons, so it is approximatively proportional to the nucleon density, therefore the same distribution for nucleon density.



proportional to $Z\alpha$. Obviously, this correction is more important for ^{208}Pb because of its large Z value, Coulomb distortion could reduce the PV asymmetry by as much as 30% as we can see in the following plots.

With these information, one is able to solve the Dirac equation directly to know the PV asymmetry, as shown in the following 2 plots:

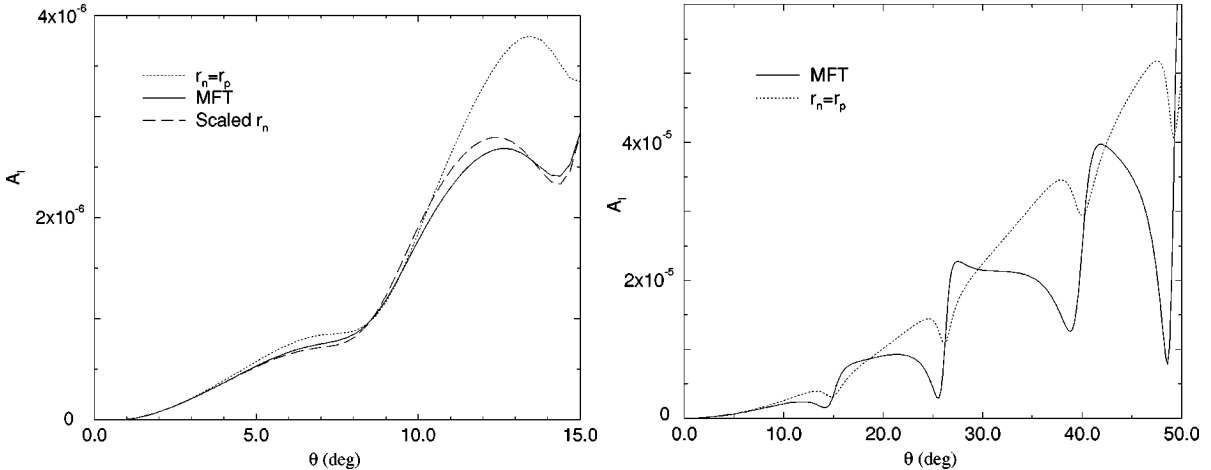


Figure 1.5: PV asymmetry for ^{208}Pb and ^{48}Ca versus scattering angle at 850 MeV (Coulomb distortion correction included). The dotted curve assumes the same weak and charge distribution, while the solid curve is based on relativistic Mean Field Densities. The dashed curve in ^{208}Pb plot uses 3 parameter Fermi distribution [2]

1.1 Symmetry Energy

It has long been a hot topic for nuclear scientists to study how the asymmetry between number of proton and nucleon will affect nuclei, especially the binding energy, which hints us the limit of new isotope elements. Using the simplest Liquid Drop Model (LDM), we

will get the Bethe-Weizsacker Semi-empirical Mass Formula:

$$E \text{ (MeV)} = a_V A - a_S A^{2/3} - a_C \frac{Z(Z-1)}{A^{1/3}} - a_A \frac{(N-Z)^2}{A} + \delta(A, Z)$$

$$\delta(A, Z) = \begin{cases} +\delta_0 & Z, N \text{ even} \\ 0 & A \text{ odd} \\ -\delta_0 & Z, N \text{ odd (A even)} \end{cases} \quad (1.13)$$

- Volume term: nucleons attract nearest neighbors through strong force ($a_V \sim 16 \text{ MeV}$), reflects the short-range nature of strong interaction.
- Surface term: correction to the volume term – nucleons on the surface aren't completely surrounded by other nucleons
- Coulomb term: EM charge repulsion
- Asymmetry term: Pauli exclusion principle
- Pairing term: spin coupling effect – if N and Z are even, then the nuclei will be stable thanks to the occurrence of 'paired spin'; on the other hand, nuclei with odd number of proton and neutron are usually unstable. ($\delta_0 \sim 1 \text{ MeV}$, slowly decreasing with A)

The first 3 terms are natural and easy to understand, while the 4th term is not so obvious. It is based only on Pauli exclusion principle. In heavy nuclei, more neutrons than protons are needed to balance the repulsion between protons. Due to the Pauli exclusion principle, these extra neutrons' energy will be higher than the rest of nucleons, therefore introducing this correction term.

Regard the nuclear system as a free Fermi gas of protons and neutrons, then the kinematic energy of this system will be:

$$E_k = E_N + E_Z = \frac{3}{5} Z E_F^p + \frac{3}{5} N E_F^n$$

Since the Fermi energy is proportional to $n^{2/3}$

$$E_k = C(Z^{5/3} + N^{5/3})$$

Expanse it in terms of $N-Z$ A , we will get

$$E_k = 2^{-2/3} C \left(A^{5/3} + \frac{5}{9} \frac{(N-Z)^2}{A^{1/3}} \right) + O((N-Z)^4)$$

$$= \frac{3}{5} E_F A + \frac{1}{3} E_F \frac{(N-Z)^2}{A} + O((N-Z)^4)$$

The first term contributes to the volume term and the second term is minus the asymmetry term because E_k contributes to the binding energy negatively.

For a general discussion, we can ignore the 3rd term to focus on the homogeneous nuclear (residual strong) interaction between nucleons, and the 5th term which is too small. Now, we can talk about any nuclear system composed of Z protons (EM chargeless) and N neutrons, rather than just true nuclei. Now we have a simplified equation of state (EoS) for nuclear matter:

$$\begin{aligned} E &= a_V A - a_S A^{2/3} - a_A \frac{(N - Z)^2}{A} \\ e &= \frac{E}{A} = a_V - a_S A^{-1/3} - a_A \frac{(N - Z)^2}{A^2} \end{aligned} \quad (1.14)$$

Actually, we should also discard the second term. Obviously, we can't guarantee any specific shape about the nuclear system; what's more, for what people model with most – the infinite nuclear system, we don't need to consider the surface term at all.

$$\begin{aligned} E &= a_V A - a_A \frac{(N - Z)^2}{A} \\ e &= \frac{E}{A} = a_V - a_A \frac{(N - Z)^2}{A^2} = e_0(A) - a_A \beta^2 \end{aligned} \quad (1.15)$$

Here we define $\beta = \frac{N-Z}{A}$ as asymmetry between the number of protons and neutrons.

For infinite system, density, instead of A , will be a better choice to parameterize the EoS. So we should replace N , Z and A with their corresponding density: ρ_n , ρ_p and ρ ($\beta = \frac{\rho_n - \rho_p}{\rho}$). So we are considering an infinite uniform nuclear system at 0 temperature that interacts only via the nuclear force. For any identified ρ , eq (1.15) will be:

$$e(\rho, \beta) = e(\rho, 0) + S(\rho) \beta^2 + O(\beta^4) \quad (1.16)$$

This is an expansion of the binding energy per nucleon around $\beta = 0$. Due to the isospin symmetry between proton and neutron, any isoscalar quantities F will keep unchanged under $n \leftrightarrow p$ interchange, while isovector quantities G will change sign. β is an isovector, so for a smooth $F(\beta)$, its expansion around $\beta = 0$ has even terms only:

$$F(\beta) = F_0 + F_2 \beta^2 + F_4 \beta^4 + \dots$$

On the other hand, for a smooth $G(\beta)$, its expansion around $\beta = 0$ has odd terms only:

$$G(\beta) = G_1 \beta + G_3 \beta^3 + \dots$$

e is an isoscalar, it doesn't change under $n \leftrightarrow p$ interchange as we can see from eq (1.15). The coefficient $S(\rho) = \frac{\partial^2 e(\rho, \beta)}{\partial \beta^2}$ is what we call the **symmetry energy**, a key parameter in explaining a wide range of nuclear properties and phenomena. It describes how much energy will be released when exchange all protons into neutrons for a symmetric

nuclear system.

Not only is S itself important, but also its dependence on ρ . By convention, $S(\rho)$ is expanded around the nuclear saturation density ρ_0 (following the free Fermi gas assumption):

$$S(\rho) = S(\rho_0) + \frac{dS}{d\rho} \bigg|_{\rho_0} (\rho - \rho_0) + \frac{1}{2} \frac{d^2S}{d\rho^2} \bigg|_{\rho_0} (\rho - \rho_0)^2 + \frac{1}{6} \frac{d^3S}{d\rho^3} \bigg|_{\rho_0} (\rho - \rho_0)^3 + \dots \quad (1.17)$$

From which, we have some auxiliary parameters defined:

$$\begin{aligned} S_0 &= S(\rho_0) \\ L &= 3\rho_0 \frac{dS}{d\rho} \bigg|_{\rho_0} \\ K_{sym} &= 9\rho_0^2 \frac{d^2S}{d\rho^2} \bigg|_{\rho_0} \\ Q_{sym} &= 27\rho_0^3 \frac{d^3S}{d\rho^3} \bigg|_{\rho_0} \end{aligned} \quad (1.18)$$

Among them, L represents S 's dependence on ρ .

Take neutron star [22] as an example, it has most neutrons and a few protons, so its $\beta = 1$.

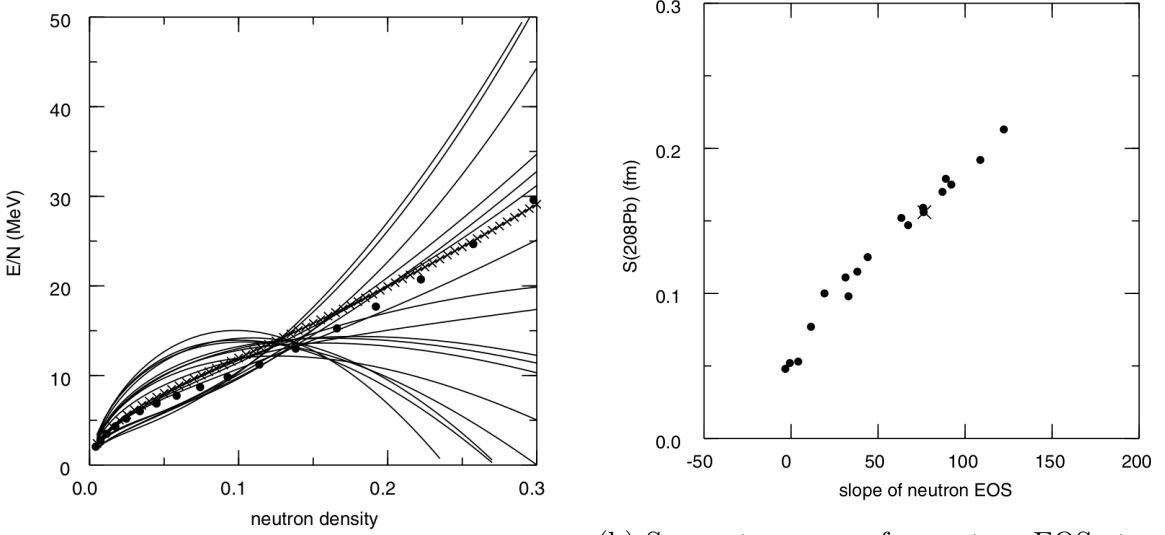
$$\begin{aligned} E &= E_0 + S \\ P &= \rho^2 \frac{dS}{d\rho} \approx \frac{L\rho^2}{3\rho_0} \\ RP^{-1/4} &\approx const \end{aligned} \quad (1.19)$$

The amazing thing is that neutron star's pressure dependents on L is proportional to R^4 . Once we know the L value, we will know the pressure and therefore the radius of a neutron star.

Being such an important parameter, a great effort has been done to extract S and L . Comparing (1.15) and (1.16), we can directly get:

$$S(\rho) \approx -a_A \quad (1.20)$$

But this tells us only the symmetry energy at nuclear density ($1.22 \times 10^{44} m^{-3}$), what about the symmetry energy at other density values? Especially at the nuclear saturation density ($\sim 1.7 \times 10^{44} m^{-3}$)? And what about its density dependence? Another strategy is the energy density functionals (EDF), which fits the binding energy throughout the nuclear mass table to find out the best EDF, then use it to calculate $S(\rho)$. Fitting parameterizations are constrained by nuclear density, proton RMS radii and nuclear binding energies. The problem is many EDFs can fit equally well with these constrains, but have quite different L values, as shown in Fig. ???. If there is a experiment that can identify S (L) value without model dependence, then no doubt it will help a lot in understanding



(a) Neutron EOS for 18 Skyrme parameter sets. The filled circles are the Friedman-Panharipande (FG) variational calculations and the crosses are SkX. [?] We can see different models have very different symmetry energies.

(b) Symmetry energy for neutron EOS at $\rho_n = 0.1 \text{ neutron/fm}^3$ (in units of $\text{MeV fm}^3/\text{neutron}$) vs the S value in ^{208}Pb for 18 Skyrme parameter sets. The cross is SkX. Determination of S in ^{208}Pb will greatly constrain the possible candidates.

the symmetry energy and the EoS.

The method to measure L in lab is to measure the neutron skin thickness of neutron rich nuclei. For symmetric nuclei ($N = Z$), the protons and neutrons are expected to distribute uniformly. While for neutron-rich nuclei, the extra neutrons are pushed out against the surface tension[23], therefore forming a neutron skin.

Neutron skin and neutron star, though of their 18 orders of magnitude difference in size (fm vs km), both are neutron-rich nuclear matter and governed by the same physical laws: eq (1.19). So by measuring the neutron skin thickness, we can derive P and L values, for the study of neutron stars and nuclear EoS.

1.2 Physics Beyond the Standard Model (SM)

Parity-Violating Electron Scattering is always a promising avenue for physics beyond the SM in precision frontier. Flavor conserving interaction:

$$|A_\gamma + A_Z + A_{new}|^2 \rightarrow A_\gamma^2 \left[1 + 2\frac{A_Z}{A_\gamma} + 2\frac{A_{new}}{A_\gamma} \right]$$

1.3 Asymmetry

To explain the beta decay, Fermi proposed the 4-fermion interaction (Fermi's interaction) in 1933 [?], which is a low-energy limit of the weak interaction. In his theory,

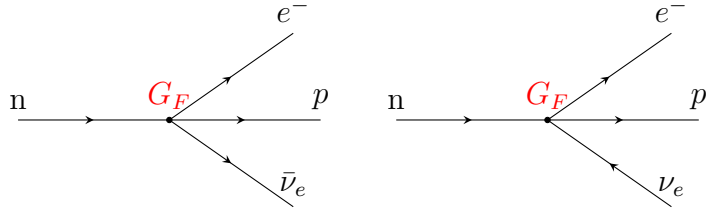


Figure 1.7: Fermi's interpretation of beta decay, current $j_{n \rightarrow p}$ convert n into p and current $j_{\nu_e \rightarrow e}$ creates $(e, \bar{\nu}_e)$ pair.

In analogy to the EM interaction (emission of a photon by an electron: $\mathcal{M} = ej_\mu^{em} A^\mu$) Fermi interpreted the β decay as emission of a $(e, \bar{\nu}_e)$ pair, during the process neutron converts itself into a proton, therefore coupling of two current:

$$\mathcal{M} = G_F (\bar{p} \mathbb{O}^\mu n) (\bar{e} \mathbb{O}_\mu \nu_e) = G_F j_{(n \rightarrow p)}^\mu j_\mu^{(\nu_e \rightarrow e)} \quad (1.21)$$

Where $G_F = 1.166 \times 10^{-5} \text{ (GeV)}^{-2}$ is the coupling constant that will be experimentally determined and \mathbb{O} represents the possible operators. Out of the 5 possible Lorentz invariant bilinear forms (Scalar (S: $\mathbb{O} = \mathbb{1}$), pseudoscalar (P: $\mathbb{O} = \gamma^5$), Vector (V: $\mathbb{O} = \gamma^\mu$), Axial vector (A: $\mathbb{O} = \gamma^\mu \gamma^5$) and Tensor (T: $\mathbb{O} = \sigma^{\mu\nu} = \frac{i}{2}(\gamma^\mu \gamma^\nu - \gamma^\nu \gamma^\mu)$), Fermi selected the vector current to keep in line with the EM interaction: $j^\mu = \bar{u} \gamma^\mu u$.

In 1956, T. D. Lee and C. N. Yang, both being Fermi's student, postulated the revolutionary idea of parity violation for solving the $\tau - \theta$ puzzle, and they succeeded. Only one year later, their hypothesis was experimentally tested by Wu etc in the decay of polarized Co^{60} nuclei, establishing the fact that parity is not conserved in weak interaction and therefore the weak current is not a pure vector-like quantity. Based on the experimental fact that parity is maximally violated [24], Sudarshan and Marshak [?], also Feynmann and Gell-Mann [?] updated Fermi's theory by replacing the vector current with a new current to accomodate parity violation, which led us to:

$$\mathcal{M} = \frac{G_F}{\sqrt{2}} (\bar{p} \gamma^\mu (\mathbb{1} - \gamma^5) n) (\bar{e} \gamma_\mu (\mathbb{1} - \gamma^5) \nu_e) \quad (1.22)$$

The factor of $\frac{1}{\sqrt{2}}$ was introduced to keep G_F unchanged (Fermi's original theory was not aware the fact that neutrino was left-handed only, resulting in a decay phase space twice the real value in nature, to fix the problem, we can either modify the value of G_F or introduce a correction factor $\frac{1}{\sqrt{2}}$). The V and A parts of V-A theory refer to the vector and axial vector current, responsible for Fermi transitions and Gamow-Teller transitions respectively.

$$j_V^\mu = \bar{u} \gamma^\mu u \quad j_A^\mu = \bar{u} \gamma^\mu \gamma^5 u \quad (1.23)$$

The form of V-A as $\mathbb{1} - \gamma^5$ happens to be the projection operator:

$$P_R = \frac{\mathbb{1} + \gamma^5}{2} \quad P_L = \frac{\mathbb{1} - \gamma^5}{2} \quad (1.24)$$

By definition of gamma matrix, one can easily verify that:

$$\begin{aligned} \left(\frac{\mathbb{1} - \gamma^5}{2}\right)^2 &= \frac{\mathbb{1} - \gamma^5}{2} & \gamma^\mu \frac{\mathbb{1} - \gamma^5}{2} &= \frac{\mathbb{1} + \gamma^5}{2} \gamma^\mu \\ \gamma^\mu \frac{\mathbb{1} - \gamma^5}{2} &= \frac{\mathbb{1} + \gamma^5}{2} \gamma^\mu \frac{\mathbb{1} - \gamma^5}{2} \end{aligned} \quad (1.25)$$

Then one can see the handness of the new current:

$$\mathcal{M} = \frac{4G_F}{\sqrt{2}} (\bar{p} \gamma^\mu \frac{\mathbb{1} - \gamma^5}{2} n) (\bar{e} \gamma_\mu \frac{\mathbb{1} - \gamma^5}{2} \nu_e) = \frac{4G_F}{\sqrt{2}} (\bar{p}_L \gamma^\mu n_L) (\bar{e}_L \gamma_\mu \nu_{e,L}) \quad (1.26)$$

Only left (right)-handed particle (antiparticle) can interact in weak interaction. In analogy to EM interaction, the coupling constant is proportional to a weak charge (weak isospin T_3), then right-handed fermions (left-handed antifermions) will have $T_3 = 0$ and left-handed fermions have the same weak charge.

Given the fact that the charge current (it changes particle's electric charge) connects 2 types of fermions and lepton number is conserved in weak interaction, it is natural to group them in a lepton doublet: $f_L = \begin{pmatrix} \nu_l \\ l \end{pmatrix}_L$. This implies us that for left-handed fermions: $T = \frac{1}{2}$, $T_3 = \pm \frac{1}{2}$

Applying the V-A theory to more decay and scattering process ($\mu^+ \rightarrow e^+ + \nu_e + \bar{\nu}_\mu$, $\pi^- \rightarrow l + \bar{\nu}_l$ etc.), we have 2 charge currents:

$$j_\mu^- = \bar{\nu}_{e,L} \gamma_\mu e_L \quad j_\mu^+ = \bar{e}_L \gamma_\mu \nu_{e,L} \quad (1.27)$$

which can be written in a more compact way w.r.t. the lepton doublet:

$$j_\mu^\pm = \bar{f}_L \gamma_\mu t^\pm f_L \quad (1.28)$$

where,

$$t^+ = \begin{pmatrix} 0 & 1 \\ 0 & 0 \end{pmatrix} = \frac{1}{2}(\sigma^1 + i\sigma^2) \quad t^- = \begin{pmatrix} 0 & 0 \\ 1 & 0 \end{pmatrix} = \frac{1}{2}(\sigma^1 - i\sigma^2) \quad (1.29)$$

We can see clearly the SU(2) symmetry by the t^\pm expression, the raising (t^+) and lowing matrices (t^-) are the combination of the first 2 Pauli matrices. Then one should consider the third component:

$$j_\mu^3 = \bar{f}_L \gamma_\mu \frac{1}{2} t^3 f_L = \frac{1}{2} (\bar{\nu}_{e,L} \gamma_\mu \nu_{e,L} - \bar{e}_L \gamma_\mu e_L) \quad (1.30)$$

This is a neutral current. But what does this neutral current represents for? The then only known neutral current is the EM current, but neutrino is neutral, how could it have a EM neutral current? The neutral current kept as a mystery until Glashow, Salam and Weinberg postulated the GSW model, which interpretes j^3 as part of a more complete neutral current that includes j^{em} – the so called $SU(2)_L \times U(1)$.

One problem with Fermi's theory is that the cross section ($\sigma \sim G_F^2 E^2$) will diverge at high energy, to which the solution was the introduction of mediating mesons: W^\pm . Unlike photon that mediates EM interaction, W boson is charged, and has a heavy mass implied from the short-range nature of the weak interaction. The introduction of W fields just make the weak interaction more similar to the EM interaction:

$$\mathcal{L} = g_W (J^+ W^+ + J^- W^-) \quad (1.31)$$

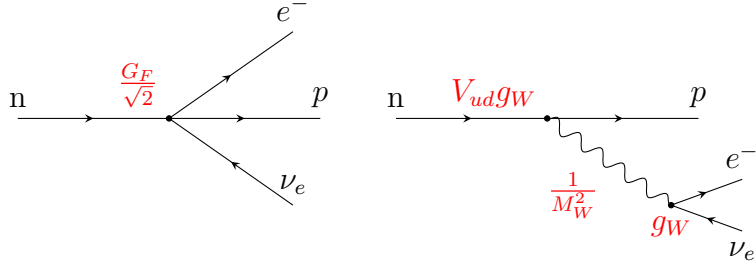


Figure 1.8: W-boson exchange picture of β decay

Given the similarity between weak interaction and EM interaction, it is natural to unify them into a multiplet of gauge fields. Based on Yang and Mills' non-abelian gauge theory, Salam and Weinberg successfully came up with a unified framework for both interactions – the $SU(2)_L \times U(1)$ structure firstly suggested by Glashow. The $SU(2)$ part is generated by ‘weak isospin’, the subscript L refers to the fact that only left-handed fermions couple to gauge boson of $SU(2)$, and the $U(1)$ part comes from the ‘weak hypercharge’. There are 4 vector bosons:

$$W^1, W^2, W^3, B$$

These bosons will couple to both left-handed and right-handed fermions. For simplicity, let's consider only the first generation leptons here:

$$\psi_1 = \begin{pmatrix} \nu_e \\ e^- \end{pmatrix} \quad \psi_2 = \nu_{e,R} \quad \psi_3 = e_R^- \quad (1.32)$$

For the left-handed doublet ψ_1 , it interacts to all bosons, so the covariant derivative is:

$$D_\mu = \partial_\mu - ig \frac{\sigma^a}{2} W_\mu^a - ig' y_1 B_\mu \quad (1.33)$$

where y_1 is the hypercharge of ψ_1 . The corresponding coupling Lagrangian is:

$$\mathcal{L}_{int,L} = -i \bar{\psi}_1 \gamma^\mu (g \frac{\sigma^a}{2} W_\mu^a + g' y_1 B_\mu) \psi_1 = -i (g \bar{\psi}_1 \gamma^\mu W_\mu + g' y_1 \bar{\psi}_1 \gamma^\mu \psi_1 B_\mu) \quad (1.34)$$

For right-handed singlets, they don't couple to weak vector bosons, therefore the covari-

ant derivative for right-handed fermions is:

$$D_\mu = \partial_\mu - ig'y_{2(3)}B_\mu \quad (1.35)$$

$y_{2(3)}$ are the hypercharge of $\psi_{2(3)}$ and the Lagrangian:

$$\mathcal{L}_{int,R} = -ig'(y_2\bar{\psi}_2\gamma^\mu\psi_2 + y_3\bar{\psi}_3\gamma^\mu\psi_3)B_\mu \quad (1.36)$$

So the complete interacting Lagrangian is:

$$\mathcal{L}_{int} = \mathcal{L}_{int,L} + \mathcal{L}_{int,R} = -i(g\mathbf{j}^\mu\mathbf{W}_\mu + g'j_Y^\mu B_\mu) \quad (1.37)$$

where \mathbf{j}^μ is the weak isospin current, it couples to a weak isotriplet of vector bosons: $\mathbf{W} = (W^1, W^2, W^3)$ with coupling strength g ; and the weak hypercharge current $j_Y^\mu = \sum_{i=1}^3 y_i\bar{\psi}_i\gamma^\mu\psi_i$ couples to an isosinglet vector boson: B^μ with strength g' .

Because the GSW model preserve the SU(2) structure we talked about before, therefore it is obvious to reproduce the charged current:

$$W^\pm = \frac{1}{\sqrt{2}}(W^1 \mp iW^2) \quad j^\pm = j^1 \pm ij^2 \quad (1.38)$$

$$j^1W^1 + j^2W^2 = \frac{1}{\sqrt{2}}(j^+W^+ + j^-W^-) \quad (1.39)$$

As for the other 2 bosons, there is no way to satisfy $y_1 = y_2 = y_3$ and $g'y_i = eQ_i$ at the same time, so B is not pure A. Since both fields are neutral, one can try to mix them, and get some result matching experimental results:

$$\begin{pmatrix} A \\ Z \end{pmatrix} = \begin{pmatrix} \cos\theta_W & \sin\theta_W \\ -\sin\theta_W & \cos\theta_W \end{pmatrix} \begin{pmatrix} B \\ W^3 \end{pmatrix} \Leftrightarrow \begin{pmatrix} B \\ W^3 \end{pmatrix} = \begin{pmatrix} \cos\theta_W & -\sin\theta_W \\ \sin\theta_W & \cos\theta_W \end{pmatrix} \begin{pmatrix} A \\ Z \end{pmatrix} \quad (1.40)$$

The mixing angle is known as the Weinberg angle.

Rewrite eq. 1.37 in terms of W^\pm , Z and A :

$$\begin{aligned} i\mathcal{L} &= \frac{g}{\sqrt{2}}(j^+W^+ + j^-W^-) \\ &+ \sum_{i=1}^3 \bar{\psi}_i\gamma^\mu \left\{ \left[g\frac{\sigma^3}{2}\sin\theta_W + g'y_i\cos\theta_W \right] A_\mu + \left[g\frac{\sigma^3}{2}\cos\theta_W - g'y_i\sin\theta_W \right] Z_\mu \right\} \psi_i \end{aligned} \quad (1.41)$$

where $g_W = g/\sqrt{2}$ is the coupling constant of weak charged current.

The neutral part can be expressed in corresponding charge:

$$\begin{aligned} i\mathcal{L}_{NC} &= \sum_{i=1}^3 \bar{\psi}_i\gamma^\mu\psi_i [(g\sin\theta_W I_3 + g'\cos\theta_W Y) A_\mu + (g\cos\theta_W I_3 - g'\sin\theta_W Y) Z_\mu] \\ &= ej_{EM}^\mu QA_\mu + g_Z j_Z^\mu Q_Z Z_\mu \end{aligned} \quad (1.42)$$

Where I_3 is the weak isospin and Y is the weak hypercharge; Similarly, Q is the EM charge in unit of electron charge and Q_Z is the weak neutral charge. e and g_Z are coupling constant for EM and neutral weak interaction respectively. With I_3 and Y vary for different fermions, we have the following relationship:

$$e = g \sin \theta_W = g' \cos \theta_W = \frac{gg'}{g^2 + g'^2} \quad (1.43)$$

So the Weinberg angle is identified as:

$$\tan \theta_W = \frac{g'}{g} \quad (1.44)$$

and:

$$Y = Q - I_3 \quad (1.45)$$

The value of weak hypercharge depends on the definition, if one keep the $\frac{1}{2}$ factor in the B current, then one will get:

$$\frac{Y}{2} = Q - I_3 \Rightarrow Y = 2(Q - I_3) \quad (1.46)$$

This is the traditional formula. In this thesis we will use the definition of eq. 1.45.

As for neutral weak current, the value of g_Z , Q_Z and J_Z dependent on our choice, as long as:

$$g_Z Q_Z J_Z = (g \cos \theta_W I_3 - g' \sin \theta_W Y) \bar{\psi} \gamma^\mu \psi \quad (1.47)$$

The traditional choice is:

$$\begin{aligned} g_Z &= \frac{g}{\cos \theta_W} = \frac{e}{\sin \theta_W \cos \theta_W} \\ Q_Z &= I_e \cos^2 \theta_W - Y \sin^2 \theta_W = I_3 - Q \sin^2 \theta_W \end{aligned} \quad (1.48)$$

One can also absorb Q_Z into J_Z to get:

$$J_Z = \sum \bar{\psi}_i \gamma^\mu (I_3 - Q \sin^2 \theta_W) \psi_i = \sum_f \bar{f} \gamma^\mu \frac{c_v - c_a \gamma^5}{2} f \quad (1.49)$$

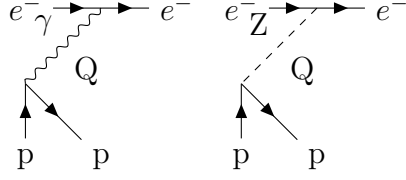
with

$$c_v = I_3 - 2Q \sin^2 \theta_W \quad c_a = I_3 \quad (1.50)$$

So we come to a striking prediction of the GSW model: the neutral weak interaction, which was experimentally observed in 1973 in the Gargamelle neutrino experiment [25].

What we are going to observe in PREX-II and CREX exactly originates from this neutral weak current.

$$\mathcal{A}_{pv} = \frac{\frac{d\sigma^R}{d\Omega} - \frac{d\sigma^L}{d\Omega}}{\frac{d\sigma^R}{d\Omega} + \frac{d\sigma^L}{d\Omega}} = \frac{|\mathcal{M}^R|^2 - |\mathcal{M}^L|^2}{|\mathcal{M}^R|^2 + |\mathcal{M}^L|^2}$$



where: $\mathcal{M}^{R,L} = \mathcal{M}_\gamma + \mathcal{M}_Z^{R,L}$. Because EM amplitude is much larger than the weak amplitude: $\mathcal{M}_\gamma \gg \mathcal{M}_Z^{R,L}$

$$\begin{aligned}
\mathcal{A}_{pv} &\approx \frac{2\mathcal{M}_\gamma(\mathcal{M}_Z^R - \mathcal{M}_Z^L)}{2\mathcal{M}_\gamma^2} \\
&= \frac{\mathcal{M}_Z^R - \mathcal{M}_Z^L}{\mathcal{M}_\gamma} \propto \frac{\frac{d\sigma_{\text{weak}}}{d\Omega}}{\frac{d\sigma_{\text{EM}}}{d\Omega}} \\
&= \left(\frac{\mathcal{M}_Z^R - \mathcal{M}_Z^L}{\mathcal{M}_\gamma} \right)_{\text{point}} \times \frac{Q_{wk}}{Z} \frac{F_{wk}(Q^2)}{F_{ch}(Q^2)} \\
&\approx \frac{g_Z^2/M_Z^2}{e^2/Q^2} \frac{(j_Z^{e,R} - j_Z^{e,L})j_Z^n}{j_\gamma^e j_\gamma^p} \times \frac{Q_{wk}}{Z} \frac{F_{wk}(Q^2)}{F_{ch}(Q^2)} \quad (Q^2 \ll M_Z^2) \\
&= -\frac{8G_F/\sqrt{2}}{4\pi\alpha/Q^2} \frac{(\bar{e}_L\gamma^\mu I_3 e_L)_{\frac{1}{2}}(\bar{n}_L\gamma_\mu I_3 n_L)}{(\bar{e}_L\gamma^\mu e_L)(\bar{p}\gamma_\mu p)} \times \frac{Q_{wk}}{Z} \frac{F_{wk}(Q^2)}{F_{ch}(Q^2)} \\
&= -\frac{G_F Q^2}{4\pi\alpha\sqrt{2}} \frac{Q_{wk}}{Z} \frac{F_{wk}(Q^2)}{F_{ch}(Q^2)}
\end{aligned} \tag{1.51}$$

The weak isospin for electron and neutron is: $I_3(e^-) = I_3(n) = -\frac{1}{2}$. The factor of $\frac{1}{2}$ in line 5 of eq. 1.51 arises from the fact that the target is unpolarized.

The FFs can be further decomposed into point nucleon FFs:

$$\begin{aligned}
F_{ch}(q) &= G_{ch}^p(q)F_p(q) + G_{ch}^n(q)F_n(q) \\
&= G_E^p(q)F_p(q) + \frac{N}{Z}G_E^n(q)F_n(q) \\
F_{wk}(q) &= G_{wk}^p(q)F_p(q) + G_{wk}^n(q)F_n(q) \\
&= G_E^p(q) \left[F_n(q) - \frac{Z}{N}(1 - 4\sin^2\theta_W)F_p(q) \right] - G_E^n(q) \left[F_n(q)(1 - 4\sin^2\theta_W) - \frac{Z}{N}F_p(q) \right]
\end{aligned}$$

Where $G_E^p(q)$ and $G_E^n(q)$ are the EW single nucleon FFs, $F_p(q)$ and $F_n(q)$ are the FFs of point proton and neutron density distribution. Compared with $G_E^p(q)$, the charge FF of

the neutron $G_E^n(q)$ can be neglected for small momentum transfer:

$$\begin{aligned} F_p(q) &= \int d^3r j_0(qr) \rho_p(r) \\ F_n(q) &= \int d^3r j_0(qr) \rho_n(r) \\ G_{wk}^p &= q_p G_E^p + q_n G_E^n + q_0 G_E^s \\ G_{wk}^n &= q_p G_E^p + q_n G_E^n + q_0 G_E^s \end{aligned}$$

For weak charges including radiative correction

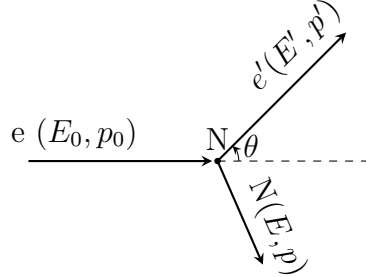
$$q_p \approx 0.0712 \quad q_n = q_0 \approx -0.9877$$

$$\begin{aligned} \frac{F_{wk}(q)}{F_{ch}(q)} &\approx \frac{F_n(q)}{F_p(q)} \\ \mathcal{A}_{pv} &= \frac{G_F Q^2}{4\pi\alpha\sqrt{2}} \frac{Q_{wk}}{Z} \left[\frac{F_n(q)}{F_p(q)} - \frac{Z}{N} (1 - 4 \sin^2 \theta_W) \right] \end{aligned}$$

When ignoring structure (tree level):

$$\mathcal{A}_{pv} = \frac{G_F Q^2}{\pi\alpha\sqrt{2}} \left(\sin^2 \theta_W + \frac{1}{4} \left[\frac{N}{Z} - 1 \right] \right)$$

1.4 Dynamics



4-Momentum conservation

$$E_0 + M = E' + E \quad \mathbf{p}_0 = \mathbf{p}' + \mathbf{p}$$

Assume ($m_e \ll 0 \Rightarrow E_0 \approx p_0$, $E' \approx p'$)

$$\begin{aligned} E^2 &= M^2 + \mathbf{p}^2 = M^2 + (\mathbf{p}_0 - \mathbf{p}')^2 \\ &= M^2 + (E_0 - E' \cos \theta)^2 + (E' \sin \theta)^2 \\ &= M^2 + E_0^2 + E'^2 - 2E_0 E' \cos \theta \\ &= (E_0 + M - E')^2 \end{aligned}$$

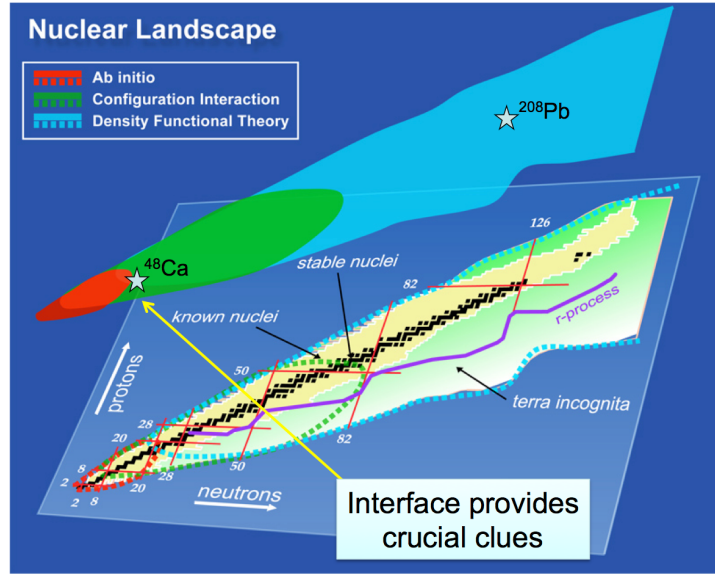


Figure 1.9: Nuclear Landscape

So we can get

$$\begin{aligned}
 M(E_0 - E') &= E_0 E' (1 - \cos \theta) \\
 E' &= \frac{M E_0}{M + E_0 (1 - \cos \theta)} \\
 Q^2 &= -q^2 = -[(E_0 - E')^2 - (\mathbf{p}_0 - \mathbf{p}')^2] \\
 &= 2E_0 E' (1 - \cos \theta)
 \end{aligned}$$

1.5 Why Pb and Ca

As tiny as the neutron skin thickness, to measure it relatively accurate, the larger it is, the better our measurement will be. So the target elements should have a large neutron excess. So ^{208}Pb (^{48}Ca) is chosen for PREX-II (CREX). Besides, both nuclei are spin-0, so that we don't need to worry about the target polarization. When the single nucleon separation energy in a nucleus is much larger than that of its neighbors, it is said that this nucleus has a magic number of protons or neutrons. The magic number arises from the nucleon shell structure – when a shell is fully filled and the next higher energy shell is empty, it is hard to separate out a nucleon from that closed shell. Both ^{48}Ca and ^{208}Pb are doubly magic nuclei, which means both the number of protons and neutrons are magic number, therefore a simple structure. It also means that the energy of their first excited state is much larger than the ground state, being 3.84 and 2.6 MeV respectively. Combined with the high momentum resolution of HRS, it provides sounding ground for flux integration detection.

As we see in previous section, the elastic scattering is quasi, not exact. The small energy change is caused by nuclei recoil. The heavier the target nuclei, the smaller the

recoil effect, the smaller the Q^2 , the better our measurement of Q^2 and scattering angle.

Finally, ^{48}Ca , which lies in the medium region of the nuclear landscape, is accessible from both ab-initio and DFT theoretical approaches. By measuring the neutron skin thickness of ^{48}Ca , we hope to provides a possibility to bridge these two methods.

Chapter 2

Experimental Setup

Over the past 30 years, PVES has been a well-established and powerful experimental technique in atomic, nuclear and particle physics. Its success traces back to Lee and Yang's prediction of parity violation in beta decay in 1956 [?] and the following experimental provement by Wu in 1957 [26]. Shortly later, Zel'dovich first predicted the existance of parity-violating weak neutral current and proposed to measure it in electron-proton scattering [27] in 1959. But it was only about 20 years later that people was able to experimentally observe the PV asymmetry in electron scattering experiments. In 1978, C.Y. Prescott etc. (E122 experiment at SLAC) measured the PV asymmetry in the inelastic scattering of longitunally polarized electrons from an unpolarized deuterium target [3]. With this successful demonstration, more effort was made to improve this experimental technique, which matured and boomed at the turn of the last century. Many experiments were conducted to probe the contribution of strange sea quarks to nucleons' EM FFs (SAMPLE, G0, HAPPEX and A4) and test the Electroweak sector of the SM at low energy (E158, PVDIS, Qweak). It was PREX-I that first proposed the application of PVES to probe the structure of nuclei, then followed by PREX-II and CREX. Future programs (Moller, SoLID and MESA experiments) will continue the development of PVES and push it to a higher precision.

Generally, PVES experiments requires 2 experimental conditions: polarized electron beam and fast flipping of beam polarization. Both requirements actually come to the same dependence: an intense source of polarized electrons and with quick response. The nature of being PV means measurement between different polarization states, while the **tiny** characteristic of PV asymmetry demands fast flipping of the polarization states. To measure such a tiny quantity, it is essential to control the experimental configurations as the same as possible between different beam helicities. One obvious and effective method to do the job is to fast flipping of beam helicity, the faster the helicity reversal, the smaller the possible change in beam conditions, target density and other apparatus, the smaller the introduced false asymmetry. This requirement makes PVES out of the capacity of storage ring accelerators. Though of the fast reversal of electron's helicity, much effort is needed to control the beam fluctuation, making it as small as possible. Possible systematic uncertainties in the source and accelerator will be controlled through the slow reversal

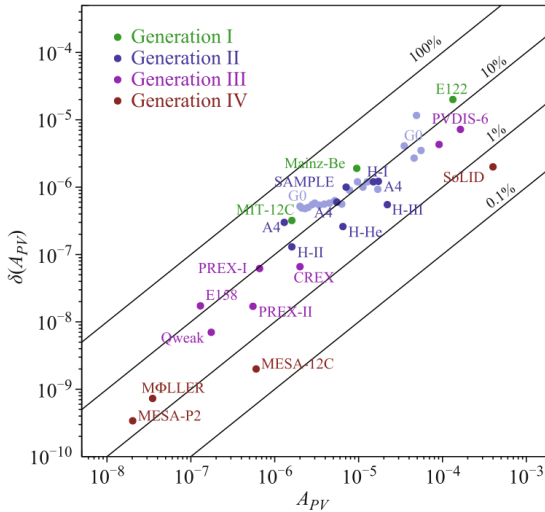


Figure 2.1: Evolution of PVES experiments, solid lines represent the relative precision. Generation I experiments (E122 (1978) [3], MIT-12C (1989) [4] and Mainz-Be (1990) [5]) did pioneering work to pave the way for PVES. Generation II experiments (the SAMPLE collaboration [6] at the MIT-Bates accelerator, the G0 [7] and HAPPEX [8] collaboration at Jefferson Lab and the A4 collaboration [9] at the Maizer Mikrotron (MAMI) accelerator) were devoted to the exploration of strange FFs in nucleons. Generation III experiments (E158 at SLAC [10], Qweak [11] and PVDIS [12]) tested the SM at low energy and measured the neutron skin thickness of nuclei (PREX-I/II and CREX). The planned Generation IV experiments (SoLID program [13] and MOLLER experiment [14] at JLab, P2 experiment on the future Mainz Energy-recovery Superconducting Accelerator (MESA) [15]) will continue to test the SM and explore the structure of nucleons with higher precisions. (MESA-12C is the same experiment as MESA-P2 with a different ^{12}C target)

of beam helicity. In terms of the target deformity under electron bombardment, a raster with very high scanning rate will minimize this uncertainty. As for detection of scattered electrons, electron flux rather than single electron will be counted due to high scattering rate in such experiments.

The 2 sister experiments were conducted in Hall A at JLab, the CEBAF accelerator at JLab is one of the few facilities in the world that can do PVES experiments (other facilities include MIMA and its successor MESA, the Facility for Antiproton and Ion Research (FAIR) and the Facility for Rare Isotope Beams (FRIB)). CEBAF provided excellent polarized electron beams (helicity correlated difference at sub-nanometer level) to hall A, with dedicated apparatus (Compton polarimeter, taget chamber, HRS and others) in Hall A, we were able to measure this tiny asymmetry precisely.

	PREX-II	CREX
Target	^{208}Pb	^{48}Ca
Target density (g/cm^3)	11.38	1.855
Target thickness (mm)	$0.2554 + 0.5520 + 0.2566$	6
Number of Target	10	1 + 1
Used	6	2
Beam Energy (GeV)	0.953	2.18
Largest Beam Current (μA)	70	150
Average Beam Polarization (%)	89.7	87.1
Beam Rate (MHz)	249.5	249.5
Electrons/Bunch ($\times 10^6$)	1.75	3.76
Helicity Flip Rate (Hz)	240	120
Power on Target ($Watt$)		
Scattering angle (deg)	4.7	4.51
Q^2 (GeV^2)	0.00616	0.0297
Scattering rate (MHz/arm)	$\sim 2200^{\textcolor{red}{1}}$	~ 28
xsection ($mbarn$)	3930.6	5.3
Acceptance (msr)	0.0037	0.0037
Collected Charge (C)	114	412
Predicted \mathcal{A}_{pv} (ppm)	0.6	2
Proposed precision	3.6%	2.4%
Error on R_n (fm)	0.06	0.02

Table 2.1: Summary of PREX-II and CREX

2.1 Kinematics

PREX-II and CREX are follow-up experiments to PREX-I, which also ran at JLab in 2010. With excellent control of systematic uncertainty, but unfortunately, many technical challenges during the experiment, PREX-I’s result was statistics limited, achieving a precision of 10% [?]:

$$\mathcal{A}_{Pb} = 656 \pm 60(stat) \pm 14(syst) \text{ ppb}$$

Based on the experience and lessons we learned from PREX-I, PREX-II and CREX had more well-established designs, which helped to meet the goal of high-precision.

One important feature of these 2 experiments is the redundancy design for critical components: we have 2 slow helicity reversal for systematic uncertainty control, we have 2 polarimeters for polarization measurement, we have multiple BPMs and BCMs for beam parameter monitoring, we have multiple Pb foil targets and finally 2 HRS arms for electron reception.

Experiment	PREX-II (%)	CREX (%)
Charge Normalization	0.1	0.1
Beam Asymmetry	1.1	0.3
Detector Non-Linearity	1.0	0.3
Transverse Asymmetry	0.2	0.1
Polarization	1.1	0.8
Target Contamination	0.4	0.2
Inelastic Scattering	< 0.1	0.2
Effective Q^2	0.4	0.8
Total Systematic	2	1.2
Statistical	3	2.4
Total	3.6	2.7

Table 2.2: Budget of systematic and statiscal error in both experiments [28, 29]

Uncertainty Budget

The goal of PREX-II is to achieve the 1% precision in ^{208}Pb neutron radius proposed by PREX-I, which requires the presicion of PV asymmetry measurement better than 3% [?]. CREX proposed similar goal, that a precision of 0.02 fm (0.6%) in the ^{48}Ca neutron radius will be an essential benchmark to test various microscopic models, which correspond to a 2.4% total error in PV asymmetry.

As said above, PREX-I already had impressive control over systematic uncertainties (2.1%), so will the PREX-II and CREX. The main concern is to collect as much scattered electrons as possible to reduce statistical error, which is inversely proportional to \sqrt{N} .

$$\frac{\delta \mathcal{A}}{\mathcal{A}} = \sqrt{\sigma_{stat}^2 + \sigma_{sys}^2} \quad \sigma_{stat} = \frac{\sigma_{det}}{P\sqrt{N}} \quad (2.1)$$

where:

- σ_{det} is the detector uncertainty
- P is the beam polarizaiton
- N is the total number of scattered electrons

2.1.1 Figure Of Merits (FOM)

The choice of beam energy and scattering angle is a compromise of competing factors. PV asymmetry prefers larger beam energy and larger scattering angle, while scattering rate falls dramatically with beam energy and scattering angle, Q^2 also likes smaller beam energy and scattering angle, and calculation showes that the sensitivity of PV asymmetry w.r.t. neutron radius is oscillating along beam energy. All these considerations are

incorporated into the FOM, which is defined as:

$$\text{FOM} = R \times \mathcal{A}^2 \times \epsilon^2$$

where R is the scattering rate, \mathcal{A} the PV asymmetry and ϵ the sensitivity of \mathcal{A} w.r.t. R_n . One difference here is that FOMs for most PVES experiments have only R and \mathcal{A}^2 , the inclusion of ϵ in our FOM help to achieve a higher precision in R_n measurement.

Rate

For a data set of N independent events sampled from one normal distribution $X \sim N(x_0, \sigma_0)$, the statistical uncertainty on the measured mean value will be:

$$\text{var}(\bar{x} = \frac{1}{n} \sum x_i) = \frac{1}{n^2} \text{var}(x_i) = \frac{\sigma_0^2}{n} \implies \sigma(\bar{x}) = \frac{\sigma_0}{\sqrt{n}}$$

Assume one want to measure a 1 *ppm* asymmetry to 1% statistical uncertainty,

$$\frac{\sigma_A}{A} = \frac{1}{A} \frac{\sigma_{\text{det}}}{\sqrt{2N}} \approx \frac{1}{A\sqrt{2N}} = 1\% \implies N = 5 \times 10^{15} \quad (2.2)$$

a factor of 2 is included because we have 2 HRS arms. One need to count $\sim 10^{15}$ scattered electrons. Given a counting rate of 1 *MHz*, it will take $\frac{5 \times 10^{15}}{1 \text{ MHz}} = 5 \times 10^9 \text{ s} \approx 160 \text{ years}$, a completely unacceptable time scale. So we have to turn to integrated flux technique for a higher scattering rate, which is:

$$\frac{dR(\theta)}{d\Omega} = \frac{d\sigma}{d\Omega} I t \frac{\rho}{A} \times N_A \quad (2.3)$$

- $\frac{d\sigma}{d\Omega}$ is the fractional cross section in cm^2/str ,
- I is the beam current in *electrons/s*
- t is the target thickness in *cm*
- ρ is the target density in g/cm^3
- A is the atomic number
- $N_A = 6.022 \times 10^{23}$ is the Avogadro's constant and conversion factors.

The differential cross section was numerically calculated by our theoretical friends with values of 3930.6 *mbarn* and 5.3 *mbarn* for ^{208}Pb and ^{48}Ca at their corresponding kinematics. Other parameters can be checked in table 2.1.

The total rate will be the integration over the acceptance:

$$R = \int \frac{dR(\theta)}{d\Omega} d\Omega = \frac{dR}{d\Omega} d\Omega \quad (2.4)$$

PREX-II and CREX have an acceptance defined by the septum and Q1 collimator, which is $d\Omega = 0.0037 \text{ str}$

Finally, we should also consider radiative correction due to emission of virtual and real soft photons (Bremsstrahlung), and hard photons by vacuum polarization, this correction is formulated as:

$$\eta = \left(\frac{\Delta}{E} \right)^{bt} \quad (2.5)$$

which is evaluated to be: $\eta \sim 0.5$.

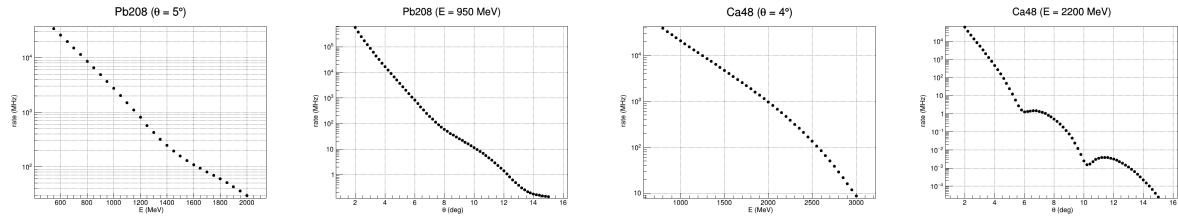


Figure 2.2: Scattering rate versus beam energy and scattering angle for ^{208}Pb and ^{48}Ca , the energy and scattering angle are design values. We see that rate falls quickly along both beam energy and scattering angle for both nuclei, so one would like small beam energy and small scattering angle (equivalently small \mathbf{q}) for large scattering rate.

Asymmetry and Sensitivity

As we shown in eq. 2.2, the asymmetry itself matters, a 2 times larger asymmetry means we can reduce the run time to one quarter, a huge save of beam time. So we should choose the kinematics region where asymmetry is large. Besides, asymmetry's sensitivity (ϵ) to neutron radius is also important, keep in mind that our final goal is to extract neutron radius from PV asymmetry, the more sensitive the asymmetry to neutron radius, the more precise the extracted neutron radius. The sensitivity is calculated as the relative change of \mathcal{A} with 1% change in neutron radius.

$$\epsilon = \frac{\delta \mathcal{A}/\mathcal{A}}{\delta R/R} = \frac{|\mathcal{A}_{stretched} - \mathcal{A}|/\mathcal{A}}{1\%} \quad (2.6)$$

Though asymmetry is what we want to measure, we can estimate its value based on some theoretical models, as was numerically calculated by our theoretical friends in [2].

Based on the theoretical result, we can optimize the kinematics for both nuclei:

$$\frac{\delta R}{R} = \frac{\delta \mathcal{A}}{\mathcal{A}} \frac{1}{\epsilon} = \frac{\sigma_{det}}{P} \frac{1}{\sqrt{N} \mathcal{A} \epsilon} \quad (2.7)$$

To minimize $\delta R/R$, it is equivalent to maximize

$$FOM = N \times \mathcal{A}^2 \times \epsilon^2 \quad (2.8)$$

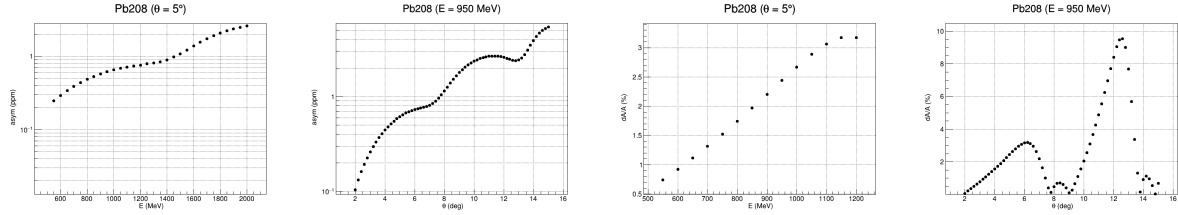


Figure 2.3: Asymmetry and sensitivity plot for ^{208}Pb , which increases along beam energy and oscillating up along scattering angle. The sensitivity plot is calculated with 1% change in neutron radius and it shows the absolute value. So in small scattering angle region, there is a local maximum around 6°

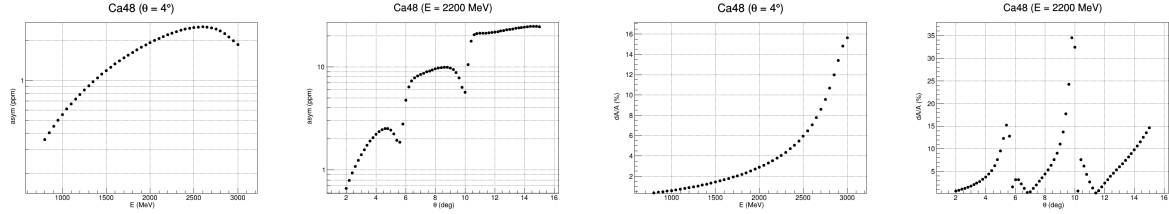


Figure 2.4: Asymmetry and sensitivity plot for ^{48}Ca , the asymmetry maximize around 2500 MeV and there is a local maximum about 4.5° . As for sensitivity, there is regional maximum around 5°

The design values of beam energy and scattering angle were chose to be 950 (2200) MeV and 5 (4) degree for ^{208}Pb (^{48}Ca). The beam energy of CREX is exactly 1-pass beam energy in CEBAF.

2.2 Continuous Electron Beam Accelerator Facility (CEBAF)

CEBAF is able to deliver multi-GeV continuous wave (cw) eletron beams of different energies and different intensities to 4 halls simultaneously. With the 12 GeV upgrade, the north and south 1497 MHz LINAC each has 25 Superconducting Radial Frequency (SRF)

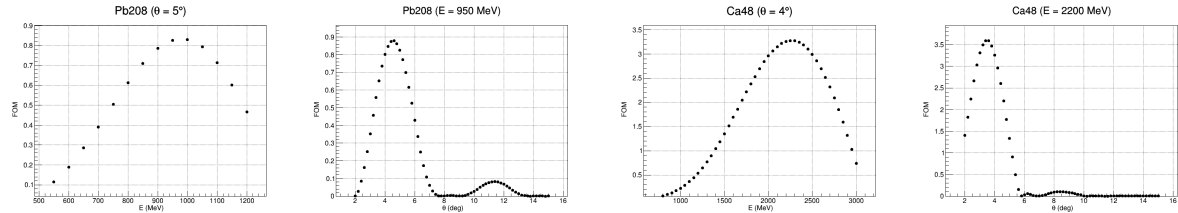


Figure 2.5: For both nuclei, FOM supports a small scattering angle. As for beam energy, FOM maximize around 950 (2200) GeV for ^{208}Pb (^{48}Ca).

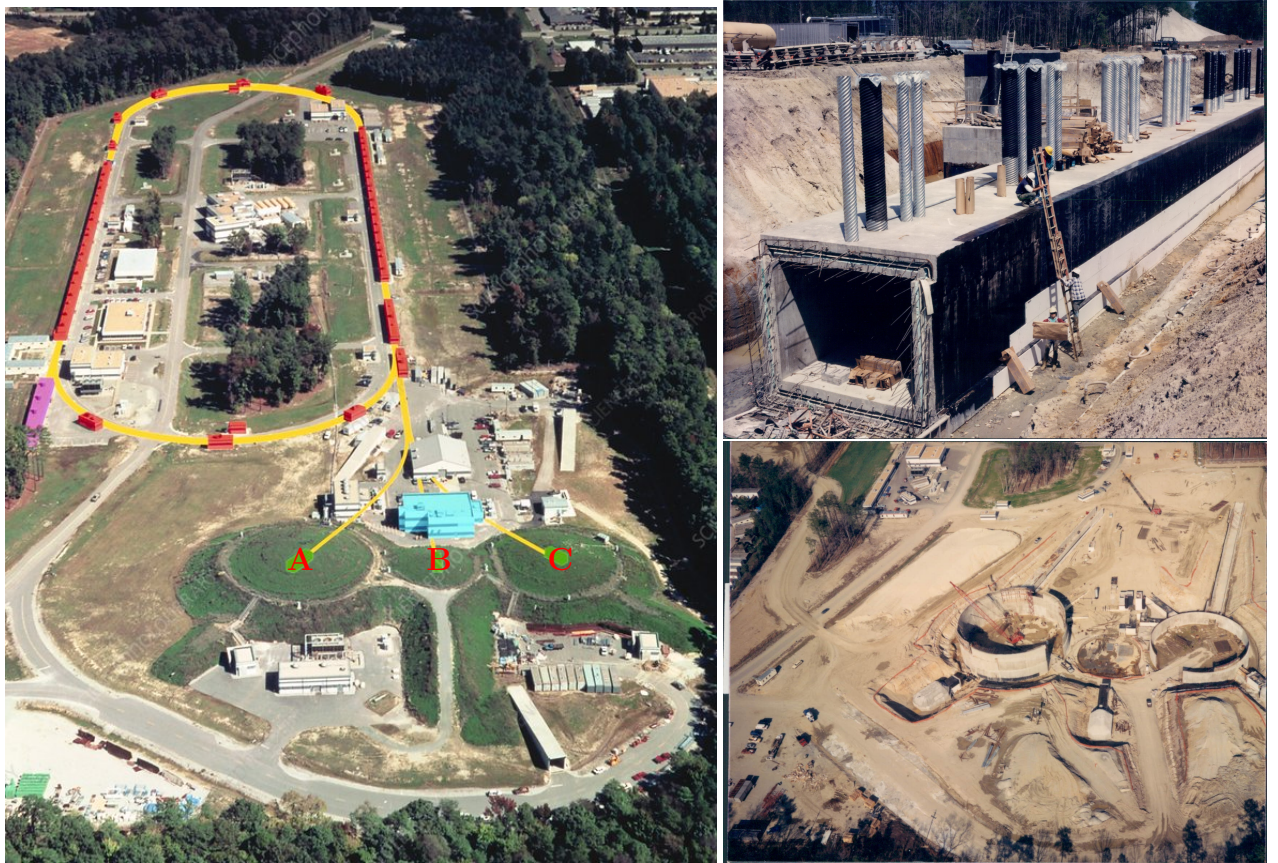


Figure 2.6: Aerial view of JLab accelerator site, yellow line tells the position of the CEBAF accelerator and the 3 experimental halls are marked out as A/B/C (Hall D locates on the top left corner, after the exit of north LINAC). The accelerator tunnel is 30 *feet* (~ 9 m) underground and 10 *feet* (~ 3 m) high, with a circumference of about 7/8 *miles* (1.4 km). There are 2 superconducting LINAC (red lines), each of 1/4 *miles* (400 m). The pink part on the mid left is the location of injector. The right 2 plots show the tunnel and experimental halls under construction.

cryomodules, capable of accelerating electrons at the peak rate of 2.2 *GeV/turn*. Hall A, B and C can receive up to $2.2 \times 5 = 11$ *GeV* cw beams and Hall D, with an extra half circle, can receive up to 12 *GeV* cw beams. With this design, different nuclear experiments can be carried out in different halls without interfering each other, theoretically.

As one can see in 2.7, laser pulse ($\lambda = 780$ nm) from 4 lasers (Hall D laser is not shown in the plot) shoot in the electron gun (2 electron guns in total) that operates at -130 kV to excite electrons, which interweaving with each other, forming a chain of electron bunches, with a phase difference of 120° from neaby bunches (Hall D doesn't have its own slit in the chopper, therefore it follows either Hall A or Hall C). This electron chain is sent into north LINAC by the injector, accelerated by both LINACs. After reaching desired energy, they will be kicked out at the exit of south LINAC and delivered to experimental halls (A, B and C) for various experiments.

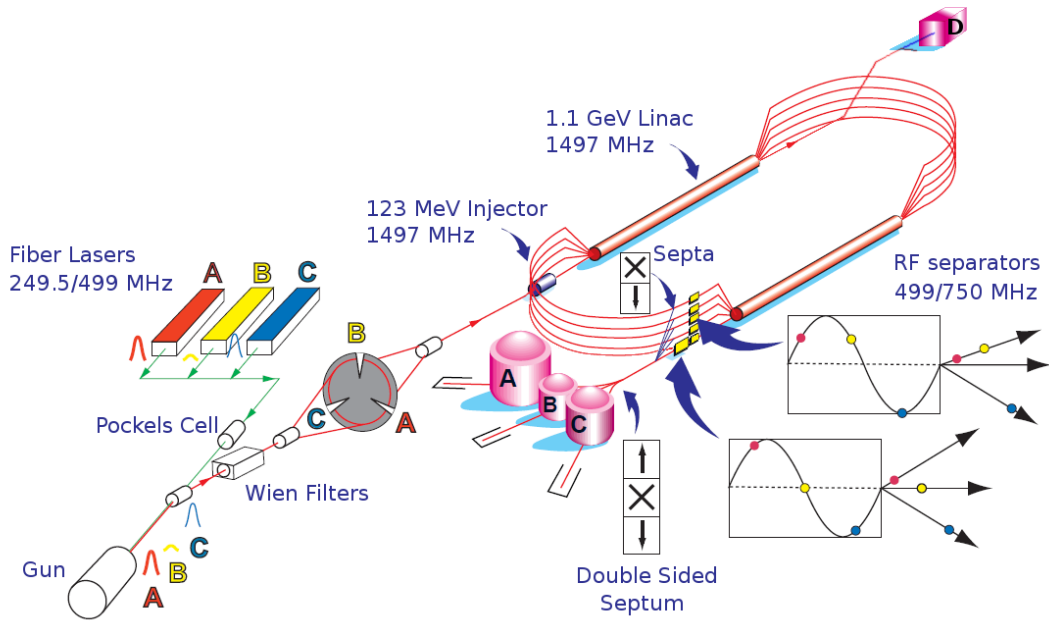


Figure 2.7: Schematic plot of CEBAF. Low energy beams will be kicked into higher arc, and high energy beams will go through lower arc. The magnetic field increases from higher arc to lower arc to keep electron trajectory have the same radius.

The maximum beam current of $200 \mu A$ at (old) highest energy of $5 GeV$ available at CEBAF is limited by the rf power ($1 MW = 5 GeV \times 200 \mu A$) and by the beam power on the beam dump. While Hall B and D requires only tiny amount of cw beams (at nA level), it is actually Hall A and C that consume the produced electron beams, both can receive a few tenths to over one hundred μA .

While all 4 halls at JLab are dedicated to the study of nuclear structure, they focus on different aspects. Hall A concentrates on form factors of various nuclei, Hall B digs into generalized parton distributions, Hall C devotes itself to precise determination of valance quark properties in nuclei, and finally, the newly established Hall D explores origin of confinement through exotic mesons.

Because all 4 halls shared the same electron source and the same accelerator, cooperation is needed to make them work at the same time. In terms of electron source, PVES experiment usually has priority over other experiments to maintain the quality of polarized electron beam. As for the LINAC, if one hall wants a smaller energy, say $1 GeV$, then the LINAC power will be reduced to $1 GeV/turn$, which will be applied to other halls' electron beams, therefore limiting the highest energy available in other halls. Careful schedule is needed to make sure every hall get what they want.

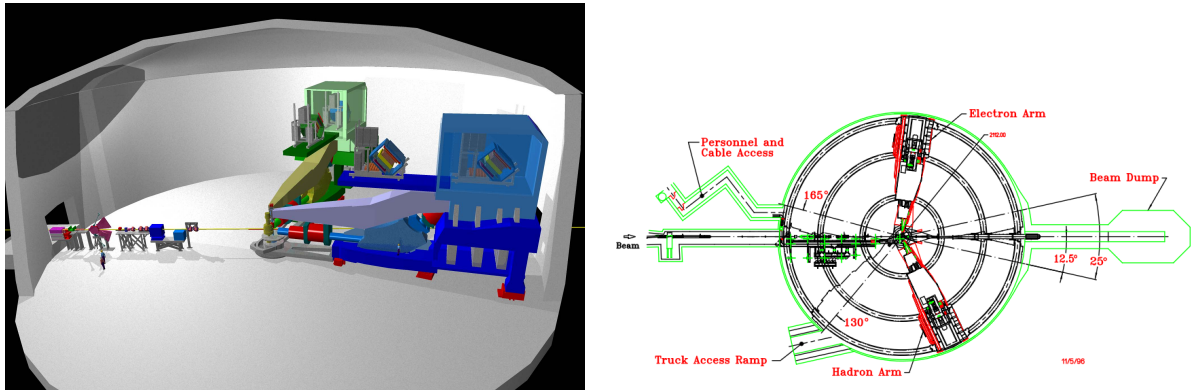


Figure 2.8: 3D and bird view of Hall A [?]. Originally, they were called High Resolution Hadron Spectrometer (HRHS) and High Resolution Electron Spectrometer (HRES), but they are essentially identical to each other and can be used interchangeably. so now they are called left arm (HRS-L) and right arm HRS (HRS-R).

2.3 Polarized Electron

2.3.1 Polarized Electron Source

PVES experiments motivate the development of polarized electron source, which require a highly stable polarized electron source that can produce high polarization electron beam at a wide range of intensity, from nA to A depending on the experiment. The source should be capable of rapid helicity reversal ($\sim 100Hz$) with negligible impact on other properties of the beam.

Currently, GaAs-based semiconductor photoemission source is the only available polarized electron source for accelerators on the market. Historically, this kind of electron source was the only one that could satisfy high peak currents required by the low duty factors of the old accelerators and rapid helicity reversal required by PVES. That's why it is the only player on the market now. Over the past few decades, pulsed beam has been replaced by continuous beam while this electron source is inherited and further developed. The polarized electron source used by CEBAF can produce electron beam with polarization greater than 85%, much larger than the 37% polarization from its inauguration at SLAC. [3]

The design was first proposed independently by Garwin, Pierce and Siegmann [30] and by Lampel and Weisbuch [31]. The idea is straightforward: When circularly polarized laser light with carefully selected energy $E_{gap} < h\nu < E_{gap} + \Delta$ shoot on the semiconductor, only electrons on the valance band $P_{3/2}$ will be pumped into the conduction band $S_{1/2}$. The selection rule makes sure only those transitions that satisfy $\Delta m_j = +1$ (-1) can occur for circularly right (left) incoming photons, As shown in fig. ???. The ratio of the transition rate is also marked out in circle in the plot, which can be calculated from the Clebsch-Gordan coefficient easily. The excited electrons are polarized and different states have different pumping rate, so we have polarized electron beam now with

polarization as: $P = (3-1)/(3+1) = 50\%$, for both cases.

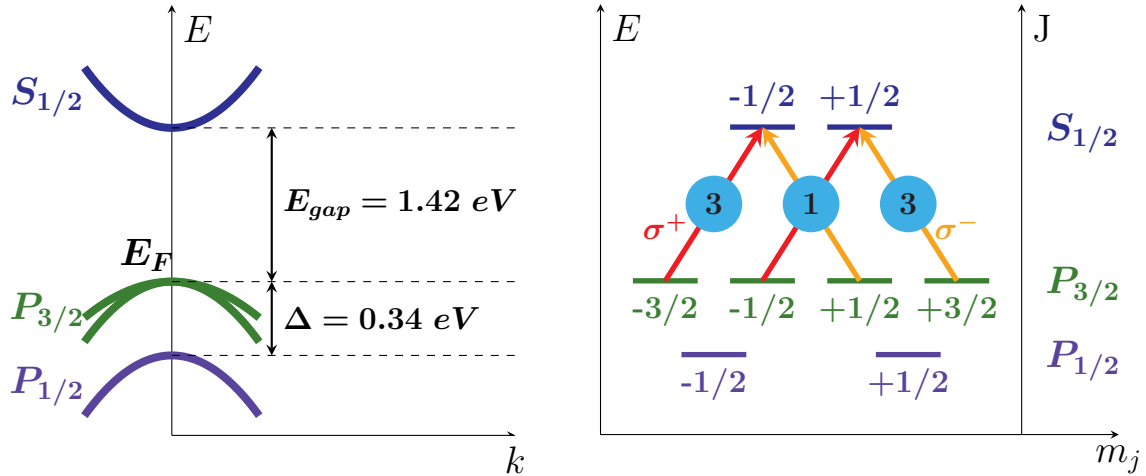


Figure 2.9: Excitation of polarized electrons

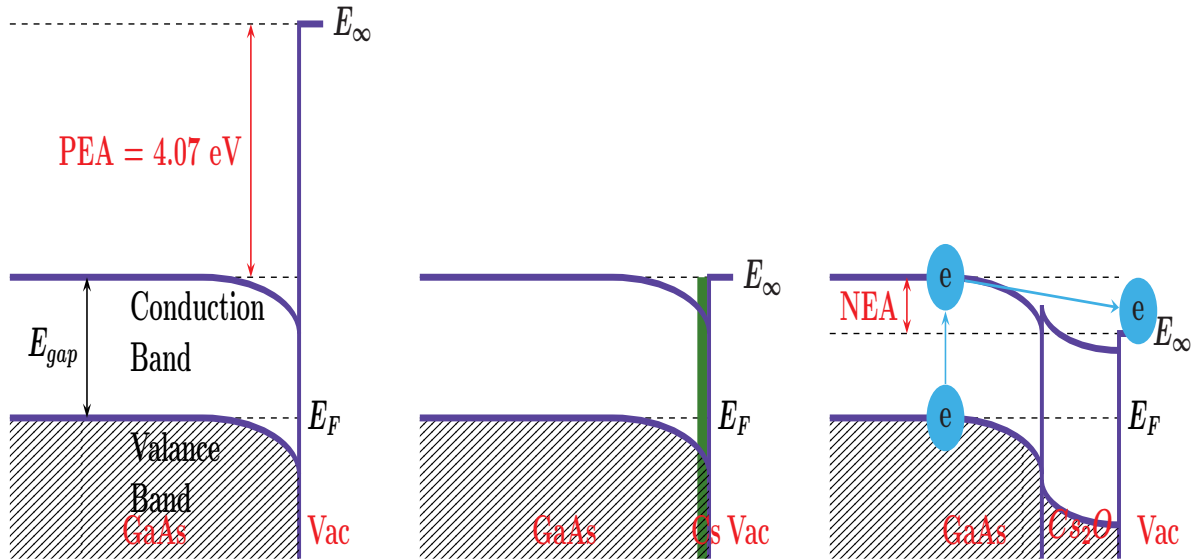


Figure 2.10: The energy band diagram of GaAs near its surface. Left: bare p-type GaAs, the large positive electron affinity (PEA) prevents electrons from escaping the surface; Middle: p-type GaAs with a cesiated surface, the electron affinity (EA) is 0, but electrons still can't escape the surface easily; Right: GaAs with layer of cesium oxide; the electron vacuum energy E_∞ is lowered to make a negative EA so that electrons can break free the surface easily. [16]

Then how can we liberate the polarized electrons from the material, without degenerating the polarization significantly. As shown in fig. ??, for bare GaAs, a 4.07eV electron affinity (EA) prevents any electrons from leaving the surface. To solve this problem, a

condition known as negative electron affinity (NEA) is used, that is to make the energy of electron in the vacuum just outside the surface lower than the conduction band energy by adding a layer a cesium oxide on the surface of pure GaAs semiconductor.

By the NEA technique, we were able to get polarized electron beam, but never reached the ideal 50% polarization, achieved polarization range between 25 to 43%. The polarization loss is due to spin dilution as electrons diffuse to the semiconductor surface. From this aspect, we can increase the polarization by reducing the thickness of the GaAs crystal. But obviously, even the thinnest GaAs crystal can't give us a polarization greater than 50%. New strategies are needed. It turned out the answer was strained GaAs. [16]

With a strained layer, the degeneracy of $P_{3/2}$ state is splitted, only states with $m_j = \pm 3/2$ will be pumped, therefore we will get 100% polarization, in ideal case. The real polarization achieved by CEBAF electron source is about 88%.

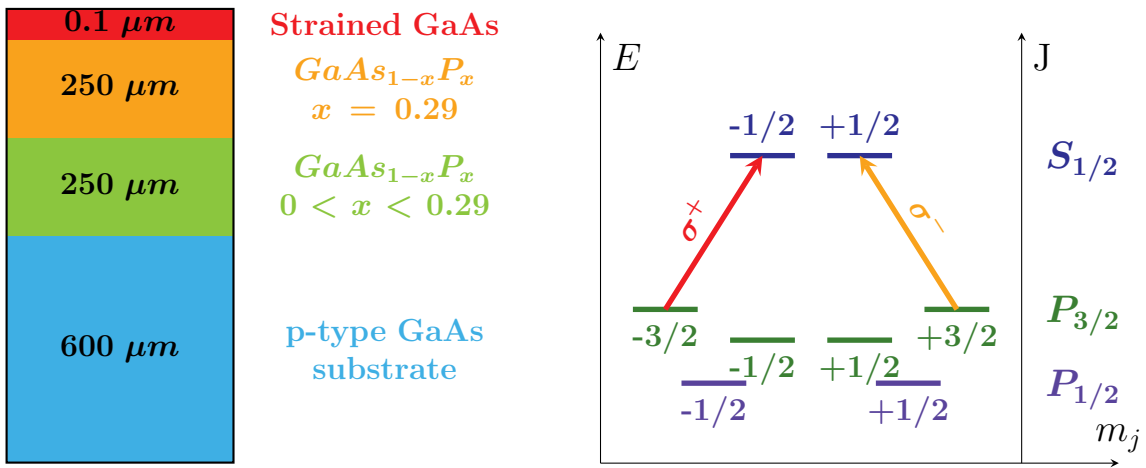


Figure 2.11: Strained GaAs

2.3.2 Polarization Control

Pockels Cell

Now that we can produce polarized electron beams, we need more control over the polarization of the electron beams. We should be able to flip the beam polarization quickly while keeping polarization as stable as possible. It is not easy and time consuming to manipulate the electron directly, while manipulating photons is much easier. One just need to reverse the circular polarization of the laser pulse, it will flip the electron beam polarization. The easiest way to do the job is a half-wave plane, by inserting it into or retracting it from the laser path, the phase of the laser pulse will be changed by π , flipping the laser circular polarization. But mechanical movement is not fast enough, the fast flipping of beam polarization is done by a component called Pockels Cell (PC), which is Rubidium Titanyle Phosphate (RTP) crystal. PC operates based on the Pockels effect, which is the production of birefringence in the crystal under an electric field, the

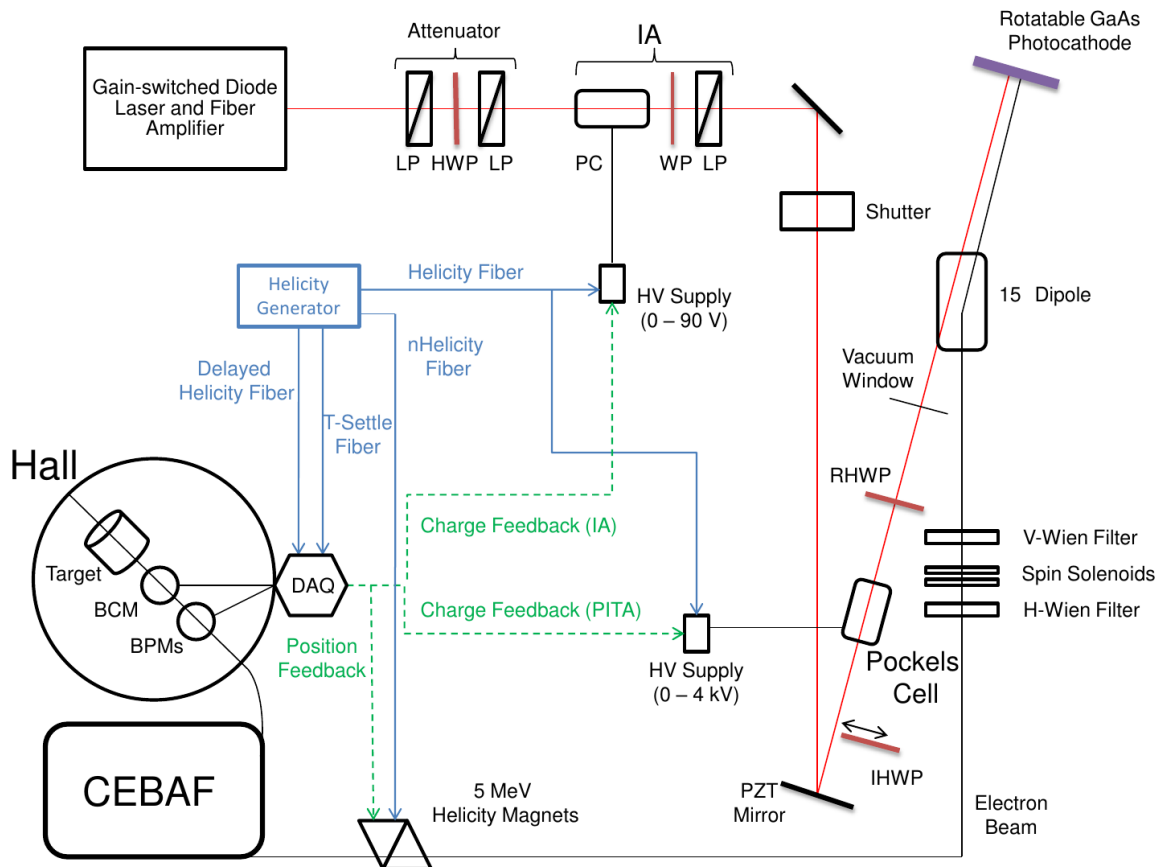


Figure 2.12: The laser system at the CEBAF injector

birefringence is proportional to the strength of the applied electric field. By applying appropriate high voltage (~ 1.5 kV), PC will act as a quarter wave plate (photon amplitude along fast and low axes E_x, E_y will have a phase difference of $\pm\frac{\pi}{2}$ depending on the polarity of the applied electric field), converting linearly polarized laser beam into circularly polarized laser beam. And reverse the electric field polarity will reverse the polarization of the laser beam. This transition can be very fast, up to 1 kHz, with a dead time of about 60 μ s.

Polarization Induced Transport Asymmetry (PITA, or Phase Induced Transmission Asymmetry) [?]

What we talked about above is the ideal case that PC will be an exact quarter wave plate and other optical components also work well, in reality, there is always deviation from the perfect circular polarization, resulting in systematic effect on beam position, spot size and intensity. If the deviation is polarization correlated, it will introduce a false asymmetry to our PV asymmetry measurement, which is called the PITA effect. The PITA effect is the dominant piece of HCBA, which, as we said before, is the largest false

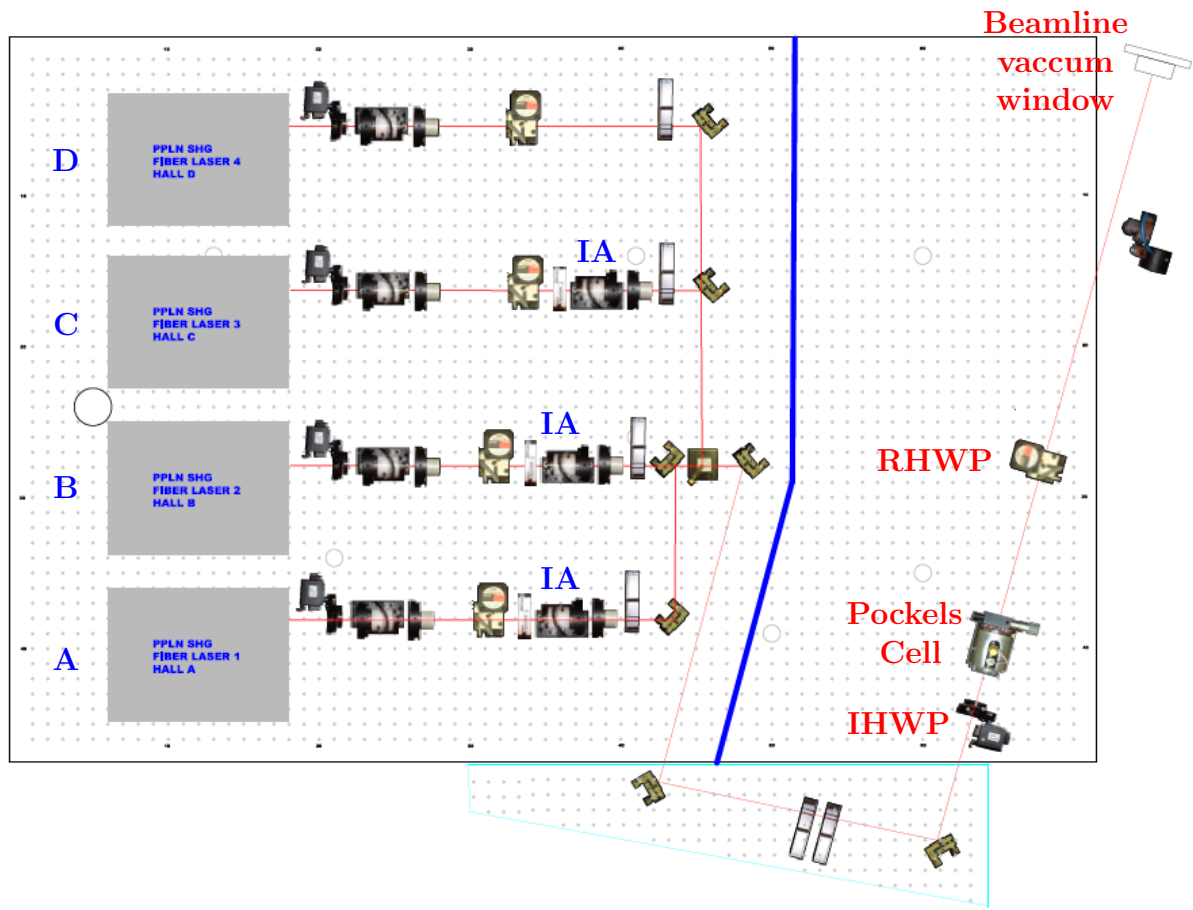


Figure 2.13: How the laser table actually looks like

asymmetry in our measurement.

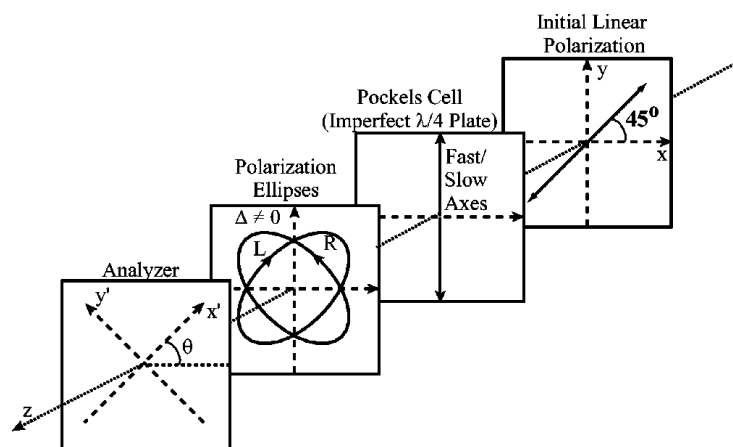


Figure 2.14: Phase shift by going through the PC

The PITA effect is characterized by the PC induced phase shift δ

$$\delta^{R(L)} = \mp \left(\frac{\pi}{2} + \alpha \right) - \Delta$$

where α and Δ represent the symmetric and asymmetric offset phase shift respectively. The resultant slightly elliptical beam has a residual linear component, leading to an intensity asymmetry (to first order):

$$\mathcal{A}_I = \frac{I^R - I^L}{I^R + I^L} = -\frac{\epsilon}{T} [\Delta \cos(2\theta)] \quad (2.9)$$

ϵ/T ($<< 1$) defines the “analyzing power”, $\epsilon = T_{x'} - T_{y'}$ and $T = (T_{x'} + T_{y'})/2$, $T_{x'(y')}$ is the transmission coefficient along the axis x' (y') of the downstream analyzer. θ is the angle between the PC’s fast axis and the x' axis of the analyzer

Consider other optical elements along the laser path, like the RHP and the vacuum window, the unknown tiny birefringence in these components will also contribute to Δ , resulting to a modified intensity asymmetry:

$$\mathcal{A}_I = \frac{I^R - I^L}{I^R + I^L} = -\frac{\epsilon}{T} [\cos(2\theta) \cdot (\Delta - \Delta^0)] \quad (2.10)$$

To minimize the intensity asymmetry, one would like to keep $\Delta - \Delta^0$ as small as possible. Fortunately, *Delta* is tunable, by change the applied electric field. As shown in fig. 2.12, our charge feedback system will monitor the charge intensity asymmetry and automatically adjust the HV supplied to the PC to maintain a small \mathcal{A}_I . Over CREX, the average charge intensity asymmetry is ??? ppm.

As you may see in fig. 2.12, the charge feedback system also controls the HV supply of the Intensity Attenuator (IA), which, together with the slit in beam chopper, controls the intensity of electron beams. So, IA also plays a key role in achieving a small charge intensity asymmetry by equalizing beam intensity across helicity states.

A optical element called Rotatable Half-Wave Plate (RHWP) lies downstream the PC, it help to equalize any residual linear polarization left in the PC to establish a Quantum Efficiency (QE) independence of helicity.

Slow Helicity Reversal

Fast reversal of the PC can minimize a lot of random noise from beam and target density fluctuations, nevertheless, some helicity correlated (HC) false asymmetries remain, such as electronic pickup between accelerator electronic systems and the experimental DAQ system or the residual birefringence effect. It is the job of slow helicity reversal to cancel these systematic false asymmetries.

There are 2 methods to make slow helicity reversal – the Insertable Half-Wave Plate (IHWP) and the double Wien Filters. Prior to 2009, IHWP was the only available approach at CEBAF to do slow helicity reversal. A new mechanism was introduced

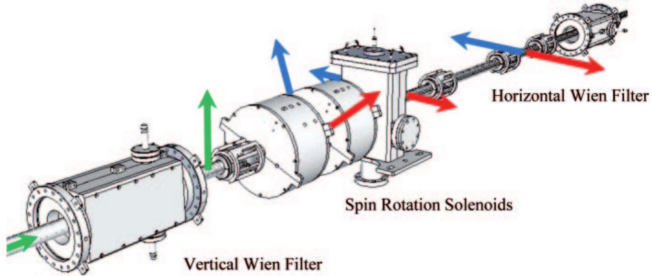


Figure 2.15: Schematic plot of double wien filter, electron beam travels from left to right. [17]

during PREX-I and Qweak experiments for better systematic precision – the wien filter.

The IHWP lies upstream of the PC, it is the easiest way to reverse the beam helicity by inserting or retracting the IHWP. With slow helicity reversal, we can identify the possible systematic uncertainties. The idea is simple, assume the true and a systematic false asymmetry to be A_0 and ΔA , then what we measure by inserting (retracting) the IHWP will be:

$$A^{+(-)} = \pm A_0 + \Delta A \quad (2.11)$$

Because IHWP doesn't affect the systematic uncertainty, so the true asymmetry will be:

$$A_0 = \frac{A^+ - A^-}{2} \quad (2.12)$$

As easy and good as IHWP, it resolves only some of the HC beam variations, namely the residual birefringence from the laser optical system and is powerless in dealing with other HC effects, like HC beam size variations that are introduced via PC focusing [17], which is addressed by the wien filter. The wien filter manipulate the electron spin directly by electromagnetic field without affecting the electron movement and is able to achieve any spin orientation. It consists of 2 wien filters and 2 intervening solenoids between them. A wien filter is such a cavity with proper electric and magnetic field ($qE = qvB$), perpendicular to each other and to the electron moving direction, so that it rotates electron spin only. Electrons coming from the photocathode are longitudinally polarized, the vertical wien filter will make the electron spin vertical oriented, so that it can be rotated to left/right by the following spin solenoid, depending on the polarity of the solenoid, a wien flip means to change the polarity of the spin solenoid. Finally, the horizontal wien filter will fine tune the spin direction to optimize the longitudinal polarization in the experimental hall. Note that electrons exit the double wien filters are not longitudinally polarized, because electron spin will precess when travel through the accelerator, causing a rotation in the horizontal plane. Therefore, a carefully selected initial spin direction is needed to make sure the spin is (anti) parallel to electron momentum at target.

This tells us another function of the wien filter, to set a non-longitudinal initial spin to cancel out the shift caused by spin precession during acceleration, so that we have

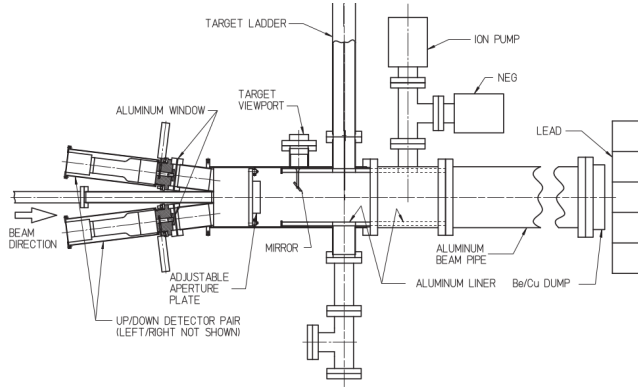


Figure 2.16: Schematic plot of the Mott polarimeter, it has 4 symmetric detector ports (up and down, left and right – which is not shown in the plot). The back scattering angle is 172.6° , where we have the highest analyzing power from theoretical calculation of the Sherman function. [33]

exactly longitudinally polarized electron beam at target.

With both IHWP and Wien filter, we are able to cancel most systematic false asymmetries, achieving very small systematic errors.

2.3.3 Polarimeters

Now that we have polarized electron beams, we still need to measure its polarization. We have 3 polarimeters to measure the beam polarization: the Mott polarimeter at injector and the Compton and Moller polarimeter in Hall A. As their names imply, they use the cross section asymmetry of the Mott, Compton and Moller scattering to measure the polarization of the electron beam. Since these are all pure QED processes, their cross sections are well understood and analyzing powers are easily calculable to high order.

While both Mott and Moller measurement are invasive, they can't be done frequently (Moller measurement happens about every 10 days). the non-invasive Compton polarimeter is the only choice for beam polarization monitoring. Mott polarimeter measures the beam polarization before it enters the accelerator, so it is not used for the determination of beam polarization during PREX-II/CREX.

Mott Polarimeter

The 5-MeV Mott polarimeter lies at the CEBAF injector, between the Wien Filter and the Injection Chicane, it measures the single spin cross section asymmetry of 5 MeV electron beams scattered off a high-Z target. Comparing the measurement to the Sherman Function [32], the analyzing power, will tell us the transverse polarization of the electron beam:

$$\mathcal{A}_{LR} = \frac{N_L - N_R}{N_L + N_R} = S(\theta) \mathbf{P} \cdot \hat{\mathbf{n}} \quad (2.13)$$

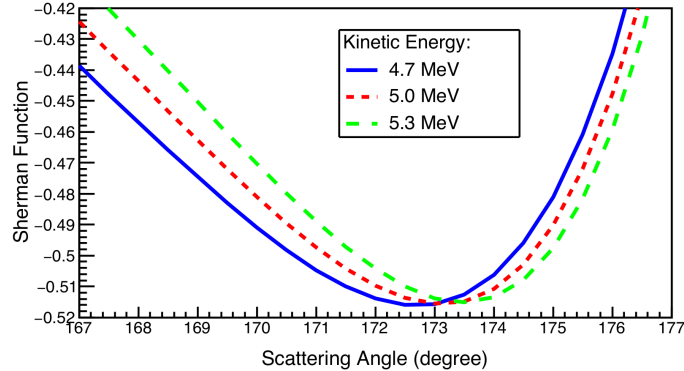


Figure 2.17: The Sherman Function for different high-Z targets at 5 MeV, dots represent experimental measurement.

$\hat{\mathbf{n}}$ is the unit normal vector of the scattering plane. The same formula applies to the Up-Down asymmetry. Because the asymmetry comes from the coupling of electron's spin and the induced magnetic field by the nucleus in the electron's rest frame (spin-orbit coupling), the scattering potential is:

$$V(r, \mathbf{L}, \mathbf{S}) = V_{Coulomb} + V_{so}(r, \mathbf{L}, \mathbf{S}) = \frac{Ze}{r} + \frac{Ze^2}{2m^2r^3} \mathbf{L} \cdot \mathbf{S} \quad (2.14)$$

So only transverse polarization can be measured using Mott polarimeter, rather than the longitudinal one we desire at the target. Nevertheless, it provides an independent check of the initial beam polarization from the injector and its high precision (its total uncertainty can be as small as 0.61% [33]) helps to normalize the polarization measurement in the experimental halls.

Compton Polarimeter

The Compton polarimeter locates at the entrance to hall A (about 20 m upstream the target chamber), using the elastic scatter between polarized photon and electron to measured the polarization of the electron beam. As shown in fig 2.18, when the compton polarimeter is on, the electron beam will be bent into the Compton Chicane to interact with the polarized photons nearly head-on (a tiny crossing angle of 23.5 mrad). The Fabry-Perot Cavity is locked to and filled with circularly polarized (> 99%) green laser beam ($\lambda = 532 \text{ nm}$, $E = 2.334 \text{ eV}$). The back-scattered photons will be detected by a GSO (low energy) or PbWO₄ crystal calorimeter right of the interaction region, while the electron beam will be bent back to the beam pipe to bombar the target. Due to interaction with photons, the scattered electrons will be less energetic than the incoming ones. So under the same dipole field, the scattered electrons will be bent more than the non-interacting electrons, as shown by the red dash line in Fig. 2.18. This seperation allow us to measure the scattered electrons, together with measurement of scattered photons, we can identify and scattering asymmetry and then the polarization of the electron beam.

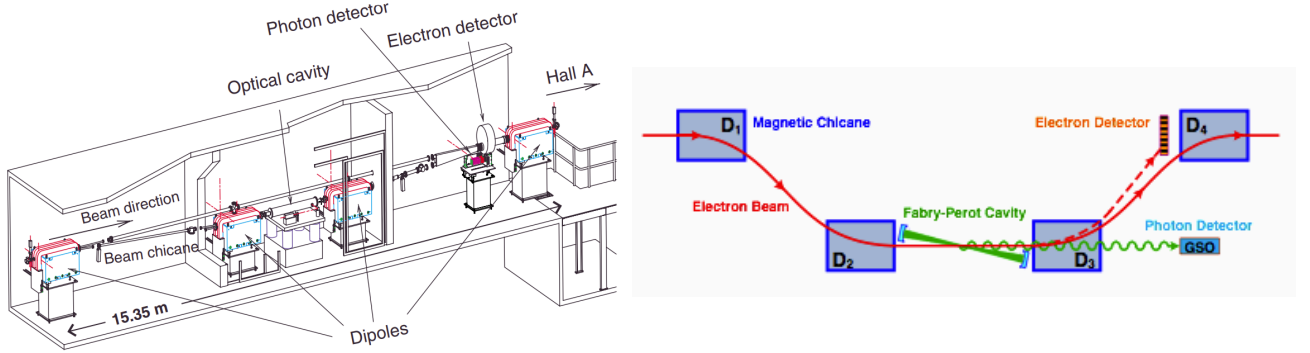


Figure 2.18: Left: Compton Chicane [?]; Right: Schematic plot of electron/photon scattering

The energy of the scattered photon will be:

$$E_\gamma \approx E_{laser} \frac{4a\gamma^2}{1 + a\theta_\gamma^2\gamma^2} \quad (2.15)$$

where $\gamma = E_{beam}/m_e$ is the Lorentz factor of the incoming electron, $a = \frac{1}{1+4\gamma E_{laser}/m_e}$ and θ_γ is the scattering angle w.r.t. the electron moving direction. The maximum energy of the scattered photon appears at $\theta_\gamma = 0$, which is back scattering. For PREX-II (CREX) beam energy of 0.95 (2.2) GeV , $E_\gamma^{max} \sim 32.55$ (167.02) MeV .

Define $\rho = \frac{E_\gamma}{E_\gamma^{max}}$, the cross section for unpolarized Compton scattering will be:

$$\frac{d\sigma}{d\rho} = 2\pi r_0^2 a \left[\frac{\rho^2(1-a)^2}{1-\rho(1-a)} + 1 + \left(\frac{1-\rho(1+a)}{1-\rho(1-a)} \right)^2 \right] \quad (2.16)$$

$r_0 = \frac{\alpha\hbar c}{mc^2}$ is the classical electron radius; then the analyzing power will be:

$$\mathcal{A}_l = \frac{\sigma_{\Rightarrow}^{\rightarrow} - \sigma_{\Rightarrow}^{\leftarrow}}{\sigma_{\Rightarrow}^{\rightarrow} + \sigma_{\Rightarrow}^{\leftarrow}} = \frac{2\pi r_0^2 a}{d\sigma/d\rho} (1 - \rho(1+a)) \left[1 - \frac{1}{(1-\rho(1-a))^2} \right] \quad (2.17)$$

The measured asymmetry will be:

$$\mathcal{A}_{exp} = \mathcal{P}_e \mathcal{P}_\gamma \mathcal{A}_l = \frac{N_\gamma^R - N_\gamma^L}{N_\gamma^R + N_\gamma^L} \Rightarrow \mathcal{P}_e = \frac{\mathcal{A}_{exp}}{\mathcal{P}_\gamma \mathcal{A}_l}$$

The advantage of the Compton polarimeter is that it can tolerate quite high current (up to $\sim 200 \mu A$ at JLab), plus its non-invasive operation make it a beam polarization monitor. The disadvantage is, comparing to Mott or Moller polarimeter, its analyzing power is quite low at GeV energy level, while increase the beam energy will lead to high

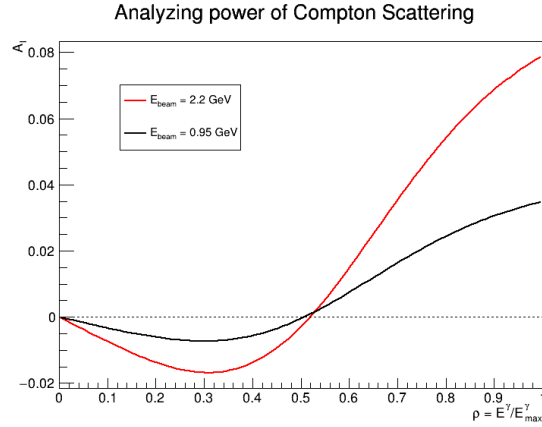


Figure 2.19: The Compton analyzing power increases with electron energy. Note that the analyzing power will change sign at $\rho \sim 0.5$ for both PREX-II and CREX beam energies.

background in the photon detection due to synchrotron radiation. Overall, the Compton polarimeter is able to achieve a 1% absolute systematic uncertainty.

Moller Polarimeter

The Moller polarimeter lies downstream of the Compton polarimeter and upstream of the target chamber. It uses elastic electron-electron scattering to measure the asymmetry due to different beam polarizations.

$$\begin{aligned} \frac{d\sigma}{d\Omega} &= \frac{d\sigma_0}{d\Omega} \left(1 + \sum_{i,j=x,y,z} \mathcal{P}_b^i \cdot \mathcal{P}_t^j \cdot A_{ij}(\theta_{CM}) \right) \\ \frac{d\sigma_0}{d\Omega} &= \frac{\alpha^2}{s} \left(\frac{4 - \sin^2 \theta_{CM}}{\sin^2 \theta_{CM}} \right)^2 \end{aligned} \quad (2.18)$$

With $\frac{d\sigma}{d\Omega} d\Omega$ being the unpolarized moller scattering cross section, s is the Mandelstam variable: $s = 2m_e(E + m_e) \approx 2m_e^2\gamma$, \mathcal{P}_b (\mathcal{P}_t) the polarization of beam (target). θ_{CM} and A_{ij} the scattering angle and analyzing power in CoM frame.

Assuming incoming electrons move in the z direction and the scattering happens in the xz plane, then in the ultra-relativistic limit:

$$\begin{aligned} A_{zz} &= \frac{\sin^2 \theta_{CM} (7 + \cos^2 \theta_{CM})}{(3 + \cos^2 \theta_{CM})^2}, & A_{xx} = -A_{yy} &= \frac{\sin^4 \theta_{CM}}{(3 + \cos^2 \theta_{CM})^2} \\ A_{xz} = A_{zx} &= \frac{2 \sin^4 \theta_{CM} \cos \theta_{CM}}{\gamma (3 + \cos^2 \theta_{CM})^2}, & A_{xy} = A_{yz} = A_{yz} = A_{zy} &= 0 \end{aligned} \quad (2.19)$$

When $\theta_{CM} = 90^\circ$, A_{zz} is maximized to be $\frac{7}{9}$. This is what we choose in the moller polarimeter.

The polarized target electrons come from magnetized Fe-alloy foil, which is saturated

by a very strong (4 T) longitudinal magnetic field created by superconducting Helmholtz coils, as shown in Fig. 2.20. So Eq. 2.18 is simplified to:

$$\frac{d\sigma}{d\Omega} = \frac{d\sigma_0}{d\Omega} (1 + \mathcal{P}_b^z \cdot \mathcal{P}_t^z \cdot A_{zz}(\theta_{CM})) \quad (2.20)$$

The moller pair (the scattered incident electrons and recoil target electron) centered around $\theta_{CM} = 90^\circ$ ($\theta_{lab} < 3^\circ$), are seperated from the undeflected beam by set of magnets, then goes through collimators (at the exit of dipole, not shown in Fig. 2.20) that define the acceptance, and finnally is detected by electron detectors in coincidence. The measreud asymmetry between spin-parallel and anti-parallel cross section is:

$$A_{exp} = \frac{N^+ - N^-}{N^+ + N^-} = \mathcal{P}_b \mathcal{P}_t \langle A_{zz} \rangle \Rightarrow \mathcal{P}_b = \frac{A_{exp}}{\mathcal{P}_t \langle A_{zz} \rangle} \quad (2.21)$$

with $\langle A_{zz} \rangle$ being the average analyzing power over the acceptance, which was about 0.75 for PREX-II and CREX.

The target foil was cooled by conduction through the target, whose temperature will climb quickly with increase beam current, causing damage to target polarization. Therefore moller polarimeter can only operate at very low current ($\lesssim 1\mu A$). The extrapolation from polarization measurement at low current to high current where PREX-II and CREX run at, is a large source of systematic uncertainty. During PREX-II and CREX, the target polarization was measured to be $\mathcal{P}_t \sim 8\%$ leading to an effective analyzing power of $A_{eff} = \mathcal{P}_t \langle A_{zz} \rangle = 6\%$. This relative large analyzing power makes moller measurement quite precise. Overall, Moller polarimeter in Hall A can achieve a systematic uncertainty less than 1%.

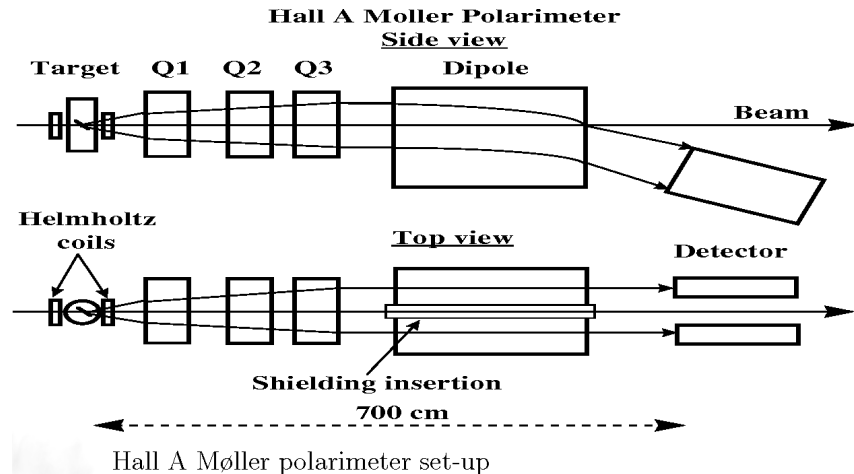


Figure 2.20: Møller Polarimeter

2.4 Monitors

Besides beam polarization, another significant source of systematic uncertainty is the beam false asymmetry – the difference in beam position, angle, energy and current between different helicity states. Because there is no way to ensure exactly the same beam parameters between different helicity states, even with fast helicity flipping. We monitored these variables with redundant specialised devices – Beam Position Monitors (BPMs) and Beam Current Monitors (BCMs). For PREX-II and CREX, we had another independent monitor system – Small Angle Monitors (SAMs). These monitors were able to measure the beam difference as precise as:

$$\Delta x \sim 1 \mu\text{m} \quad \Delta x' \sim 1 \text{ mrad} \quad \Delta p/p \sim 0.0004 \quad \Delta I/I \sim 100 \text{ ppm}$$

(FIXME)

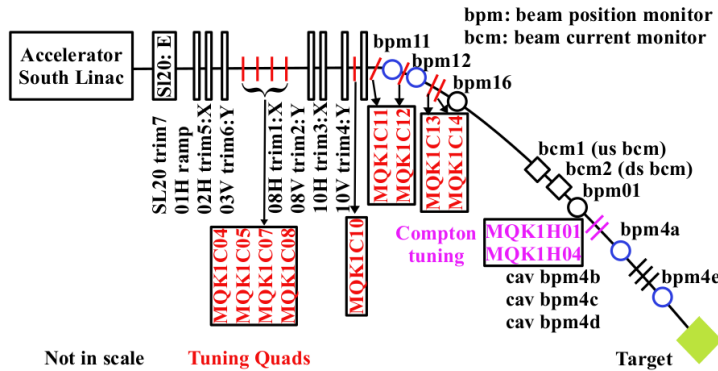


Figure 2.21: Schematic plot of Hall A beam monitor system and beam modulation system

2.4.1 BPMs

Hall A has a series of BPMs along the beam pipe leading to the target chamber to monitor the beam conditions, among them, 6 switched electrode electronics (SEE) stripline BPMs are important to PREX-II and CREX, their records are used to extract beam parameters. These 6 key BPMs are shown in Fig. 2.21. BPM4A and BPM4E locate 7.524 m and 1.286 m upstream of the target chamber, they are used to determine the beam position and angle on the target. BPM11 and BPM12 are positioned on the arc area to measure the beam energy using the bending radius of the electron trajectory. BPM1 and BPM16 are backup monitors.

A stripline BPM consists of a 4-wire antenna array of open ended thin wire striplines, the voltage induced by the electron bunches in each electrode is sensitive to beam position. Therefore we can extract (x', y') positions from opposite 2 pickup signals.

$$x' = \frac{1}{S_x} \frac{X_p - X_m}{X_p + X_m} y' = \frac{1}{S_y} \frac{Y_p - Y_m}{Y_p + Y_m} \quad (2.22)$$

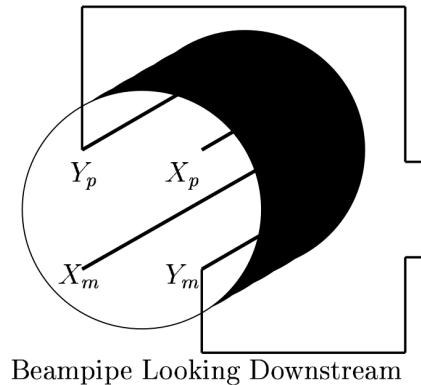


Figure 2.22: Schematic plot of stripline BPM

where the proportional constant S_x (S_y) is the position sensitivity. The pickup voltage responds linearly to beam displacement when the displacement is small. In the case of Hall A BPMs, the 4 striplines are rotated 45° w.r.t. to hall coordinate system, so a 45° rotation is needed to recover hall (x, y) from extracted BPM (x', y').

Besides these stripline BPMs, PREX-II and CREX also utilized 3 cavity BPMs (see discussion below), shown as bpm4b/c/d between bpm4a and bpm4e in Fig. 2.21, to measure beam conditions for low current calibration runs, because stripline BPMs don't work when beam current is lower than 0.5 μA . These cavity BPMs were not used in normal production runs.

2.4.2 BCMs

One technique to measure beam current is current transformation. Various BCMs based on this idea may have different designs, features and performances, the key component is the same – current transformer (CT). When beam bunch travel through the beam pipe, it will induce a magnetic field in the beam pipe (the core), which in turn will induce a current in the secondary winding (toroid), whose output is proportional to the beam current. To make a precise measurement, it is important to shield any outside magnetic field and separate the segment of beam pipe where the BCM lies in from the rest.

The BCM system in Hall A consists of two radio frequency (rf) cavities and an unseer monitor in between, the unseer monitor is a parametric current transformer (PCT), which will output a DC voltage equivalent to 4 mV per μA of beam [?]. In PREX-II and CREX, the Unser monitor was not used for beam current measurement, because its voltage output drifted quickly after only a few minutes of running, instead, it was used to calibrate the rf-cavity monitors on either side of it, whose readout was what we used for runtime beam current measurement.

A rf cavity is a metallic chamber that sustains an electromagnetic (EM) field (infinite number of resonant EM modes), by special design of its shape, a particular EM mode can efficiently transfer energy to or from a charged particle. The frequently heard accelerating cavity need to provide a electric field along beam velocity direction. While a decelerating

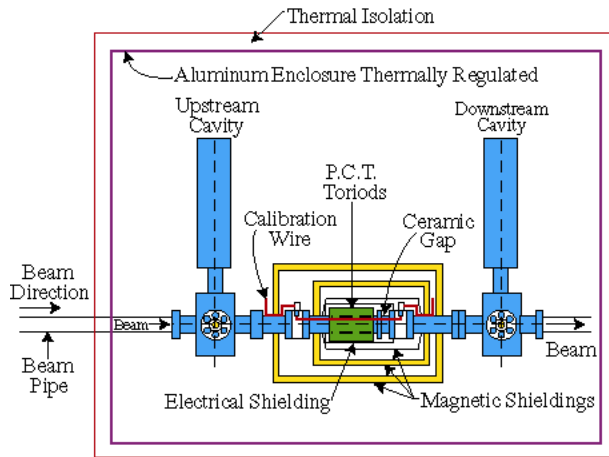


Figure 2.23: Hall A BCM system [?]

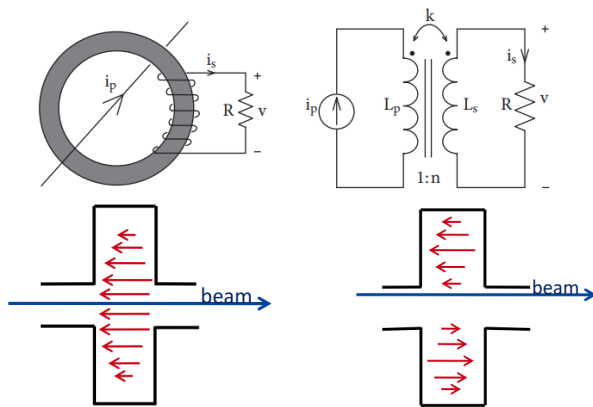


Figure 2.24: Up: Schemtaic plot of current convertor; Down: TM_{010} and TM_{110} modes, the red arrows are electric field

cavity, which will absorb energy from the coming charged particles, can be used as beam diagnostic monitors. The induced voltage is proportional to the traversing charge q :

$$V = 2k_{loss}q \quad (2.23)$$

where k_{loss} is the loss factor, which depends only on the electric field distribution, therefore is sensitive to beam position and particle velocity. To measure beam intensity, one would prefer the EM mode whose electric field doesn't depend on r position, these are TM_{010} like modes; while for measurement of beam position, exactly the opposite is wanted, the electric field should have an azimuth angle and r dependence, which are TM_{110} like modes.

The 2 rf-cavity current monitors are of Pill box type (the electric field is concentrated near axis, while the magnetic field is concentrated at outer cylindrical wall), which operates at TM_{010} mode. The voltage readout will be downconverted to lower frequencies signals, then filtered, amplified and further precessed before writing into the data

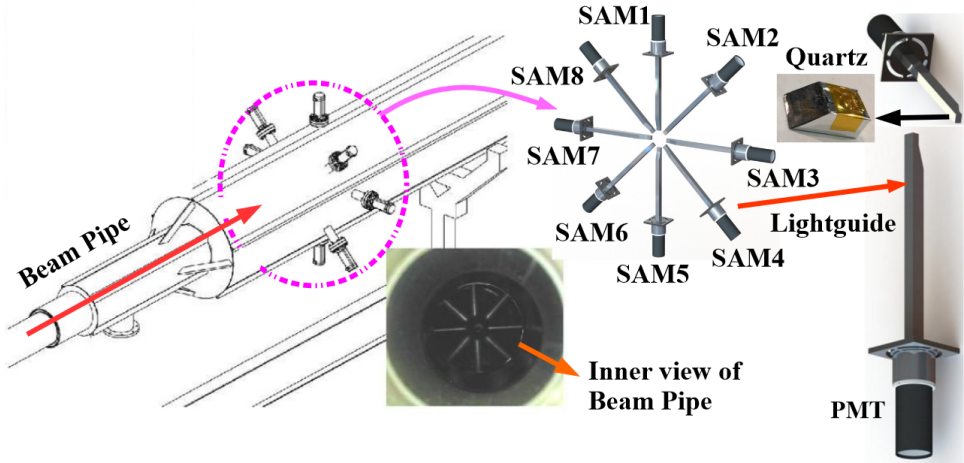


Figure 2.25: Layout of SAMs[?] ??

stream. Due to non-linearity at low current region, actually 3 signals (the same signal with different gains: x1, x3 and x10) will be recorded [?].

2.4.3 SAMs

For further understanding of beam dynamics, electronic noise and possible target boiling effect, a luminosity monitoring system, called the small angle monitors, was installed in the dump pipe, about 7 m downstream of the target pivot. As shown in Fig. ??, the SAMs system consist of 8 detector modules, symmetrically positioned around the dump pipe. Each detector module has a quartz tile (active detector), attached to a lightguide, the Cherenkov light will be read out by a PMT at the end of the lightguide. As its name implies, SAMs are designed to monitor small angle ($\sim 1^\circ$) scattered and secondary flux from the target, thus it can also be used to inspect the target conditions, e.x. a bubble in the target that forms and disappears within one helicity window is unknown to both BPMs and BCMs, but SAMs will see it. SAMs' readout is sensitive to beam parameters, e.x., the sum of a symmetric pair monitors is sensitive to change in beam current and energy while their difference tells the fluctuation in beam position and angle. The symmetric design helps to disentangle these beam parameters. So it provide an independent check of the measurement of BPMs and BCMs and can be used to eliminate possible beam or electronic noise.

2.4.4 Beam Modulation

Another system we see in Fig. 2.21 is the beam modulation system, which lies in beamline arc right after Beam Switch Yard where electron chains are separate into Hall A/B/C beams. It consists of 6 air-core coils and an energy vernier in the last cavity of south LINAC, the total number of 7 coils provides a redundancy w.r.t. the free number

of degrees of beam phase space, making sure to cover all beam phase space at target. Coil (trim) 1, 3, 5 are responsible for modulating beam x position and coil 2, 4, 5 will modulate beam y position. These coils (vernier) are driven by a VME-DAC, which in turns is controlled by the parity DAQ. It takes 4.267 s for each coil (vernier) to modulate the beam, a whole modulation cycle takes 85.68 s (~ 1 beam modulation every 10 mins during run time).

The beam modulation system was used for false asymmetry correction, together with regression. When beam was modulated, BPMs and detectors will record corresponding change in their readout, to calculate detector sensitivity w.r.t. jitter in beam parameters. Therefore, the modulation should be much larger than the natural jitter in the beam, a typical position modulation will be about $100 \mu\text{m}$ (FIXME) and the energy vernier will result in a beam displacement of 0.75 mm in BPM 11/12.

2.5 Target

For the sake of statistics, the designed current was quite large, as shown in Table. ???. With such high current, the electron beam will deposit quite a lot of heat on the target, it will be a disaster if we can't take away these heat as soon as possible to keep a stable target temperature. For PREX-II, because Pb itself is not a good thermal conductor ($35 \text{ W/m} \cdot \text{K}$), auxiliary diamond foils ($> 1000 \text{ W/m} \cdot \text{K}$) were used to form a D-Pb-D sandwich target to help heat dissipation. The thickness of the diamond foil matters, one lesson we learned from PREX-I was that with thin (0.15 mm) diamond foil, the thermal conductivity of the diamond foil dropped greatly (from $1000 \text{ W/m} \cdot \text{K}$ to $100 \text{ W/m} \cdot \text{K}$) after about 1 week of running with $70 \mu\text{A}$ cw beam, resulting in some Pb targets melted. While a thicker diamond foil (0.25 mm) will protect Pb foils from melting under the same conditions. In PREX-II, a factor of 2 safety margin was adopted, conservatively assume 1 week running for each Pb target, 35 PAC days of beam time requires 5 targets, and we deployed 10 isotopically pure Pb sandwich targets with thick diamond layers to ensure the success of PREX-II, each new target was able to sustain up to $85 \mu\text{A}$ cw beams.

While Ca itself is an excellent thermal conductor, no need for auxiliary materials and higher current can be applied. Isotopically pure ^{48}Ca (the original target we used had a purity of 95.99%) is much more expensive than pure ^{208}Pb target, so only one ^{48}Ca target was prepared for CREX. After the target accident, the new ^{48}Ca target was a stack of 3 separated foils with similar total thickness.

Targets were firmly mounted in bays of target ladders, whose axes were perpendicular to the beam line. The ladder was movable along its axis by an AC servo-motor, which can receive remote instructions through internet. The motion along ladder axis can be precise to $\sim 12 \text{ nm}$. There are 2 target ladders in total, one for production targets and the other one for calibration targets. The production-ladder had 10 ^{208}Pb targets, two Calcium isotope targets: ^{40}Ca and ^{48}Ca , and 4 other calibration and diagnostic targets, 16 target slots in total. The calibration-ladder had 5 targets, a carbon hole, a watercell, a thin C foil, a thin natural Pb and a thin ^{40}Ca target. The calibration-ladder was rotated

45° w.r.t. the production ladder, which was along the lab x axis, as shown in Fig. 2.26 and 2.27.

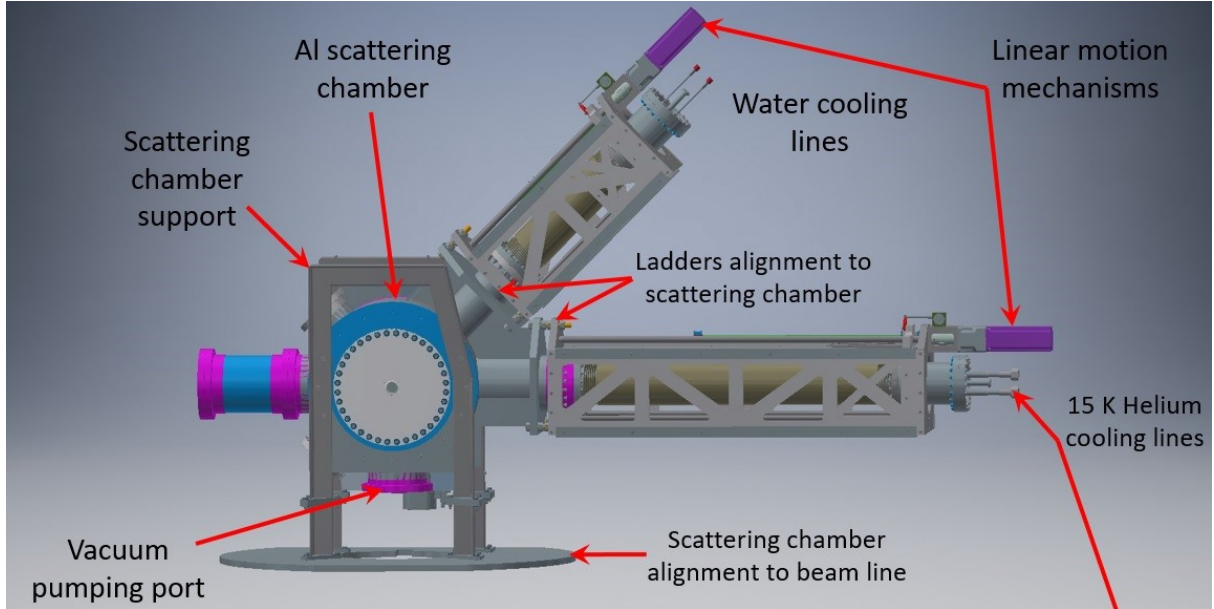


Figure 2.26: Scattering chamber of PREX-II/CREX

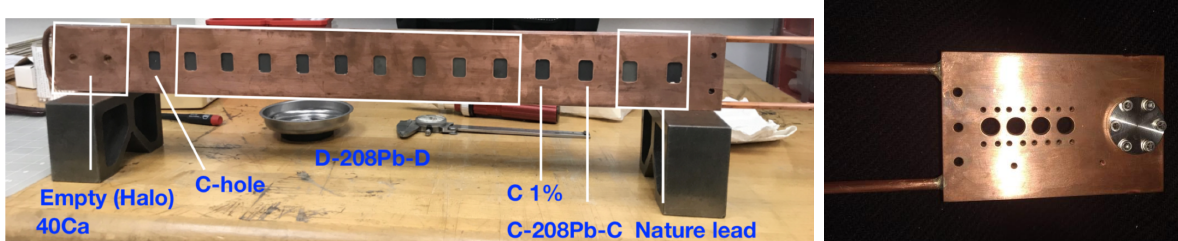


Figure 2.27: Production target ladder and calibration ladder

The ^{40}Ca and ^{48}Ca targets were installed on the cold heat sink in dedicated cylindrical sockets at the end of the production ladder. The fact that the ^{48}Ca and the ^{208}Pb targets share the same ladder means they actually had the same z location, therefore the same scattering angle (CREX scattering angle was proposed at 4°), to simplify the design, construction and installation of the target chamber.

Special care was needed for ^{48}Ca target, the pressure should be less than 10^{-6} torr to avoid Ca oxidation. The vacuum of the target chamber was maintained by a turbo-molecular pumping system, which created a 10^{-7} (10^{-8}) torr vacuum for the calibration (production) ladder in the target chamber. What's more, gate valves were closed to isolate the target chamber from upstream and downstream beam pipes when beam was not on. By way of precaution, a nitrogen purge system was installed to purge air in case of possible leak. Every time we warmed up the ^{48}Ca target, boiling was needed before restarting data taking.

2.5.1 Target Cooling

The production ladder was cryogenically cooled due to high power from electron beam, while the calibration ladder was water cooled, the calibration runs need only $\lesssim 1 \mu A$ level beam current. Both ladders were made of cooper, the cooper frame of the production ladder was cooled by $15 K$, 12 atm gaseous helium, which runs through the cooling tube surrounding the frame. Contact between the target and the frame and within each layer of the ^{208}Pb sandwich target is also important. Belleville washers were used to clamp the lead and diamond foils to ensure contact as temperature changes in the beam, besides, a thin layer of Apiezon L vacuum grease was applied to their interface to improve heat conductivity. In the diamond/copper interface, a silver-based paste compound was used for the same purpose. For D-Pb-D sandwich target with thick C foil, the heat loading will be $100 \text{ W}@70 \mu A$ with a $4 \times 6 \text{ mm}$ raster, the cooling system would keep the Pb target stay at $\sim 60 K$ (melting point at $600 K$) assuming good contact and smooth heat conduction. For ^{48}Ca target, With $150 \mu A$ beam current, it will produce about 370 Watts heat on the target, which raised the target temperature up to $\sim 300 K$ (melting point at $1115 K$).

2.5.2 Raster

Although the target foil was cooled to about $20 K$ (PREX-II), it still deformed (even melted) under electron's bombardment. Small nonuniformities in the target thickness vary the scattering rate, and over the course of the experiment they eventually generated enough noise to swamp the tiny weak-scattering signal. Actually, this is how we inspect the status of a target and evidence to replace a target if the measured asymmetry width increase significantly.

The solution to this problem is the raster, which is a set of dipole magnets that deflect the beam at about 25 kHz to spread the beam on the target. What we learned from PREX-I was that we could significantly reduce the sensitivity to target-thickness variations by synchronizing the helicity flipping frequency with the raster frequency so that it sampled different areas on the target. As shown in Fig. 2.28, the Lissajous pattern we got depends on the frequency difference between X and Y, the larger the frequency difference, the larger the scanning area. The ratio of f_y/f_x should be an irrational number to prevent a closed Lissajous pattern. The actual frequencies we used were 25.44 and 24.48 kHz , for PREX-II, the raster size was $4 \times 6 \text{ mm}$, and CREX had a raster size of $2 \times 2 \text{ mm}$.

Another reason for having raster is heat dissipation, the larger the raster size, the quicker the heat dissipation will be, the lower the target temperature, as shown in Fig. 2.30.

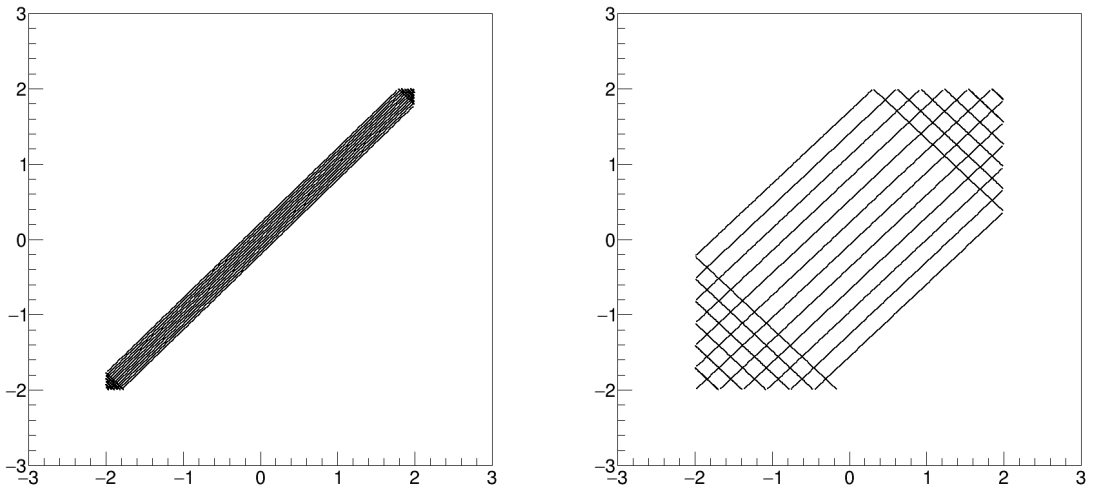


Figure 2.28: Raster pattern with different frequency difference between X and Y. Left: $|f_y - f_x| = 120 \text{ Hz}$; Right: $|f_y - f_x| = 8 * 120 \text{ Hz}$. The raster shape is a $4 \times 4 \text{ mm}$ square.

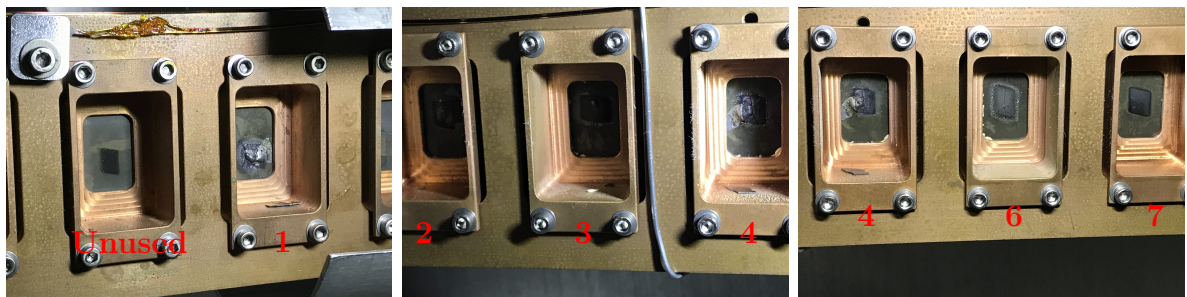


Figure 2.29: Picture of Pb targets after running, one can see clearly the shape of raster.

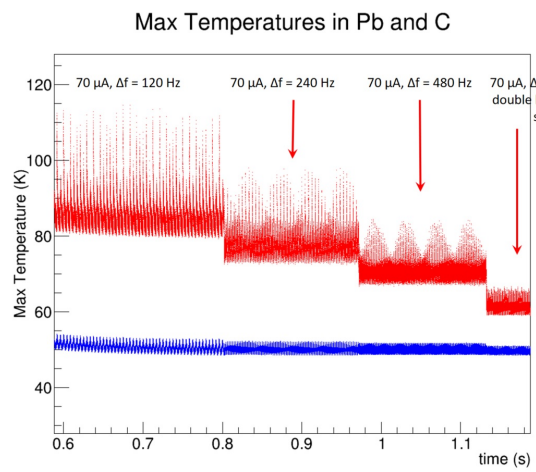


Figure 2.30: How the target temperature change with size of raster area.

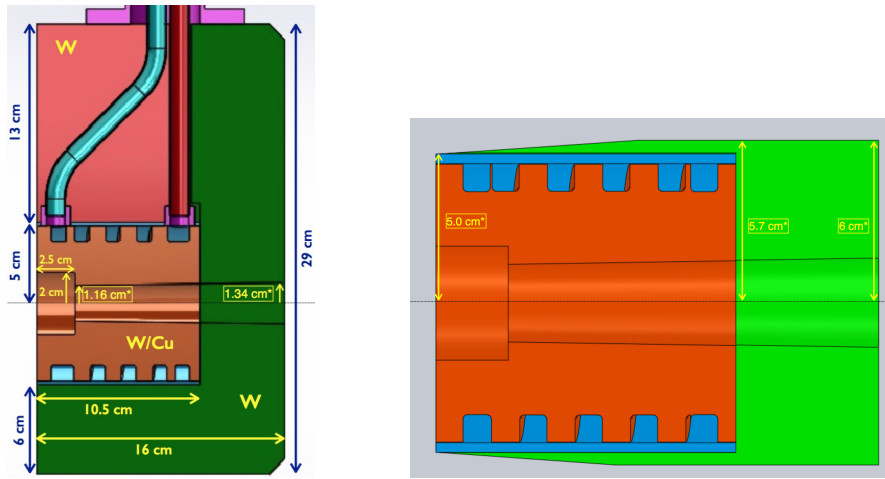


Figure 2.31: Side and top view of beamline collimator. Beam from left to right.

2.5.3 Beamlne Collimator and Sieve Slit Collimators

Another problem that failed PREX-I was the excessive radiation, which damaged electronics in the Hall and the o-ring on the target exit flange leading to leaks and ultimately halted the experiment. With this experience, the new design of the pivot area (the center of the 2 HRS where the target chamber lies in) for PREX-II and CREX payed more attention to radiation near the target region. The idea was to lead as much radiation to beam dump as possible, and absorb the rest radiation in one key component – the beamline collimator, which was placed 83 cm downstream of the production target. The beamline collimator consists of an inner collimator and a housing jacket made of sintered tungsten; the inner collimator, in turn, has the same structure of a 70% W/30% Cu alloy collimator and a copper jacket. As shown in Fig. 2.31, there is cylinder notch in the front of the inner collimator, to make sure the electrons/radiation are completely absorbed inside the collimator. The beamline collimator was water cooled, with maximum heat loading of about 3.65 kW from Pb target. The power on the beamline collimator was another signal for the degradation of target. When the temperature of the outgoing water increased dramatically, it was time to replace the target. as shown in Fig. 2.32

Besides the beamline collimator, a few other devices were installed to further eliminate the radiation level in the hall. These devices include the high-density polyethylene (HDPE) neutron shield around the beamline collimator region and a skyshine shield consisting of a 6 cm thick tungsten block and massive concrete blocks. These extra shields were used to block high energy neutrons from the collimator.

On both sides of the beamline collimator were the sieve slit collimators, which were used for optics study, helping electron trajectory reconstruction. When we took production data, the sieve slit collimators were moved out of the spectrometer acceptance; when we took optics data to measure the scattering angle and Q^2 , the sieve slit collimators were put in to cover the whole spectrometer acceptance, without interfering the inner bore of the the beamline collimator. With known (x, y) information of each hole in the

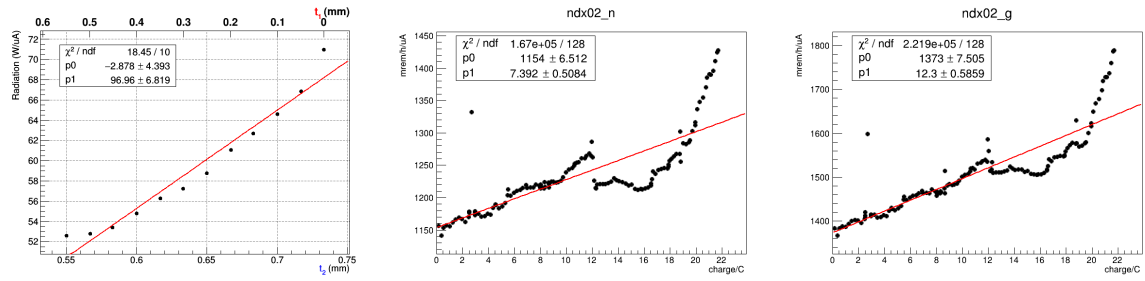


Figure 2.32: Left: a simple model of target degradation – assuming the inner foil (t_1) is becoming thinner and the outer foil is becoming thicker (t_2) while the total mass keeps intact. The plot shows how the power deposition on the beamline collimator change in this model. Middle and Right: actual neutron and photon radiation level monitored along charge accumulation. They show similar trends.

sieve plane, together with the vertical drift chamber (VDC) tracker, we can reconstruct the beam transport matrices.

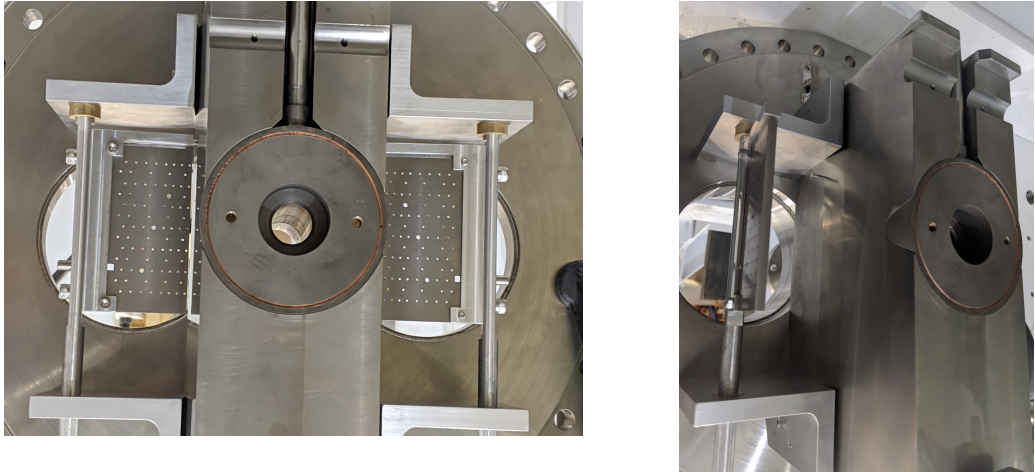


Figure 2.33: Front picture of beamline collimator and sieve slit collimators, looking downstream. One can clearly see a cylinder removed from the central collimator. The sieve planes lie after the beamline collimator and are movable like a door, it can be opened or closed remotely.

2.5.4 Septum

The septum magnet is required to bridge the scattered electrons at small angle into the HRS. As said before, the designed scattering angle is about 5° while the smallest angle that HRS can reach is 12.5° , so we need the septum magnet to guide the scattered electrons into HRS.

The septum magnets are normal conducting magnets that consist of 3 coils, by applying large current, it will produce a strong magnetic field (up to ~ 1 T in the central

region). A non-magnetic stainless vacuum box will connect the upstream collimator box and the downstream HRS vacuum pipe on both sides of the septum. The septum beampipe (the one that leads to the beam dump) is made of magnetic stainless steel to shield the magnetic field from the septum, on both ends of the septum beampipe, there are magnetic steel box to shield the fringe magnetic field from septum.

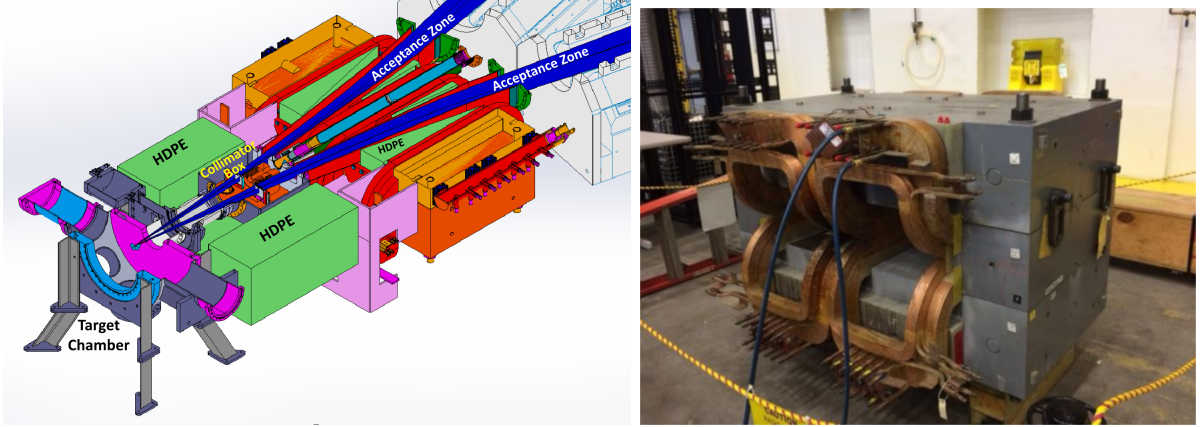


Figure 2.34: Left: septum (the red coils) in the pivot region; Right: picture of septum.

2.5.5 High Resolution Spectrometer (HRS)

The key component of every Hall A experiment – spectrometer. The most frequently used ones are the high resolution spectrometer pair. Each HRS consists 3 superconducting quadrupoles and 1 dipole. The maximum magnetic field of the 3 quadrupoles are 1.2, 1.0 and 1.0 T respectively while the dipole can provide up to 1.7 T field. The incoming electrons will be bent 45° up in the vertical plane and then received by the following detectors. HRS has a small angular acceptance (± 28 mr horizontally, ± 60 mr vertically, the solid angle being 7.8 msr), but can move over a wide range of angle around the hall (12.5° – 165°). As its name implies, it achieves a very high momentum resolution at the 10^{-4} level over a wide range of momentum (0.8 – 4 GeV). This capacity helped us to reject most of inelastic electrons, because a small difference in electron momentum (2 – 3 MeV) will lead to large separation in the detector plane, thus leaving us a relative clean data with very small background from inelastic scattering.

Before the entrance of Q1 quadrupoles was the Q1 collimator, which defined the spectrometer acceptance. It was strictly required that the symmetry between left/right, and up/down of Q1 collimators should be preserved to reduce any possible systematic uncertainties.

2.5.6 Detector Package

The standard HRS detector package on each arm consists of trigger scintillators for triggering, a pair of VDCs for particle tracking, Cherenkov type detectors and shower

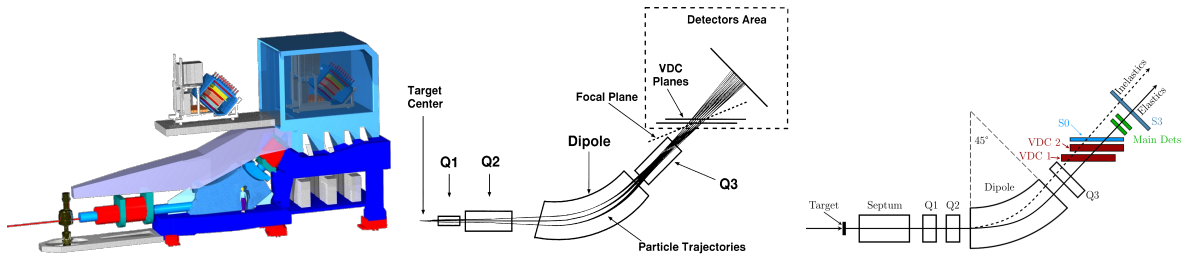


Figure 2.35: Schematic plot of HRS and particle rays inside it. [?] The 'focal plane' in the middle plot, by design, should be at an angle of 45° w.r.t the central ray, but is actually rotated to 70° due to lackness of sextupole winding in Q3. When we talk about the HRS focal plane, we usually refer to the VDC lower plane.

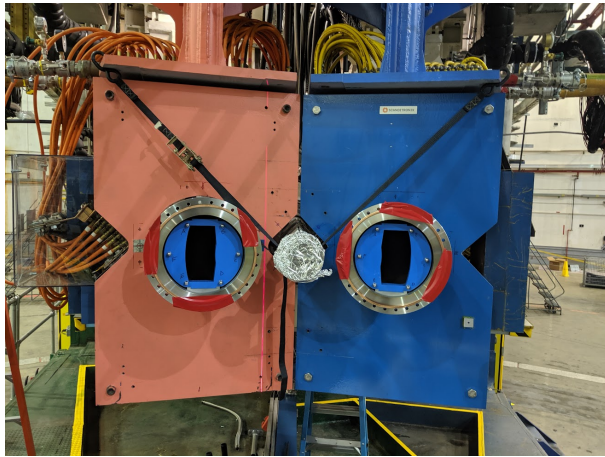


Figure 2.36: Picture of Q1 collimator pairs

counters (calorimeters) for particle identification (PID). In PREX-II and CREX, we needed only part of these detectors, namely VDCs and S0/S3 triggers, others were removed for safety. We built our own Cherenkov counters that can work in the so called 'intergrating mode'.

Vertical Drift Chamber (VDC)

Each VDC detector package consists of 2 drift chambers, one lower and one upper chamber with a vertical separation of 0.23 m (0.335 m between the same U or V planes of the lower and upper chamber), to enable precise position and angle measurement. The drift chamber is actually a multiwire proportional chamber (MWPC) with 2 layers of sense wires – U and V planes in the lab horizontal plane, which are orthogonal to each other and has a vertical separation of 26 mm . Each wire plane consists of 368 tungsten wires with the width of adjacent wires being 4.24 mm , corresponding to 6 mm in the spectrometer cross section due to the 45° cross angle between the central ray and the VDC plane. The ion's drift time in the chamber are used to reconstruct particle trajectory. The single plane can achieve a position resolution of $\sim 235\text{ mm}$ FWHM, the angular

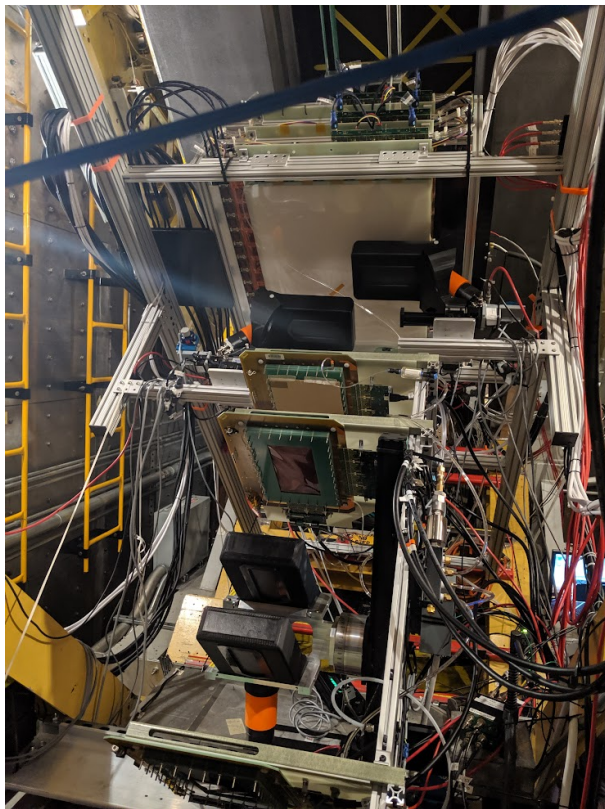


Figure 2.37: The detector package

resolution is 6 mrad FWHM for θ (out-of-plane angle) 2.3 mrad for ϕ (in-plane angle) [?].

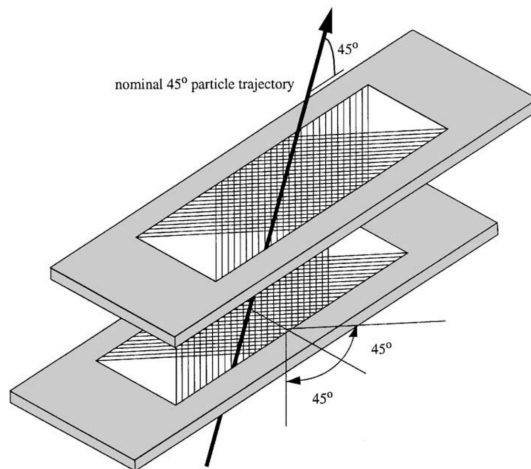


Figure 2.38: Schematic plot of VDCs showing UV wires [?]

VDCs were only used for optics runs in PREX-II and CREX, when we collect electrons one by one to measure their scattering angle and energy, otherwise they were turned off during normal production runs.

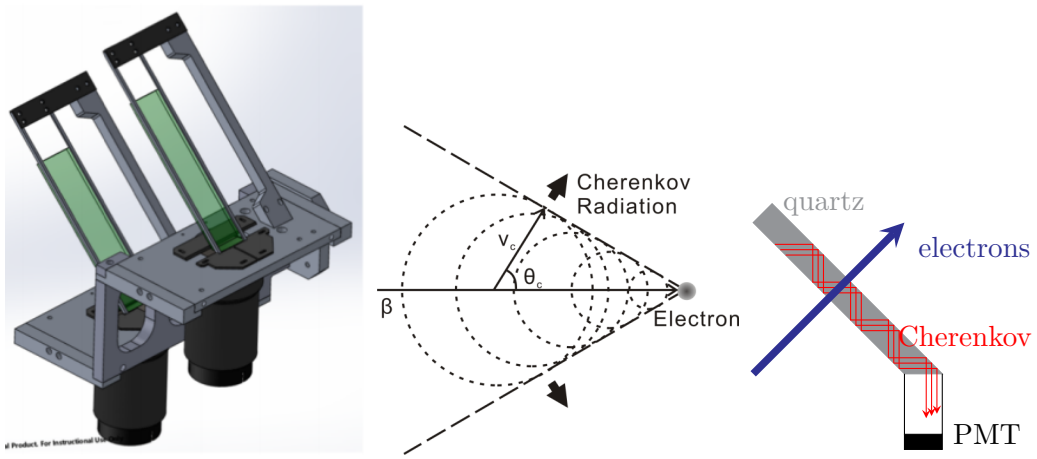


Figure 2.39: Left: CAD drawing of the quartz detector; Middle: schematic plot of Cherenkov radiation, the angle between electron and the Cherenkov radiation is $\cos \theta = \frac{v_c}{v_e} = \frac{c}{nv_e} = \frac{1}{n\beta} \approx \frac{1}{n}$; Right: electron flux goes through a quartz detector.

Trigger

Same as VDCs, triggers were only used in counting mode for optics study. The standard detector package consists of multiple trigger planes, and we used only 2 of them: S0 and S3 plastic scintillators. The S0 scintillator locates between VDCs and the main detectors while S3 lies behind the main detectors, they have a sensitive area of 170 cm long by 25 cm wide. Their signals were logically combined to provide different trigger rate. The trigger rate was controlled to be less than 50 kHz most of the time (the up limit of VDC is about 250 kHz).

Main Detector

The main detector of PREX-II and CREX was the 5 mm thick fused silica (quartz) tiles, with a size of 16 cm long by 3.5 cm wide (3 cm \times 3 cm active area). 2 identical quartz detectors were installed with the upstream one used as the main detector and the downstream one as the backup (also used for a cross check in PREX-II). They are tilted to be perpendicular to the electron rays. The high refractive index of quartz ($n \approx 1.45$) means the opening angle θ in Fig. 2.39 is about 46°, larger than the critical angle to make total internal reflection ($\theta_c = \arcsin \frac{1}{n} = 43.6^\circ$), therefore, the Cherenkov light produced by high energy electrons will be totally reflected inside the quartz and finally collected by the PMT. The high photon yield make it easier to resolve the electron peak, which was beneficial given the fact that non-linearity of the PMTs is one of the major contributors to systematic uncertainties.

The width of the photon-electron distribution will increase the statistical uncertainty:

$$\sigma_A = \sigma_{stat} \times \sqrt{1 + \left(\frac{\sigma_{PE}}{\langle PE \rangle} \right)^2} \quad (2.24)$$

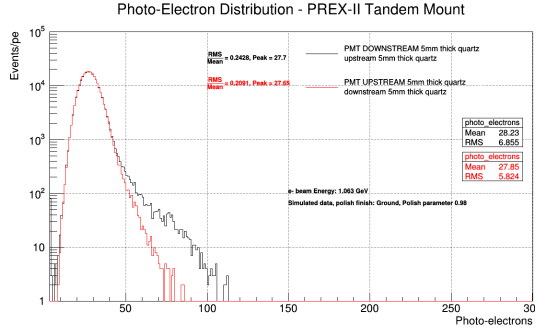


Figure 2.40: Simulation result of photo-electron (PE) spectrum for single electron passing through the main detectors. The wider tail in the downstream detector is due to particle showering in the upstream quartz. Plot from Devi Adhikari.

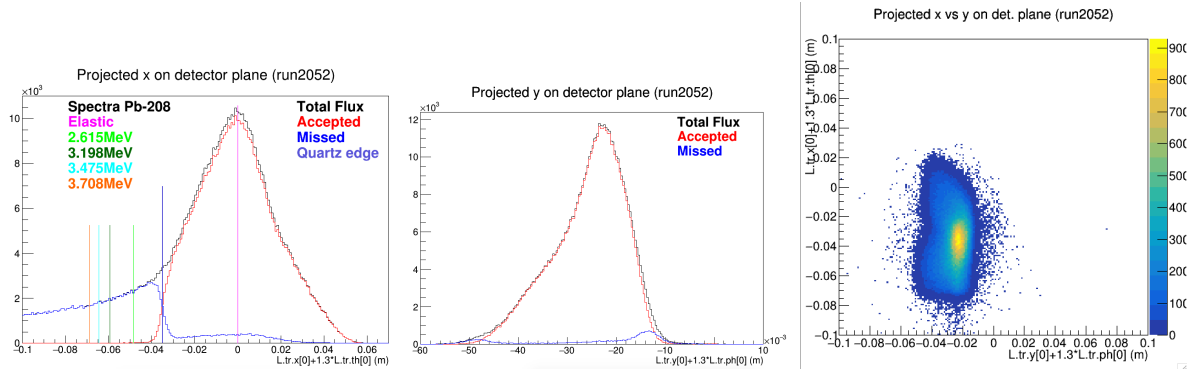


Figure 2.41: Data of x,y distribution on quartz. Plots from Devi Adhikari.

where σ_{PE} is the RMS of the distribution. The RMS can be parameterized into 2 parts: the Gaussian principle part which is inversely proportional to the quartz thickness and a Landou tail which comes from the showering process and is proportional the thickness. The final decision of 5 mm of thickness was a compromise between these 2 parts to minimize detector resolution $\frac{\sigma_{PE}}{\langle PE \rangle}$: thicker to increase photon-electron yield and thinner to reduce showering.

There was a homemade motion control system in each arm to move the main detectors remotely, which allowed us to tune the position of the main detectors when we changed gain of the main detectors under a different beam current.

AT Monitors

About 1 m downstream the main detector were a pair of AT monitors, as shown in Fig. 2.37, which used exactly the same quartz piece as the main detectors. They were used to monitor transverse polarization in the beam.

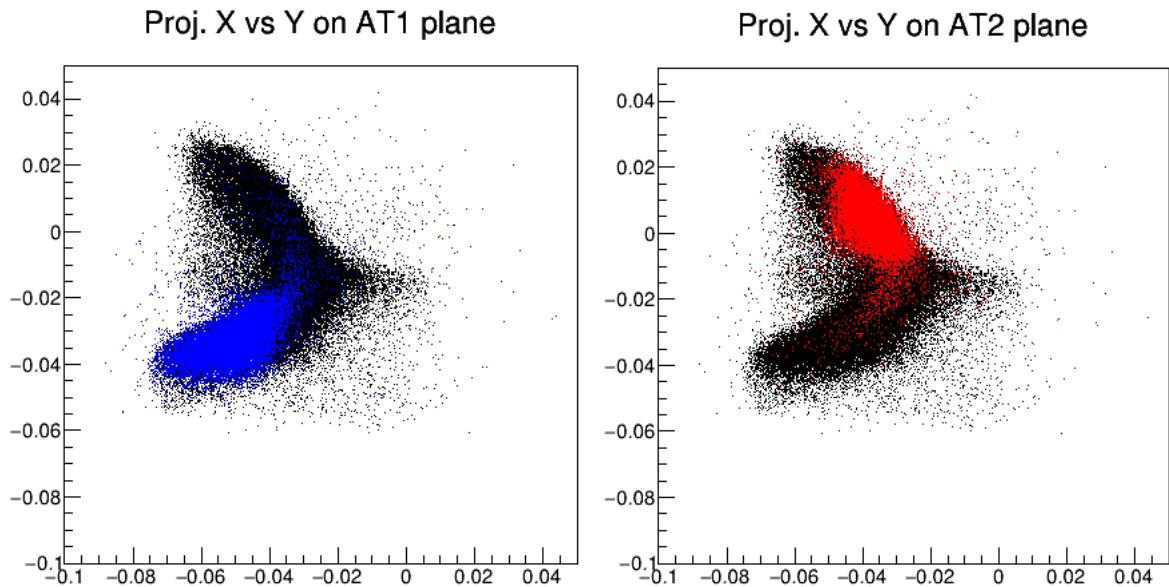


Figure 2.42: Scatter plot of electrons on the AT monitor plane. Red and blue represent events with opposite transverse polarization.

2.5.7 Data AcQuisition (DAQ)

CEBAF Online Data Qcquisition (CODA) system We use to pseudo random number generator to decide the helicity pattern, which will trigger the data taking of both detectors and monitors. DAQ will read data from PCs, BPMs, BCMs and detectors, which will then be digitalized by a 18 digits ADC. In one helicity window, they will sample ??? times, which will be grouped into 4 blocks. The sum of the 4 blocks was what we got.

The integrated response of each detector and beam monitor was collected and sampled by a custom 18-bit ADC for each helicity window.

Integrating mode and counting mode

Chapter 3

Data Analysis

As mentioned before, though of fast flipping and tremendous effort to keep electron beam in exactly the same conditions (intensity, energy, position and angle on target) through opposite helicity states, life is not easy and there is no way to achieve such a goal, after all, no one can understand completely and control every aspect of something as complicated as an accelerator. There is always various noise caused in various parts of the machine, though very small in general sense, they are large compare to what we want to measure, and actually the largest correction to PV asymmetry. So we need to remove such noise in the raw asymmetry we measured.

We use the same methods to process both PREX-II and CREX data, therefore we will talk about only CREX data here.

CREX started commissioning around December 2019, we took the first good run on Dec 12. 6 slugs (slug 100 - 105) were collected before the Christmas. After the Christmas break, data taking was resumed until Jan 18 2020 when the ^{48}Ca target was damaged accidentally. It tooks 5 days to prepare a new ^{48}Ca target. Things moving on quite smoothly, we had 2 days of transverse asymmetry measurement from Feb 10 to Feb 12. We were a little over halfway on data taking when Covid-19 hitted and the lab was shut down at the end of March 2020. Fortunately, things came back 4 months later, we had

variable	quadtets	minirun	run	slug
count	86840789	8527	1386	121
raw asymmetry (ppk)				
corrected asymmetry (ppk)				
bpm4aX				
bpm4aY				
bpm4eX				
bpm4eY				
bpm12X				

Table 3.1: CREX Data Set

variable	regression	dithering	Lagrangian
slope correction (ppm)			

the chance to continue data taking for about 1 month. The experiment stopped data taking on Sep 18 2020. A total charge of 480 C was collected, among which 390 C was good charge. The dataset was clearly separated into 3 parts: before AT, after AT (before Covid) and after Covid, which we will talk about later.

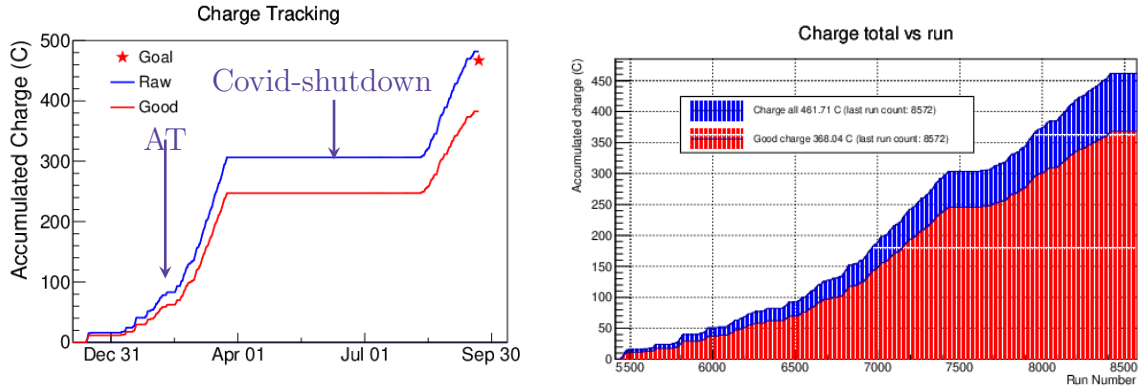


Figure 3.1: Charge accumulation versus time (left) and run number (right). The long plateau on the left plot is due to Covid shutdown, which is shown around run 7500 on the right plot. We see that data taking is most efficient after AT (before Covid), the last month (after Covid) is not bad while the first 2 months is not so efficient due to various problems.

CREX collected 1451 production runs, among them, 1386 were identified as ‘Good’ and used for final analysis. The good runs consists of 1362 both arms runs, 6 left arm runs and 18 right arm runs. Each good production run took about 1 *hour* and collected about 0.3 C charge with a charge efficiency of 80%.

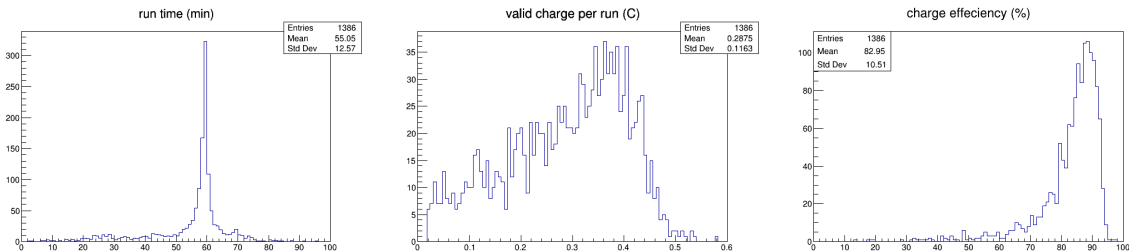


Figure 3.2: Statistics of CREX runs

Though electrons come bunch by bunch, the bunch frequency of 249.5 *MHz* is much larger than our helicity frequency of 120 *Hz*, so electron beam can be regarded as continuous. All electrons within one helicity window will be integrated as 1 record. Every 4

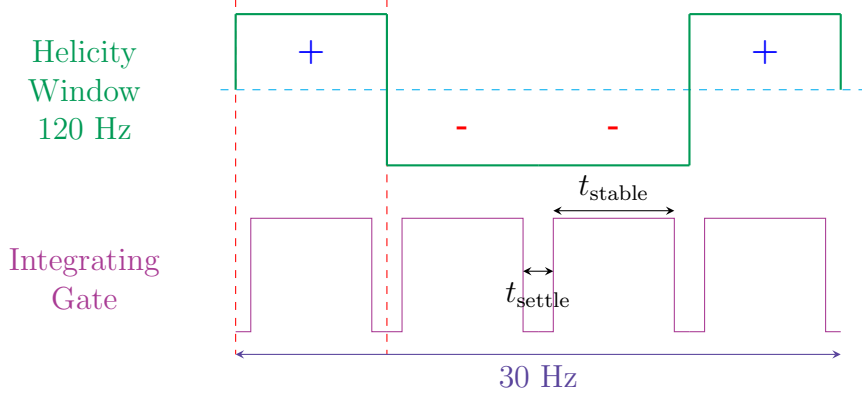


Figure 3.3: For CREX, $t_{\text{settle}} = 90 \mu\text{s}$, to allow the PC stabilizes after flipping, avoiding any cross effect from last helicity state. The deputy factor is 98.92%.

continuous helicity window data is grouped as quadruplet in order to cancel the 60 Hz noise in line power, and asymmetry will be calculated based on quadruplet – this is what we called one asymmetry event. So the asymmetry event frequency is 30 Hz. CREX collects ??? such good asymmetry events.

Every run is separated into multiple miniruns to account for the fact beam conditions is changing quickly, it is inappropriate to calculate slope values over a 60 mins run. Minirun will be more proper, the beam conditions, and therefore the slope value should be more stable during such a shorter time period. Every minirun contains 9000 good (pass cut) events (5 mins), the last minirun contains whatever number of good events that can't be divided into 2 miniruns. CREX has 8543 miniruns from 1386 runs, among them, 16 miniruns are discarded due to noisy beam conditions that were not caught in the previous 2 respins. To avoid any respin, these miniruns are simply removed, which counts ??? C.

Runs will be grouped into slugs. One slug is defined as all runs before the next IHWP flipping. With good beam conditions, we could collect 3 slugs per day, so each slug took about 8 hours or longer in case of any accidents. CREX collects 124 slugs, after data clean and combination to remove slugs with only 1 runs, 121 slugs are kept.

Finally, slugs will be grouped into part, with different wien flip status. We have 3 parts as said before.

Cut

We have only very loose cut on data to keep as much data as possible. The online cuts include a current cut and some stability cuts. The current cut requires the beam current no smaller than $15 \mu\text{A}$ below the nominal current, due to non-linearity in monitor/detector response. The stability cut says ???

a few miniruns are discarded

Beam Current

We have 5 bcms and the upstream analog bcm is used as the target current monitor. where are the 5 bcms why choose bcm_an_us as bcm_target?

- non-linearity from electronics read out: false asymmetry. PMT → preamplifier → ADC

Data quality:

- Beam excursion: data quality cuts are applied to remove unstable beam periods
FIXME: a plot for beam excursion

3.1 Raw Data

What we call one event is all electrons counted in one helicity window. The asymmetry value is calculated using every 4 (8 in PREX-II) helicity windows (++ or -++) to cancel the 60 Hz line power noise. The helicity pattern was chosen pseudo-randomly. The CREX data consists of ??? event.

ErrorFlag

beam jitter ??? in position, ??? in energy and ??? in time scale

Every event is accompanied by a set of beam parameter values, recording the beam conditions in that helicity window. A series of cut will be applied, basing on the beam stability, to select good charge.

Pair value

For any 2 continuous events, define their pair value as: For BPM/BCM, the pair difference is:

$$diff = \frac{v^+ - v^-}{2}$$

For usl/usr, the asymmetry is:

$$asym = \frac{v^+ - v^-}{v^+ + v^-}$$

Redundant Position Measurement

stripline BPM vs Cavity BPM

3.1.1 Measured Asymmetry

3.1.2 Beam False Asymmetry

Can we count number of electrons from detector read out?

3.2 Regression

Regression is the most common statistical method to identify the relationship between dependent variables (Y) and independent variables (X). Bear in mind that regression itself doesn't tell us any relationships or rules, it only works under the assumption that the relationship of variables is predictable (given by the user) and the dependent variables follow a known distribution function $P(\epsilon)$, again, needed to be told by the user:

$$Y = f(X) + \epsilon$$

With these prior knowledge, regression is able to calculate the most likely coefficients in the predicted model.

For example, the famous least square fit is actually a linear regression

$$Y = c_0 + \sum c_i x_i + \epsilon$$

assuming Gaussian distribution of the dependent variable: $\epsilon \sim N(0, \sigma)$ Another frequently used scene is logistic regression for classification, which is very similar to linear regression except $f(X)$ will be converted into a probability function, e.x. using the logistic function:

$$h(z) = \frac{e^z}{1 + e^z} \quad z = f(X)$$

3.2.1 The Model

Considering one monitor and one detector. Assuming the reading noise of detector follows the Gaussian distribution and the monitor is precise:

$$\begin{aligned} M &= m \\ D &= d + \epsilon(0, \sigma_0^D) \end{aligned}$$

Here, M (D) is the measured value while m (d) is the true value and σ_0^D is the variance of the noise for Detector.

Then the difference between beams of opposite polarization will follow also the Gaussian distribution with a larger variance:

$$\begin{aligned} \Delta M &= M^+ - M^- = d^+ - d^- = \Delta d_0 \\ \Delta D &= D^+ - D^- = (d^+ + \epsilon(0, \sigma_0^D)) - (d^- + \epsilon(0, \sigma_0^D)) = \Delta d_0 + \epsilon(0, \sqrt{2}\sigma_0^D) = \Delta d_0 + \epsilon(0, \sigma_1^D) \end{aligned}$$

Again, Δm_0 (Δd_0) is the real difference between the different polarized beams while ΔM (ΔD) is the measured value.

The probability for measuring ΔD will be:

$$P(\Delta D) = \frac{1}{\sigma_1^D \sqrt{2\pi}} e^{-\frac{1}{2} \left(\frac{\Delta D - \Delta d_0}{\sigma_1^D} \right)^2}$$

We will have a bunch of independent data points: $(\Delta M, \Delta D)_i$ and we want to extract the relationship between Δd_0 and Δm_0 : $c \equiv \frac{\partial d}{\partial m}$ – given the tinyness of δm , first order is precise enough. This is exactly a linear regression problem.

$$\Delta d = 0 + c\Delta m$$

For any real data point $(\Delta m_0, \Delta d_0)_i$, the possibility to measure $(\Delta M, \Delta D)_i$ is:

$$P_i(\Delta D | \Delta M) = \frac{1}{\sigma_1^D \sqrt{2\pi}} e^{-\frac{1}{2} \left(\frac{\Delta D - c\Delta M}{\sigma_1^D} \right)^2} \quad (3.1)$$

For the accumulated data of one minirun, the total probability will be:

$$P = \prod_i^n P_i(\Delta D | \Delta M) = \prod_i^n \frac{1}{\sigma_1^D \sqrt{2\pi}} e^{-\frac{1}{2} \left(\frac{\Delta D_i - c\Delta M_i}{\sigma_1^D} \right)^2} \quad (3.2)$$

To maximize P , we have:

$$\frac{\partial P}{\partial c} = P \times \sum_i \frac{\Delta M_i}{\sigma_1^D} \left(\frac{\Delta D_i - c\Delta M_i}{\sigma_1^D} \right) = 0 \quad (3.3)$$

Which gives c as:

$$\sum_i \Delta M_i (\Delta D_i - c\Delta M_i) = 0 \quad \Rightarrow \quad c = \frac{\sum \Delta D_i \Delta M_i}{\sum \Delta M_i^2} \quad (3.4)$$

Extend independent variable to multi-dimensional, we have:

$$\Delta D = (c_1 \ c_2 \ \cdots \ c_n) \begin{pmatrix} \Delta M^1 \\ \Delta M^2 \\ \vdots \\ \Delta M^n \end{pmatrix} + \epsilon(0, \sigma^D) \quad (3.5)$$

$$\frac{\partial P}{\partial c_\nu} \propto \sum_i \Delta M_i^\nu (\Delta D_i - \sum_\mu c_\mu M_i^\mu) = 0 \quad (3.6)$$

Arrange them in a matrix:

$$\begin{pmatrix} \sum_i \Delta D_i \Delta M_i^1 \\ \sum_i \Delta D_i \Delta M_i^2 \\ \vdots \\ \sum_i \Delta D_i \Delta M_i^n \end{pmatrix} = \begin{pmatrix} \sum_i \Delta M_i^1 \Delta M_i^1 & \sum_i \Delta M_i^2 \Delta M_i^1 & \cdots & \sum_i \Delta M_i^n \Delta M_i^1 \\ \sum_i \Delta M_i^1 \Delta M_i^2 & \sum_i \Delta M_i^2 \Delta M_i^2 & \cdots & \sum_i \Delta M_i^n \Delta M_i^2 \\ \vdots & \vdots & \ddots & \vdots \\ \sum_i \Delta M_i^1 \Delta M_i^n & \sum_i \Delta M_i^2 \Delta M_i^n & \cdots & \sum_i \Delta M_i^n \Delta M_i^n \end{pmatrix} \begin{pmatrix} c_1 \\ c_2 \\ \vdots \\ c_n \end{pmatrix} \quad (3.7)$$

Define covariance of any 2 variables as:

$$\text{cov}(x, y) = \sum_i x_i y_i \quad (3.8)$$

To get:

$$\begin{pmatrix} c_1 \\ c_2 \\ \vdots \\ c_n \end{pmatrix} = \begin{pmatrix} \text{cov}(\Delta M^1, \Delta M^1) & \text{cov}(\Delta M^2, \Delta M^1) & \cdots & \text{cov}(\Delta M^n, \Delta M^1) \\ \text{cov}(\Delta M^1, \Delta M^2) & \text{cov}(\Delta M^2, \Delta M^2) & \cdots & \text{cov}(\Delta M^n, \Delta M^2) \\ \vdots & \vdots & \ddots & \vdots \\ \text{cov}(\Delta M^1, \Delta M^n) & \text{cov}(\Delta M^2, \Delta M^n) & \cdots & \text{cov}(\Delta M^n, \Delta M^n) \end{pmatrix}^{-1} \begin{pmatrix} \text{cov}(\Delta D, \Delta M^1) \\ \text{cov}(\Delta D, \Delta M^2) \\ \vdots \\ \text{cov}(\Delta D, \Delta M^n) \end{pmatrix} \quad (3.9)$$

For multiple detectors, it is easy to get:

$$\begin{pmatrix} c_{11} & c_{21} & \cdots & c_{m1} \\ c_{12} & c_{22} & \cdots & c_{m2} \\ \vdots & \vdots & \ddots & \vdots \\ c_{1n} & c_{2n} & \cdots & c_{mn} \end{pmatrix} = \begin{pmatrix} \text{cov}(\Delta M^1, \Delta M^1) & \text{cov}(\Delta M^2, \Delta M^1) & \cdots & \text{cov}(\Delta M^n, \Delta M^1) \\ \text{cov}(\Delta M^1, \Delta M^2) & \text{cov}(\Delta M^2, \Delta M^2) & \cdots & \text{cov}(\Delta M^n, \Delta M^2) \\ \vdots & \vdots & \ddots & \vdots \\ \text{cov}(\Delta M^1, \Delta M^n) & \text{cov}(\Delta M^2, \Delta M^n) & \cdots & \text{cov}(\Delta M^n, \Delta M^n) \end{pmatrix}^{-1} \begin{pmatrix} \text{cov}(\Delta D^1, \Delta D^1) \\ \text{cov}(\Delta D^1, \Delta D^2) \\ \vdots \\ \text{cov}(\Delta D^1, \Delta D^n) \end{pmatrix} \quad (3.10)$$

Theoretically, we need only 5 BPMs to cover all the beam parameter phase space. What's the typical noise of bcm/bpm?

3.3 Beam Modulation

3.4 Lagragian

3.5 Correction

- background dilution

3.6 Result

Chapter 4

Transverse Asymmetry

The Beam Normal Single Spin Asymmetry (BNSSA, aka Transverse Single Spin Asymmetry or Transverse Asymmetry) is different from the PV asymmetry, it is purely electromagnetic and therefore parity-conserving. It arises from the interference between one-photon and two-photon exchange, which is sensitive to the imaginary part of the two-photon exchange amplitude. Transverse asymmetry is time-odd.

4.1 Motivation for Transverse Asymmetry

4.2 How to Measure the Transverse Asymmetry: the Method

4.3 The Result

Chapter 5

Systematic Uncertainties

Systematic uncertainty control is very important to and a highlight of this high-precision experiment. To achieve a smaller systematic uncertainty, a combination of fast-control and slow control was employed, which helped us to eliminate systematic uncertainties brought by the accelerator to the beam. Except the uncertainty from the machine, another important source of systematic uncertainties come from detection process, namely the acceptance function.

5.1 Q^2 and θ

Physical interpretation of \mathcal{A}_{PV} requires measurement of Q^2 better than 1%. Counting mode:

- low current
- single electron events
- tracks

5.2 Carbon Contamination in PREX-II

The Pb foil is not good thermal conductivity, which limits the highest current we can apply. To help dissipate the heat produced by electron bombardment, auxiliary materials – the Diamond foils, which are excellent thermal conductivity are used. Besides, C12 is isoscalar, and spin-0 nucleus, whose PV asymmetry is well-measured (FIXME), so the background is well-understood. Even so, the highest current is only $70 \mu A$.

The Pb208 foil is 0.5 mm thick, each diamond foil is half the thickness

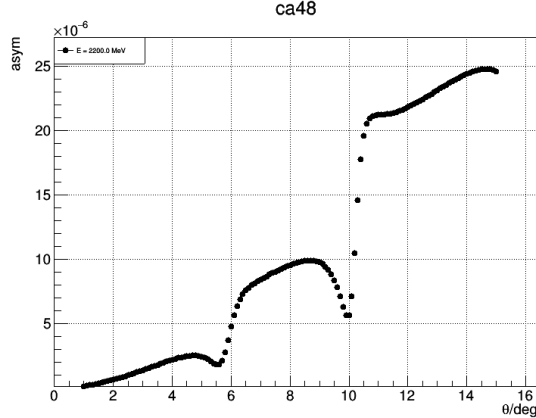
For CREX, Ca48 has good thermal conductivity, so the current can go up to $150 \mu A$ the contamination is mainly Ca40 ($\sim 4\%$ FIXME), which is also isoscalar and spin-0 nucleus, so benign background

5.3 Acceptance Function

The acceptance function is defined as the proportion of detected electrons over scattered electrons, it is a function of the scattering angle θ :

$$A(\theta) = \frac{N_{det}(\theta)}{N_{sca}}$$

The acceptance function has another importance: only with the acceptance function,



can we interpret our measurement:

$$\langle A \rangle = \frac{\int d\theta \sin \theta A(\theta) \frac{d\sigma}{d\Omega} \epsilon(\theta)}{\int d\theta \sin \theta \frac{d\sigma}{d\Omega} \epsilon(\theta)}$$

The idea is to match simulation with optics data; then we can extract the acceptance function from the simulation. For optics data, we have 2 sieves (which is just a thin steel plane with many holes on it) before the septum. Because we know each hole position on the sieve, we can therefore reconstruct the transfrom matrices between target and detector. Which can then be used in simulation to extract the acceptance function.

For the simulation, we need to identify a few things:

- Beam Position
-

We will scan through some parameters to find the best model:

- Septum current
- Collimator shift
- Pinch point shift

Chapter 6

Results

6.1 Polarization

6.1.1 Moller

6.1.2 Compton

6.2 Final Number

6.3 Physical Implication

6.3.1 Theoretical Models

Neither the nuclear interaction nor their wave functions are known to us. Unlike particle physics, there is no such a single Standard Model to describe general properties of a nuclear system, such as the ground state binding energy, nuclear size and excitation spectrum. Various models work well in their own territories. Ab-initio is mainly used to describe light nuclei while Density Functional Theory (DFT) provides very precise prediction for heavy nuclei.

ab-initio

Ab-initio is more like a theoretical approach, that needs to calculate the force between nucleons and then solve the quantum many-body equation from them. While DFT is more like an experimental approach, which uses experimental data to fit interactions in a given region of the nuclear landscape.

- Green's function Monte Carlo (GFMC)
- No-Core Shell Model (NCSM)
- Coupled-cluster

Nuclear Density Functional Theory (DFT)

The basic idea is to construct a general functional, with nucleons density distribution as input, will output the ground-state energy and other properties of the nuclear system, the difficulty lies in that no single general functional can cover all nuclei. The basic idea is simple, once we know the density distribution function, then one can calculate the total energy of the system based on this distribution function, minimization of the total energy will be the ground state, and other static properties will be inferred from the ground state. Excitation properties can also be calculated from DFT. The only problem is how to know the density distribution function.

Effective Field Theory (EFT)

Based on nucleons and pions, but still obey the symmetry of QCD. Various EFT models are based on an effective interacting Lagrangian, for example, FSUGold model has the following effective Lagrangian [21]:

$$\begin{aligned}\mathcal{L}_{\text{int}} = & \bar{\psi} \left[g_s \phi - \left(g_v V_\mu + \frac{g_\rho}{2} \boldsymbol{\tau} \cdot \mathbf{b}_\mu + \frac{e}{2} (1 + \tau_3) A_\mu \right) \gamma^\mu \right] \psi \\ & - \frac{\kappa}{3!} (g_s \phi)^3 - \frac{\lambda}{4!} (g_s \phi)^4 + \frac{\zeta}{4!} (g_v^2 V_\mu V^\mu)^2 \\ & + \Lambda_v (g_\rho^2 \mathbf{b}_\mu \mathbf{b}^\mu) (g_v^2 V_\mu V^\mu)\end{aligned}\quad (6.1)$$

This Lagrangian density describes interactions of the nucleon field ψ to various meson fields and their self-interactions. ϕ is a scalar.

The difference between different EFT models is just how many coupling they include in their effective Lagrangian density. With the Lagrangian density, one can calculate the properties of various nuclei, fitting predicted values to experimental results to get a parameter set for the coupling constant in the Lagrangian, which is called one model. Frequently used EFT models include NL3 [], FSUGold [] and

Saturation

The invariance of binding energy per nucleon (E_b/A) w.r.t. A means that the interaction between nucleons is not proportional to $A(A - 1)$, but proportional to A , which means nucleons saturate.

6.3.2 Saturation Density

Nuclear Density Function Theory the basic idea is given a Lagrangian density function:

Atomic Parity Violation Measurement

Accuracy of atomic PV measurement is about 0.3% (FIXME), which is important for the test of the SM and the search for physics beyond the SM. A higher (0.1%) precision

requires knowledge about the neutron radius better than 1%. [34]

6.4 Neutron Stars

Pb neutron radius is large \Rightarrow stiff EOS at low nuclear density (subnuclear density) combine NS radius measurement NS radius is small \Rightarrow soft EOS at high density these 2 measurements will mean softening of EOS with density \Rightarrow transition to an exotic high density phase such as quark matter, strange matter, color superconductor, kaon condensate

URCA Cooling

proton fraction for matter in beat equilibrium depends on symmetry energy $S(n)$.o The larger R_n in Pb, the lower the threshold mass for direct URCA cooling. If $R_n - R_p < 0.2 \text{ fm}$ all EOS models don't have direct URCA in $1.4 M_{\text{sun}}$ stars If $R_n - R_p > 0.25 \text{ fm}$, all models do have URCA in $1.4 M_{\text{sun}}$ stars

Bibliography

- [1] J. B. Bellicard, P. Bounin, R. F. Frosch, R. Hofstadter, J. S. McCarthy, F. J. Uhrhane, M. R. Yearian, B. C. Clark, R. Herman, and D. G. Ravenhall. Scattering of 750-mev electrons by calcium isotopes. *Phys. Rev. Lett.*, 19:527–529, Aug 1967. doi: 10.1103/PhysRevLett.19.527. URL <https://link.aps.org/doi/10.1103/PhysRevLett.19.527>.
- [2] C. J. Horowitz. Parity violating elastic electron scattering and coulomb distortions. *Phys. Rev. C*, 57:3430–3436, Jun 1998. doi: 10.1103/PhysRevC.57.3430. URL <https://link.aps.org/doi/10.1103/PhysRevC.57.3430>.
- [3] C.Y. Prescott, W.B. Atwood, R.L.A. Cottrell, H. DeStaebler, Edward L. Garwin, A. Gonidec, R.H. Miller, L.S. Rochester, T. Sato, D.J. Sherden, C.K. Sinclair, S. Stein, R.E. Taylor, J.E. Clendenin, V.W. Hughes, N. Sasao, K.P. Schüler, M.G. Borghini, K. Lübelsmeyer, and W. Jentschke. Parity non-conservation in inelastic electron scattering. *Physics Letters B*, 77(3):347–352, 1978. ISSN 0370-2693. doi: [https://doi.org/10.1016/0370-2693\(78\)90722-0](https://doi.org/10.1016/0370-2693(78)90722-0). URL <https://www.sciencedirect.com/science/article/pii/0370269378907220>.
- [4] P. A. Souder, R. Holmes, D.-H. Kim, K. S. Kumar, M. E. Schulze, K. Isakovich, G. W. Dodson, K. W. Dow, M. Farkhondeh, S. Kowalski, M. S. Lubell, J. Bellanca, M. Goodman, S. Patch, Richard Wilson, G. D. Cates, S. Dhawan, T. J. Gay, V. W. Hughes, A. Magnon, R. Michaels, and H. R. Schaefer. Measurement of parity violation in the elastic scattering of polarized electrons from ^{12}C . *Phys. Rev. Lett.*, 65:694–697, Aug 1990. doi: 10.1103/PhysRevLett.65.694. URL <https://link.aps.org/doi/10.1103/PhysRevLett.65.694>.
- [5] W. Heil, J. Ahrens, H.G. Andresen, A. Bornheimer, D. Conrath, K.-J. Dietz, W. Gasteyer, H.-J. Gessinger, W. Hartmann, J. Jethwa, H.-J. Kluge, H. Kessler, T. Kettner, L. Koch, F. Neugebauer, R. Neuhausen, E.W. Otten, E. Reichert, F.P. Schäfer, and B. Wagner. Improved limits on the weak, neutral, hadronic axial vector coupling constants from quasielastic scattering of polarized electrons. *Nuclear Physics B*, 327(1):1–31, 1989. ISSN 0550-3213. doi: [https://doi.org/10.1016/0550-3213\(89\)90284-8](https://doi.org/10.1016/0550-3213(89)90284-8). URL <https://www.sciencedirect.com/science/article/pii/0550321389902848>.
- [6] Sample at mit-bates. URL <https://bateslab.mit.edu/projects/sample>.

- [7] The g0 experiment. URL <http://research.npl.illinois.edu/exp/G0/publicWeb/>.
- [8] Happex collaboration. URL <https://hallaweb.jlab.org/experiment/HAPPEX/>.
- [9] A4 collaboration at mami. URL <https://www.blogs.uni-mainz.de/fb08-ag-maas/a4-collaboration-at-mami/>.
- [10] P. L. Anthony, R. G. Arnold, C. Arroyo, K. Bega, J. Biesiada, P. E. Bosted, G. Bower, J. Cahoon, R. Carr, G. D. Cates, J.-P. Chen, E. Chudakov, M. Cooke, P. Decowski, A. Deur, W. Emam, R. Erickson, T. Fieguth, C. Field, J. Gao, M. Gary, K. Gustafsson, R. S. Hicks, R. Holmes, E. W. Hughes, T. B. Humensky, G. M. Jones, L. J. Kaufman, L. Keller, Yu. G. Kolomensky, K. S. Kumar, P. LaViolette, D. Lhuillier, R. M. Lombard-Nelsen, Z. Marshall, P. Mastromarino, R. D. McKeown, R. Michaels, J. Niedziela, M. Olson, K. D. Paschke, G. A. Peterson, R. Pithan, D. Relyea, S. E. Rock, O. Saxton, J. Singh, P. A. Souder, Z. M. Szalata, J. Turner, B. Tweedie, A. Vacheret, D. Walz, T. Weber, J. Weisend, M. Woods, and I. Younus. Precision measurement of the weak mixing angle in möller scattering. *Phys. Rev. Lett.*, 95:081601, Aug 2005. doi: 10.1103/PhysRevLett.95.081601. URL <https://link.aps.org/doi/10.1103/PhysRevLett.95.081601>.
- [11] D. Androic, D. S. Armstrong, A. Asaturyan, T. Averett, J. Balewski, J. Beaufait, R. S. Beminiwattha, J. Benesch, F. Benmokhtar, J. Birchall, R. D. Carlini, G. D. Cates, J. C. Cornejo, S. Covrig, M. M. Dalton, C. A. Davis, W. Deconinck, J. Diefenbach, J. F. Dowd, J. A. Dunne, D. Dutta, W. S. Duvall, M. Elaasar, W. R. Falk, J. M. Finn, T. Forest, D. Gaskell, M. T. W. Gericke, J. Grames, V. M. Gray, K. Grimm, F. Guo, J. R. Hoskins, K. Johnston, D. Jones, M. Jones, R. Jones, M. Kargantoulakis, P. M. King, E. Korkmaz, S. Kowalski, J. Leacock, J. Leckey, A. R. Lee, J. H. Lee, L. Lee, S. MacEwan, D. Mack, J. A. Magee, R. Mahurin, J. Mammei, J. W. Martin, M. J. McHugh, D. Meekins, J. Mei, R. Michaels, A. Micherdzinska, A. Mkrtchyan, H. Mkrtchyan, N. Morgan, K. E. Myers, A. Narayan, L. Z. Ndukum, V. Nelyubin, Nuruzzaman, W. T. H. van Oers, A. K. Opper, S. A. Page, J. Pan, K. D. Paschke, S. K. Phillips, M. L. Pitt, M. Poelker, J. F. Rajotte, W. D. Ramsay, J. Roche, B. Sawatzky, T. Seva, M. H. Shabestari, R. Silwal, N. Simicevic, G. R. Smith, P. Solvignon, D. T. Spayde, A. Subedi, R. Subedi, R. Suleiman, V. Tadevosyan, W. A. Tobias, V. Tvaskis, B. Waidyawansa, P. Wang, S. P. Wells, S. A. Wood, S. Yang, R. D. Young, and S. Zhamkochyan. First determination of the weak charge of the proton. *Phys. Rev. Lett.*, 111:141803, Oct 2013. doi: 10.1103/PhysRevLett.111.141803. URL <https://link.aps.org/doi/10.1103/PhysRevLett.111.141803>.
- [12] D. Wang, K. Pan, R. Subedi, X. Deng, Z. Ahmed, K. Allada, K. A. Aniol, D. S. Armstrong, J. Arrington, V. Bellini, R. Beminiwattha, J. Benesch, F. Benmokhtar, A. Camsonne, M. Canan, G. D. Cates, J.-P. Chen, E. Chudakov, E. Cisbani, M. M. Dalton, C. W. de Jager, R. De Leo, W. Deconinck, A. Deur, C. Dutta, L. El Fassi, D. Flay, G. B. Franklin, M. Friend, S. Frullani, F. Garibaldi, A. Giusa,

- A. Glamazdin, S. Golge, K. Grimm, K. Hafidi, O. Hansen, D. W. Higinbotham, R. Holmes, T. Holmstrom, R. J. Holt, J. Huang, C. E. Hyde, C. M. Jen, D. Jones, H. Kang, P. King, S. Kowalski, K. S. Kumar, J. H. Lee, J. J. LeRose, N. Liyanage, E. Long, D. McNulty, D. J. Margaziotis, F. Meddi, D. G. Meekins, L. Mercado, Z.-E. Meziani, R. Michaels, M. Mihovilovic, N. Muangma, K. E. Myers, S. Nanda, A. Narayan, V. Nelyubin, Nuruzzaman, Y. Oh, D. Parno, K. D. Paschke, S. K. Phillips, X. Qian, Y. Qiang, B. Quinn, A. Rakhman, P. E. Reimer, K. Rider, S. Riordan, J. Roche, J. Rubin, G. Russo, K. Saenboonruang, A. Saha, B. Sawatzky, A. Shahinyan, R. Silwal, S. Sirca, P. A. Souder, R. Suleiman, V. Sulkosky, C. M. Sutera, W. A. Tobias, G. M. Urciuoli, B. Waidyawansa, B. Wojtsekhowski, L. Ye, B. Zhao, and X. Zheng. Measurements of parity-violating asymmetries in electron-deuteron scattering in the nucleon resonance region. *Phys. Rev. Lett.*, 111:082501, Aug 2013. doi: 10.1103/PhysRevLett.111.082501. URL <https://link.aps.org/doi/10.1103/PhysRevLett.111.082501>.
- [13] Solid. URL <https://solid.jlab.org/>.
- [14] Moller. URL https://moller.jlab.org/moller_root/.
- [15] Mesa-p2. URL <https://www.blogs.uni-mainz.de/fb08p2/>.
- [16] L.S. Cardman. Polarized electron sources for the 1990's. *Nuclear Physics A*, 546(1):317–336, 1992. ISSN 0375-9474. doi: [https://doi.org/10.1016/0375-9474\(92\)90518-O](https://doi.org/10.1016/0375-9474(92)90518-O). URL <https://www.sciencedirect.com/science/article/pii/0375947492905180>.
- [17] Philip A. Adderley, Steven Covert, Joseph Grames, John Hansknecht, Kenneth Surles-Law, Danny Machie, Bernard Poelker, Marcy L. Stutzman, Riad Suleiman, and James Clark. Photoinjector improvements at cebaf in support of parity violation experiments. *Nuovo Cimento C*, 35(4), 7 2012. ISSN 1826-9885.
- [18] H. De Vries, C.W. De Jager, and C. De Vries. Nuclear charge-density-distribution parameters from elastic electron scattering. *Atomic Data and Nuclear Data Tables*, 36(3):495–536, 1987. ISSN 0092-640X. doi: [https://doi.org/10.1016/0092-640X\(87\)90013-1](https://doi.org/10.1016/0092-640X(87)90013-1). URL <https://www.sciencedirect.com/science/article/pii/0092640X87900131>.
- [19] I. Angeli. A consistent set of nuclear rms charge radii: properties of the radius surface $r(n,z)$. *Atomic Data and Nuclear Data Tables*, 87(2):185–206, 2004. ISSN 0092-640X. doi: <https://doi.org/10.1016/j.adt.2004.04.002>. URL <https://www.sciencedirect.com/science/article/pii/S0092640X04000166>.
- [20] L. C. Maximon and R. A. Schrack. The form factor of the Fermi model spatial distribution. *J. Res. Natl. Bur. Stand. B*, 70(1), 1966. doi: 10.6028/jres.070b.007.
- [21] B. G. Todd-Rutel and J. Piekarewicz. Neutron-rich nuclei and neutron stars: A new accurately calibrated interaction for the study of neutron-rich matter. *Phys.*

- Rev. Lett.*, 95:122501, Sep 2005. doi: 10.1103/PhysRevLett.95.122501. URL <https://link.aps.org/doi/10.1103/PhysRevLett.95.122501>.
- [22] J. M. Lattimer and M. Prakash. Neutron star structure and the equation of state. *The Astrophysical Journal*, 550(1):426–442, mar 2001. doi: 10.1086/319702. URL <https://doi.org/10.1086/319702>.
- [23] B. Alex Brown. Neutron radii in nuclei and the neutron equation of state. *Phys. Rev. Lett.*, 85(0):5296–5299, Dec 2000. doi: 10.1103/PhysRevLett.85.5296. URL <https://link.aps.org/doi/10.1103/PhysRevLett.85.5296>.
- [24] M. Goldhaber, L. Grodzins, and A. W. Sunyar. Helicity of neutrinos. *Phys. Rev.*, 109:1015–1017, Feb 1958. doi: 10.1103/PhysRev.109.1015. URL <https://link.aps.org/doi/10.1103/PhysRev.109.1015>.
- [25] F.J. Hasert, S. Kabe, W. Krenz, J. Von Krogh, D. Lanske, J. Morfin, K. Schultze, H. Weerts, G. Bertrand-Coremans, J. Sacton, W. Van Doninck, P. Vilain, R. Baldi, U. Camerini, D.C. Cundy, I. Danilchenko, W.F. Fry, D. Haidt, S. Natali, P. Musset, B. Osculati, R. Palmer, J.B.M. Pattison, D.H. Perkins, A. Pullia, A. Rousset, W. Venus, H. Wachsmuth, V. Brisson, B. Degrange, M. Haguenuer, L. Kluberg, U. Nguyen-Khac, P. Petiau, E. Bellotti, S. Bonetti, D. Cavalli, C. Conta, E. Fiorini, M. Rollier, B. Aubert, D. Blum, L.M. Chouinet, P. Heusse, A. Lagarrigue, A.M. Lutz, A. Orkin-Lecourtois, J.P. Vialle, F.W. Bullock, M.J. Esten, T.W. Jones, J. McKenzie, A.G. Michette, G. Myatt, and W.G. Scott. Observation of neutrino-like interactions without muon or electron in the gargamelle neutrino experiment. *Nuclear Physics B*, 73(1):1–22, 1974. ISSN 0550-3213. doi: [https://doi.org/10.1016/0550-3213\(74\)90038-8](https://doi.org/10.1016/0550-3213(74)90038-8). URL <https://www.sciencedirect.com/science/article/pii/0550321374900388>.
- [26] C. S. Wu, E. Ambler, R. W. Hayward, D. D. Hoppes, and R. P. Hudson. Experimental test of parity conservation in beta decay. *Phys. Rev.*, 105:1413–1415, Feb 1957. doi: 10.1103/PhysRev.105.1413. URL <https://link.aps.org/doi/10.1103/PhysRev.105.1413>.
- [27] B. Zel'dovich Ya. Parity nonconservation in the first order in the weak-interaction constant in electron scattering and other effects. *Journal of Experimental and Theoretical Physics (USSR)*, 36:964–966, March 1959. URL http://jetp.ras.ru/cgi-bin/dn/e_009_03_0682.pdf.
- [28] Prex-ii proposal.
- [29] Crex proposal.
- [30] E. L. Garwin D. T. Pierce and H. C. Siegmann. *Helv. Phys. Acta*, 47:393, 1974.
- [31] G. Lampel and C. Weisbuch. Proposal for an efficient source of polarized photoelectrons from semiconductors. *Solid State Communications*, 16(7):877–880, 1975.

- ISSN 0038-1098. doi: [https://doi.org/10.1016/0038-1098\(75\)90884-4](https://doi.org/10.1016/0038-1098(75)90884-4). URL <https://www.sciencedirect.com/science/article/pii/0038109875908844>.
- [32] Noah Sherman. Coulomb scattering of relativistic electrons by point nuclei. *Phys. Rev.*, 103:1601–1607, Sep 1956. doi: 10.1103/PhysRev.103.1601. URL <https://link.aps.org/doi/10.1103/PhysRev.103.1601>.
 - [33] J. M. Grames, C. K. Sinclair, M. Poelker, X. Roca-Maza, M. L. Stutzman, R. Suleiman, Md. A. Mamun, M. McHugh, D. Moser, J. Hansknecht, B. Moffit, and T. J. Gay. High precision 5 mev mott polarimeter. *Phys. Rev. C*, 102:015501, Jul 2020. doi: 10.1103/PhysRevC.102.015501. URL <https://link.aps.org/doi/10.1103/PhysRevC.102.015501>.
 - [34] S. J. Pollock, E. N. Fortson, and L. Wilets. Atomic parity nonconservation: Electroweak parameters and nuclear structure. *Phys. Rev. C*, 46:2587–2600, Dec 1992. doi: 10.1103/PhysRevC.46.2587. URL <https://link.aps.org/doi/10.1103/PhysRevC.46.2587>.

Appendix A

Symmetry Energy

$$E_k = C(N^{5/3} + Z^{5/3})$$

Let: $A = N + Z$ and $B = N - Z$, then we have $N + \frac{A+B}{2}$, $Z = \frac{A-B}{2}$ and $B \ll A$:

$$\begin{aligned} E_k &= C \left(\left(\frac{A+B}{2} \right)^{5/3} + \left(\frac{A-B}{2} \right)^{5/3} \right) \\ &= C \left(\frac{A}{2} \right)^{5/3} \left(\left(1 + \frac{B}{A} \right)^{5/3} + \left(1 - \frac{B}{A} \right)^{5/3} \right) \\ &= C \left(\frac{A}{2} \right)^{5/3} \left(\left(1 + \frac{5B}{3A} + \frac{1}{2!} \frac{5}{3} \frac{2}{3} \left(\frac{B}{A} \right)^2 + \dots \right) + \left(1 + \frac{5}{3} \left(-\frac{B}{A} \right) + \frac{1}{2!} \frac{5}{3} \frac{2}{3} \left(-\frac{B}{A} \right)^2 + \dots \right) \right) \\ &= 2^{-2/3} C \left(A^{5/3} + \frac{5}{9} \frac{B^2}{A^{1/3}} \right) + O(\frac{B^4}{A^{7/3}}) \\ &= 2^{-2/3} C \left(A^{5/3} + \frac{5}{9} \frac{(N-Z)^2}{A^{1/3}} \right) + O((N-Z)^4) \end{aligned}$$

A.1 Resource

- hall A equipment: <https://hallaweb.jlab.org/equipment/>